

## Local versus non-local boundary conditions for the BEM in acoustics

Stefan Schneider

CNRS-LMA, 31 chemin Joseph-Aiguier 13402 Marseille cedex 20, France

e-mail: schneider@lma.cnrs-mrs.fr

**Keywords:** Absorbing materials, fast boundary element methods, non-local boundary conditions

### Abstract

To influence the acoustical characteristics of enclosures or to reduce noise pollution often walls are equipped with sound absorbing materials. To predict their effects using numerical models based on the boundary element method, these models must take into account for the treatment of the walls by the means of a boundary condition. In general this is done by using a surface impedance or admittance condition to couple sound pressure and velocity at a point on the surface. Modelling the absorbing material using the Biot-theory reveals that using a local surface impedance or admittance condition is inaccurate under certain conditions. Nevertheless, the complete model of the absorbing material is far too expensive from a numerical point of view. Therefore, in the paper we study possible extensions of the model of a local boundary condition by finding a compromise between accurate prediction given by the complete model and efficiency of the resulting numerical model. Such an extension was found to be necessary to describe correctly the acoustical behaviour of complex shaped acoustic linings in the low frequency range. The results of the study will be used to represent the acoustic lining of an anechoic chamber by a special boundary condition. This new boundary condition will then be used to simulate the acoustical behaviour of an anechoic chamber. To evaluate the quality of the developed boundary condition numerical results are compared with experimental data.

## 1 Introduction

To reduce noise pollution in urban areas or to influence the acoustical characteristics of enclosures often walls are equipped with sound absorbing materials. To predict their effects the acoustic treatment of the walls must be taken into account for in an appropriated way. In a numerical model the presents of the acoustic lining is in general represented by the means of a boundary condition at the air/lining interface  $\Gamma_Y$  without modelling the absorbing material itself. In the most general form this boundary condition can be expressed in the form

$$v_n(x) = Y(x, y)p(y) \quad \forall x, y \in \Gamma_Y. \quad (1)$$

In this form the normal fluid velocity  $v_n$ , at a single point  $x \in \Gamma_Y$  is linked to the sound pressure  $p$  at all points on the air/lining interface  $\Gamma_Y$  via the function  $Y(x, y)$  often referred to as acoustic admittance. It is pointed out that the function  $Y(x, y)$  can be complex valued and frequency dependent. Using the above relation enables to replace the unknown surface velocity  $v_n$ , appearing in the surface integrals of the weak formulation of the time harmonic Helmholtz equation. Thereafter, the sound pressure  $p$  is the only unknown for a numerical solution of the corresponding equations.

The present study compares two different numerical models to take into account for the acoustic lining of an anechoic chamber in the 20 to 200 Hz frequency range using the boundary element method. This specifically low frequency range is typical for anechoic chambers as the applied acoustic treatment is of significant thickness –.5 to 1.5 m– unusual for applications in field of reduction of noise pollution in urban areas. However, results of the present study are applicable to acoustic linings of a common thickness when considering a corresponding higher frequency range.

The original objective of the numerical analysis was the prediction of the 1.5 dB region of an anechoic chamber either based on experimental data obtained from an impedance tube experiment carried out on a sample of the lining or, even more general, based on the knowledge of the acoustical properties of the material where the lining will be made from. Hence, the prediction of the quality of a future anechoic chamber in its planning stage. Experimental data obtained from measurements carried out in the large anechoic chamber of the Laboratoire de Mécanique et d'Acoustique (LMA) serve as reference to judge the quality of the different numerical models.

The paper is organized as follows. Section two studies the performance of the often applied model of a local admittance. In section three a surface admittance obtained by the localisation of a non-local surface admittance is studied.

## 2 Model of a local admittance condition for an absorbing layer

The most common geometry model of an enclosure, used for a numerical prediction of the effect of an acoustic treatment, is the model of a more or less rectangular cavity. In such a model the real geometry of the acoustic lining is replaced by a flat surface. The latter is equipped with an appropriated surface admittance to take into account for the behavior of the applied acoustic treatment. The advantage of such a model is twofold. First, this simple geometry is easy to handle using either FEM, BEM or the image source model. Secondly, easily available results of an impedance tube experiment are

often used to derive the required surface condition. However, the fact that this measured value is valid only for normal incident of plane waves is often neglected.

The quality of such a simple model will be studied based on the experimental data obtained from measurements carried out in the large anechoic chamber of the LMA. The 1.5 dB region in the 20 to 200 Hz frequency range was obtained by measuring the sound pressure radiated by a bass-reflex box. For a detailed description of the experiment we refer to [12]. Out of the measured sound pressure  $p_{exp}$  and the sound pressure  $p_{inc}$  generated by the sound source the deviation from free-field conditions of the chamber was calculated as

$$L_p(x) = 20 \log \left( \left| \frac{p_{exp}(x)}{p_{inc}(x)} \right| \right). \quad (2)$$

The maximum allowed difference between the measured and theoretical free-field levels according to ISO 3745 and ANSI S12.35 is  $\pm 1.5$  dB at frequencies lower than 630 Hz. A region where the difference is smaller than the required  $\pm 1.5$  dB will be called the 1.5 dB region. The size of this region may depend on the frequency and the location of the acoustic source in the chamber. The upper left sub-figure of Fig. (1) and Fig. (2) show this 1.5 dB region in the large anechoic chamber at the LMA for two different positions of the sound source. Blank areas indicate regions not belonging to the 1.5 dB region.

The simple model of a rectangular cavity with the walls equipped with a local admittance condition will be used to predict the measured 1.5 dB regions of the anechoic chamber. Three different surface admittance values were used to represent

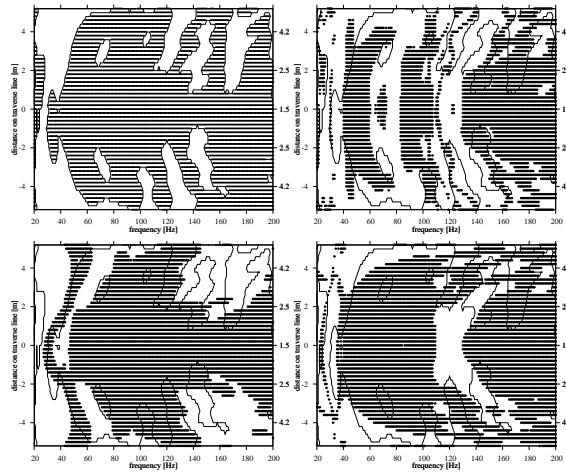


Figure 1: Measured 1.5 dB region of the large anechoic chamber of the LMA (upper left sub-figure) and 1.5 dB region obtained using numerical simulation with different local surface admittances. Upper right sub-figure, admittance obtained from numerical simulation. Lower left sub-figure, admittance obtained from results of an impedance tube experiment and lower right sub-figure, real valued admittance from numerical simulation. Sound source place in the center of the chamber.

the behavior of the acoustic lining of the large anechoic chamber of the LMA:

1. a surface admittance measured in the large impedance tube of the LMA for a  $4 \times 4$  sample of wedges of the acoustic lining. Wedges were placed in the tube without any additional fixation. In the anechoic chamber wedges are held in place by an iron wire frame.
2. Surface admittance obtained from numerical simulation of an impedance tube experiment taking into account for the mounting conditions of the wedges as present in the anechoic chamber. Numerical simulation was found to be necessary as the specific configuration, wedges held in place by an iron wire frame, could not have been analysed using the experimental facilities available at the LMA.
3. Surface admittance calculated via

$$Y = \frac{1}{\rho c} \frac{1 - \sqrt{1 - \alpha}}{1 + \sqrt{1 - \alpha}} \quad (3)$$

out of the absorption coefficient  $\alpha$  obtained from the numerical experiment. This reflects the situation that often only the absorption coefficient of a material is communicated by manufacturers.

Sound propagation in the chamber was modelled using the boundary element method. Results of the numerical simulation are compared in Fig. (1) and Fig. (2) with the experimental data obtained for two different positions of the sound source.

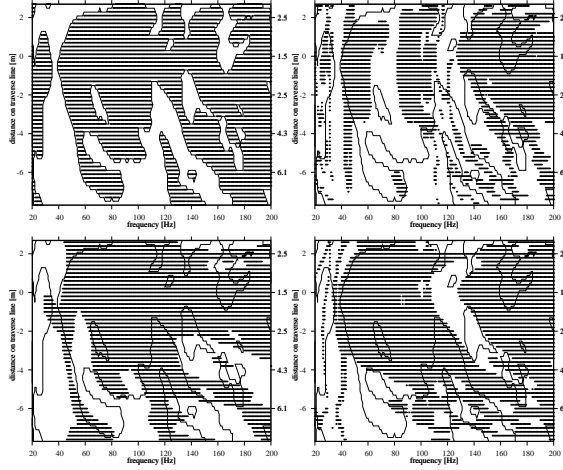


Figure 2: Measured 1.5 dB region of the large anechoic chamber of the LMA (upper left sub-figure) and 1.5 dB region obtained using numerical simulation with different local surface admittances. Upper right sub-figure, admittance obtained from numerical simulation. Lower left sub-figure, admittance obtained from results of an impedance tube experiment and lower right sub-figure, real valued admittance from numerical simulation. Sound source place at a eccentric position in the chamber.

The model of a local admittance condition fails to predict the chambers quality for frequencies lower than 150 Hz regardless the applied admittance. In this frequency range sound propagation in the absorbing material cannot be neglected as it is done when assuming a local admittance. Surface admittance 2 and 3 gave acceptable results for frequencies higher than 150 Hz. It is pointed out that the real valued admittance 3 does overestimate the absorption of the material. This is caused by the fact that eq (3) always leads to  $\rho c Y \leq 1$  what does not reflect most material's behaviour especially at low frequencies. Surface admittance 1 does not reflect the behavior of the acoustic lining in the chamber. This failure may be attributable to the fact that the mounting conditions of the lining in the anechoic chamber, did not have been taken into account for when carrying out the experiment in the impedance tube. This shows the significant influence of the mounting conditions on the performance of an acoustic treatment.

### 3 Model of a localised admittance condition for an absorbing layer

In the previous section it has been shown that the model of a local surface admittance cannot be used to predict the effect of the acoustic lining of an anechoic chamber for frequencies lower than 150 Hz. This was due to the fact that sound propagation in the absorbing material has been neglected. A numerical method is now presented that take into account for –at least partly– the effect of sound propagation in the absorbing layer. The new boundary condition enables to extent the frequency range where the effect of acoustical treatments of objects can be predicted numerically in the planing stage.

The following situation is considered. Sound propagation within the fluid domain  $\Omega_F$  is of interest. The domain  $\Omega_F$  has a common boundary  $\Gamma_Y$  with a second domain  $\Omega_B$  occupied by an absorbing material. Sound propagation in  $\Omega_B$  is modelled using the equivalent fluid or the Biot model together with a finite element method. The influence of the presents of the domain  $\Omega_B$  on sound propagation in  $\Omega_F$  is to be studied, but sound propagation in  $\Omega_B$  is of subordinate importance. Under these prevailing circumstance the following relation between the vector of the nodal sound pressures  $p^{\Gamma_Y}$  and the nodal normal surface velocities  $v_n^{\Gamma_Y}$  on the common boundary  $\Gamma_Y$

$$p^{\Gamma_Y} = Z(\omega)v_n^{\Gamma_Y} \tag{4}$$

can be established. The dense and frequency dependent matrix  $Z(\omega)$  represents a non-local impedance condition on the boundary  $\Gamma_Y$ . After a possible regularisation the matrix  $Z$  can be inverted to obtain a relation as in eq (1). Except for special cases where the discretization of  $\Omega_B$  leads only to a moderate number of unknowns, for example a small absorbing object embedded in an acoustic fluid, the numerical evaluation of  $Z(\omega)$  in eq (4) is far too expensive. Hence a suitable truncation of that matrix is to be found. Here the following strategy is suggested. Representing the sound pressure  $p^{\text{F}_Y}$  by the use of the basis functions  $\varphi_i$  used for the discretisation of the sound pressure in  $\Omega_F$  yields

$$v_{\nu}^{\text{F}_Y} = Y p^{\text{F}_Y} = Y \sum_i \beta_i \varphi_i = \sum_i \beta_i Y^i \varphi_i \quad (5)$$

where  $Y^i$  denotes the restriction of  $Y$  to the support of the basis function  $\varphi_i$ . It is pointed out that the discretisation of  $\Omega_B$  and  $\Omega_F$  may be different. If the domain  $\Omega_B$  possesses a periodic geometry then with a proper choice of the basis functions all matrices  $Y^i$  are identical. However, the matrix  $Y^i$  still couples the basis function  $\varphi_i$  to all points on  $\Gamma_Y$  and is thus still a non-local coupling condition. A localisation of this non-local behavior can be achieved by neglecting entries of the vector  $v_{\nu}^{\text{F}_Y}$  that correspond to points that are far away from the support of  $\varphi_i$ . That is keeping only the first  $n_T$  rows of  $Y^i$

$$v_{\nu}^{\text{F}_Y}(\varphi_i) \approx \begin{bmatrix} v_{\nu}^{\text{F}_Y} \\ 0 \end{bmatrix} = \begin{bmatrix} Y_{<1:n_T, :>}^i \\ 0 \end{bmatrix} \beta_i \varphi_i = Y_{n_T}^i \beta_i \varphi_i \quad (6)$$

and assuming that the discarded velocity components are of minor importance. The rows of  $Y^i$  are supposed to be ordered such that the first  $n_T$  rows correspond to the points the closest to the support of  $\varphi_i$ . The quality of the proposed localization highly depends on the behavior of the absorbing material in the frequency range of interest. The more the material is absorbing the smaller  $n_T$  can be chosen as sound propagation in the material is less relevant. Thus the value of  $n_T$  where the matrix is truncated determines the accuracy of the approximation but also the numerical costs. A measure for the truncation error depending on a specific incident sound field can be defined as follows

$$\varepsilon^{n_T}(p_{\text{inc}}) = \frac{\|(Y^i - Y_{n_T}^i)p_{\text{inc}}\|}{\|Y^i p_{\text{inc}}\|} \quad (7)$$

The dependency of the error measure on a certain sound field has been introduced to account for the type of application we have in mind. At low frequencies the sound field in an enclosure is not arbitrary. In general it can be represented –or at least approximated with a sufficient accuracy– using a set of monopole sound sources. Therefore, a set of monopole sources placed at a certain distance from the support of the basis functions  $\varphi_i$  can be used to generate a sound field that is fairly similar to that of the real application.

The quality of the presented localisation of the non-local admittance condition has been tested using two different materials. Material A is a polyester fibrous material used to manufacture acoustic linings of anechoic chambers. The acoustic parameters as given in [8] have been used. The second material is the melamine foam used as acoustic lining in the anechoic chamber of the LMA. Both sets of parameters are given in Table (1). To model the melamine foam the Biot model [2, 3, 6, 4, 1] has been used, whereas material A was modelled using the equivalent fluid model as proposed in [8]. Each

material	Young's module	Poisson ratio	density	flow resistivity	porosity	tortuosity	characteristic dimensions	
	E [N/m <sup>2</sup> ]	$\nu$	$\rho$ [kg/m <sup>3</sup> ]	$\sigma$ [Ns/m <sup>4</sup> ]	$\Phi$	$\alpha_{\infty}$	$\Lambda$ [m]	$\Lambda'$ [m]
melamine	.16e+6	.44	8.35	1.2e4	.99	1.0	.8e-4	.28e-3
Material A	-	-	-	3.0e3	.98	1.0	.2e-3	.3e-3

Table 1: Material parameters of the melamine foam and material A.

of the individual elements of the acoustic lining consists of a base of .3×.3 m<sup>2</sup> and .4 m in length and a tapering section of .7 m in length. An array of 7×7 and 9×9 wedges for material A and an array 5×5 and 7×7 wedges for the melamine foam were used for numerical simulations. The incident sound pressure was applied to the central wedge of the arrays. The error as defined in eq (7) is shown in Fig. (3) for the two materials. For material A, even when truncating the vector  $v_{\nu}^{\text{F}_Y}$  after the central wedge ( $n_T=1$ ), the error according to eq (7) is less than 50%. Taking into account also for the adjacent wedges the error drops down to less than 10%. In addition the error is almost independent on the total size of the array as results for the array of 7×7 and 9×9 wedges are almost undistinguishable. The situation is less favorable for the melamine foam. To have the truncation error smaller than 50% over the entire frequency range at least the two adjacent layers of wedges must be used. However, for frequencies higher than ≈100 Hz using only the adjacent layer of wedges results in a truncation error less than 50%. The domain  $\Omega_B$  which is used to evaluate  $Z$  in eq (4) has been truncated according to  $n_T$ . This must be seen as compromise between numerical efficiency and accuracy. For frequencies lower than 100 Hz the non-local

behavior of the material cannot be neglected and the fully coupled fluid/structure–interaction problem must be considered.

The proposed localized admittance condition was used to predict the 1.5 dB region of the large anechoic chamber of the LMA. In contrast to Sec. (2) now the real geometry of the lining will be taken into account. The lining consists of 3720 melamine wedges as described above. As all of the wedges are identical only a single matrix  $Y_{n_T}^i$  is needed. However, to take into account for the anisotropy of the melamine foam three different matrices  $Y_{n_T}^j$ , representing the three different material orientations, have actually been used. They were precalculated in the frequency range of 20 to 200 Hz with a frequency resolution of 1 Hz using a finite element method. To avoid meshing the domain  $\Omega_F$ , with its complex shape caused by the geometry of the acoustic lining, the boundary element method has been used for the numerical simulation. Hence the total sound pressure  $p = p_{inc} + p_{scat}$  within the chamber was obtained solving

$$p(y) + \int_{\Gamma_F} \frac{\partial \phi(x, y)}{\partial \nu} p(x) d\Gamma_F - a \int_{\Gamma_F} \phi(x, y) Y p(x) d\Gamma_F = p_{inc}(y) + \int_{\Gamma_F} \frac{\partial \phi(x, y)}{\partial \nu} p_{inc}(x) d\Gamma_F - a \int_{\Gamma_F} \phi(x, y) \frac{\partial p_{inc}}{\partial \nu} d\Gamma_F \quad (8)$$

with  $p_{inc}$  the incident and  $p_{scat}$  the scattered sound field and the matrix  $Y(\omega) \in \mathbb{C}^{324 \times 36}$ . Each of the wedges has been modelled using 9 elements resulting in a mesh size of .3 m. Linear discontinuous basis functions [7] together with a multilevel fast multipole [10, 9, 5] accelerated collocation method have been used. The linear system with  $N=138280$  unknowns was solved using the GMRes [11] solver. Depending on frequency 80...120 iterations were necessary to obtain a residual of  $\epsilon = 1.e - 6$ . The total solution time was 2.5...4 hours per frequency on a SGI Origin3800 of the Center for Information Services and High Performance Computing of the Technische Universität Dresden, Germany. Numerical results are compared with experimental data in Fig. (4) for two different source positions. A solid dot represents the numerical result. The bounds of the 1.5 dB region obtained from experimental data are represented by a solid line. For both source positions numerical and experimental results agree well for frequencies higher than 100 Hz. But even below that frequency accuracy is better than indicated by the error measure eq (7).

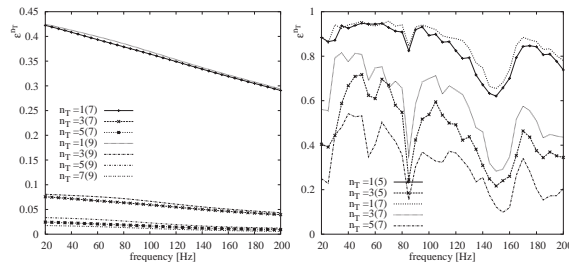


Figure 3: Truncation error eq (7) for different values of  $n_T$ . The given values for  $n_T$  represent the size of the truncated array and the numbers in brackets give the total size of the array. Left sub-figure material A and right sub-figure melamine.

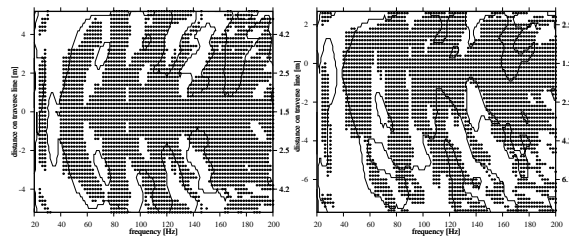


Figure 4: 1.5 dB regions for two source positions in the chamber obtained using numerical simulations with the localized surface admittance.

## Conclusion

It has been shown that at low frequencies the presents of sound absorbing materials cannot be modelled using a local surface admittance. This is due to the fact that at low frequencies the material is not sufficiently absorbing such that sound propagation within the absorbing material can not be neglected. Taking into account for these propagation effects in the vicinity of an observation point leads to an admittance matrix instead of a scalar admittance. This localised boundary condition can be used in a boundary element context with nearly no extra numerical costs. But this new type of boundary condition enables a reliable numerical prediction of the effect of the acoustical treatment in the low frequency range. Furthermore, a measure has been proposed that can be used to determine what kind of boundary condition must be applied depending on the frequency range and the acoustical and geometrical properties of the acoustic treatment.

## Acknowledgments

The author was financed by a grant from the "Deutsche Forschungsgemeinschaft". Numerical simulations were run on a SGI Origin3800 at the Center for Information Services and High Performance Computing at the Technische Universität Dresden, Germany. The author likes to thank C. Kern who made available the experimental data of the anechoic chamber.

## References

- [1] N. Atalla, R. Panneton, and P. Deberge. A mixed pressure-displacement formulation for poroelastic materials. *Journal of the Acoustical Society of America*, 104(3):1444–1542, 1998.
- [2] M. A. Biot. Theory of propagation of elastic waves in a fluid-saturated porous solid. I. low-frequency range. *Journal of the Acoustical Society of America*, 28(2):168–178, 1956.
- [3] M. A. Biot. Theory of propagation of elastic waves in a fluid-saturated porous solid. II. higher frequency range. *Journal of the Acoustical Society of America*, 28(2):179–191, 1956.
- [4] J.-F. Champoux, Y. Allard. Dynamic tortuosity and bulk modulus in air-saturated porous media. *Journal of Applied Physics*, 70(4):1975–1979, 1991.
- [5] E. Darve. The fast multipole method I: Error analysis and asymptotic complexity. *SIAM Journal on Numerical Analysis*, 38(1):98–128, Feb. 2001.
- [6] D. Johnson, J. Koplik, and R. Dashen. Theory of dynamic permeability and tortuosity in fluid-saturated porous media. *Journal of Fluid Mechanics*, 176:379–401, 1987.
- [7] S. Marburg and S. Schneider. Influence of element types on numeric error for acoustic boundary elements. *Journal of Computational Acoustics*, 11(3):363–386, 2003.
- [8] X. Olny. Acoustical properties of multiscales absorbing porous materials. In *Proceedings of Sapem 2005*, pages 273–286, ENTPE Lyon, 2005. CD.
- [9] J. Rahola. Diagonal Forms of the Translation Operators in the Fast Multipole Algorithm for Scattering Problems. *BIT*, 60(2):333–358, 1996.
- [10] V. Rokhlin. Diagonal Forms of the Translation Operators for the Helmholtz Equation in Three Dimensions. *Applied and Computational Harmonic Analysis*, 1:82–93, 1993.
- [11] Y. Saad and M. H. Schultz. GMRES: a generalized minimal residual algorithm for solving nonsymmetric linear systems. *SIAM Journal on Scientific and Statistical Computing*, 7(3):856–869, 1986.
- [12] S. Schneider, C. Kern, and H.-J. Hardtke. Characterization of the large anechoic chamber of the Laboratoire de Mécanique et d'Acoustique. *Journal of the Acoustical Society of America*, 2006. submitted for publication.

## A two-parameter model for crack growth simulation under variable load spectrum by combined FEM-DBEM approach

R. Citarella, G. Cricri

University of Salerno, dept. of Mechanical Engineering, Fisciano (SA), Italy

**Keywords:** FEM-DBEM APPROACH, TWO-PARAMETER MODEL, RESIDUAL STRESSES

**Abstract.** This paper describes the application of a two-parameters crack growth model, based on the usage of two threshold material parameters ( $\Delta K_{th}$  and  $K_{max,th}$ ) and on the allowance for residual stresses, introduced at the crack tip by a fatigue load spectrum. The coupled usage of Finite Element Method (FEM) and Dual Boundary Element Method (DBEM) is proposed in order to take advantage of the main capabilities of the two methods. The procedure is validated by comparison with available experimental results, in order to assess its capability to predict the retardation phenomena following an overload, applied during a fatigue test on a standard CT specimen. The numerical results are consistent with the experimental outcomes.

### Introduction

This paper focuses on crack retardation phenomena under spike load spectrum [1]. An original implementation of the two-parameters crack growth model described in [2-7] is presented, together with a validation procedure. In particular the coupled usage of Finite Element Method (FEM) and Dual Boundary Element method (DBEM) is proposed: FEM is more efficient for elastic-plastic analysis (needed to assess the residual stress profile) whilst DBEM allows an efficient automatic crack propagation, especially for complex geometry or for mixed mode conditions. The Dual Boundary Element Method [8] (DBEM), as implemented in the commercial code BEASY [9], is adopted for the crack propagation simulation whereas the FEM code ANSYS is used to calculate the residual stresses by elastic-plastic analysis. The procedure validation comes from a series of laboratory tests, realised in order to evaluate the capabilities of the procedure in predicting the crack retardation phenomena induced by an overload.

### Problem description and theoretical model

The load spectrum effects, as well as other transient effects, arise due to perturbation of the stress distribution ahead of the crack tip with respect to the steady-state stress field: for example, in presence of an overload, the stress field at crack tip is altered by residual stresses generated by the enhanced plastic deformations. The basic effect of these residual stresses is to change the effective values of the total Stress Intensity Factor (SIF) at the crack tip, with both  $K_{min}$  and  $K_{max}$  generally affected in the same way, so as to leave unchanged the parameter  $\Delta K$ . Consequently, the primary effects of residual stresses on crack growth rates are related to the  $K_{max}$  variations and not to the  $\Delta K$  variations. This is accounted for by the aforementioned two parameters approach. According to this theory, fatigue crack growth can be viewed, fundamentally, as a two-parametric problem, where two driving forces,  $K_{max}$  and  $\Delta K$ , drive the growth of a fatigue crack. Since it is assumed that, in presence of an overload,  $K_{max}$  also enters as the major driving force for fatigue crack growth (in addition to the classical parameter  $\Delta K$ ), the corresponding residual stresses can affect crack growth rates even if they do not affect the parameter  $\Delta K$ . In addition, the theory assumes that there are two fatigue thresholds,  $K_{max,th}^*$  and  $\Delta K_{th}^*$  corresponding to the two driving forces. These are asymptotic values in the  $\Delta K$ - $K_{max}$  graphs of the fatigue curves: both the driving forces must be simultaneously larger than the relative thresholds for fatigue crack growth to occur. Since overload residual stress effects manifest primarily through a reduction in  $K_{max}$  levels, a crack growth rate retardation generally follows the overload and an arrest in crack growth can occur if these stresses are sufficiently high (i.e.  $K_{max}$  falls below  $K_{max,th}$ ). The crack growth law adopted is [4]:

$$\frac{da}{dN} = A (\Delta K - \Delta K_{th}^*)^n (K_{max} - K_{max,th}^*)^m \quad (1)$$

and is calibrated by best fitting the material parameters  $A$ ,  $n$ ,  $m$ , based on constant amplitude preliminary tests. The threshold parameters  $K_{max,th}^*$ ,  $\Delta K_{th}^*$  are also evaluated by experimental tests. The overload effect is reproduced by taking into account the residual stress influence on the driving parameters  $\Delta K$ ,  $K_{max}$ .

### Crack growth law fatigue parameters

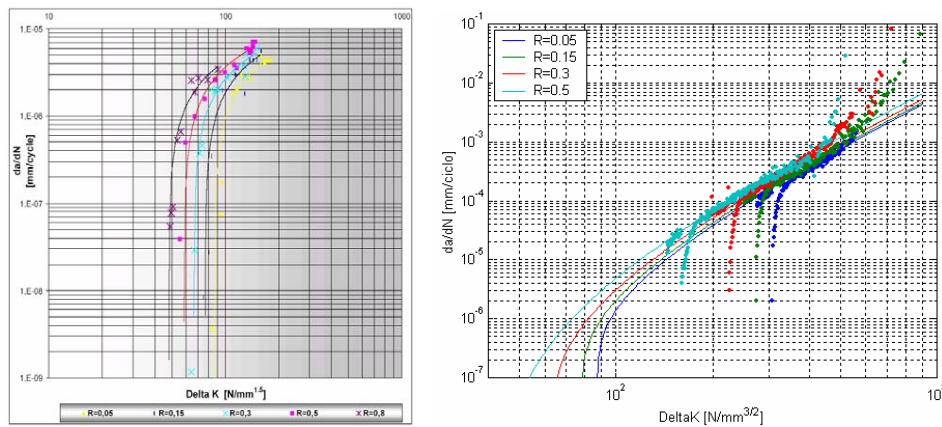
**Introduction.** The two parameter model is tested using crack growth experimental data from aluminium (2024 T351 clad sheet, 3.2 mm thick) CT specimens, undergoing a load spectrum made of a baseline cycle, ranging from  $P_{\min} = R \cdot 800$  N and  $P_{\max} = 800$  N, and a spike load intermingled to the baseline sequence, with overload ratio  $R_{ol} = P_{\max OL} / P_{\max} = 2$ . The residual stress field due to the spike load is calculated by comparing two FEM elastic-plastic simulations, respectively realised under constant and variable amplitude load conditions. The impact of such residual stresses on the driving forces is calculated, then the crack growth model is applied and its results compared with experimental crack growth rates after the spike load application. It is remarkable that the crack growth law, whose validity is expected to be extended to any overload ratio, is calibrated using only experimental data from constant amplitude test.

**Determination of the threshold parameters ( $\Delta K_{th}^*$ ,  $K_{max,th}^*$ ).** The experimental threshold data (Table 1) are provided by a sufficient number of tests on CT specimens (whose width is  $w=25.4$  mm). The experimental near threshold crack growth rates are determined and their interpolation, for each stress ratio  $R$ , reported in Fig. 1a. Eq. 2 is used in order to fit all the threshold data obtained for different  $R$ -ratios [4]:

$$\Delta K_{th} = \Delta K_{th}^* + \frac{B}{(K_{max} - K_{max,th}^*)^m} \quad \text{with} \quad K_{max} = \Delta K_{th} / (1-R) \quad (2)$$

and calculate, by minimization of the fitting error, the threshold values  $\Delta K_{th}^*$  and  $K_{max,th}^*$  (Table 2).

**Determination of the material parameters ( $A$ ,  $n$ ,  $m$ ).** In order to obtain the material parameters ( $A$ ,  $n$ ,  $m$ ), Eq. 1 is fitted to data taken from constant amplitude experimental tests on CT specimens, at different  $R$ -ratios. The resulting values for  $A$ ,  $n$ ,  $m$ , valid for every  $R$ -ratio in the considered range, are reported in Table 2. In Fig. 1b, plots of Eq. 1, with the above values of the material parameters and no allowance yet of residual stresses, are superimposed to the experimental results obtained from the addition of a spike load in the baseline sequence: the correlation is accurate but in the transient part following the overload application. It will be shown in the following that this transient part is correctly simulated by Eq. 1 when allowance for residual stresses is introduced in the SIF calculation.



Figs. 1a-b. Experimental threshold data with numerical interpolation (left), and model calibration ( $A$ ,  $n$ ,  $m$  assessment) under constant amplitude load conditions (right), for 2024 T351 aluminum alloy.

### Residual stresses assessment

**Introduction.** The overload retardation effect is evaluated by considering the crack growth law (Eq. 1), in which the SIF is equal to the sum of the nominal SIF, corresponding to the remote load, plus the SIF corresponding to the contribution of the residual stresses, induced by the plastic flow at the crack tip.

Since the residual stress contribution for the constant amplitude load is implicitly taken into account in the calibration of Eq. 1, only the residual stresses generated by the overload effect need to be considered. Such stresses are calculated, for a given crack length, as a difference between the residual stresses arising from the load sequence that includes an overload, and from the baseline load sequence, as in the following steps:

1. Elastic-Plastic FEM analysis of the specimen undergoing a constant amplitude load cycle.
2. Elastic-Plastic FEM analysis of the specimen undergoing a load cycle with a single spike load.
3. Calculation of the residual stress profile generated by the overload.

R	0.05	0.15	0.3	0.5	0.8
$\Delta K_{th}$ (N/mm <sup>3/2</sup> )	94.9	82.2	69.3	56.7	50.6
$K_{max}$ (N/mm <sup>3/2</sup> )	99.9	96.7	98.9	113	253

Table 1.  $\Delta K$  and  $K_{max}$  under threshold conditions ( $da/dN=1e-7$  mm/cycle) for different R values.

$\Delta K_{th}^*$	$K_{max,th}^*$	A	n	m
50	96	1.007e-10	1.99	0.600

Table 2. Fitting values for the calibration factors (with  $da/dN$  in mm/cycle and  $\Delta K$  in N/mm<sup>3/2</sup>).

**Materials constitutive law.** Averaging the static tension tests data for the 2024HP-T351, a relationship has been established between true stress and logarithmic strain, and the related diagram is plotted in Fig. 2. The constitutive law in plastic flow conditions is assumed to be a power law (Ramberg-Osgood model):

$$\frac{\varepsilon}{\varepsilon_0} = \left( \frac{\sigma}{\sigma_0} \right)^N \tag{3}$$

and the following parameters can be calculated by fitting of experimental data:

$$\begin{aligned} \sigma_0 &= \sigma_y = 320 \text{ MPa}; & \varepsilon_0 &= \sigma_y / E = 0.00457; & \varepsilon_{f,log} &= \log(1 + \varepsilon_f) = 0.191; \\ \sigma_{u,true} &= \sigma_u(1 + \varepsilon_f) = 537 \text{ MPa}; & N &= \log(\varepsilon_{f,log} / \varepsilon_0) / \log(\sigma_{u,true} / \sigma_0) = 7.2; \end{aligned}$$

**Elastic-plastic FEM procedure.** The overload residual stress calculation requires two elastic-plastic FEM simulations (Fig. 3): first, the baseline constant amplitude cycle is imposed on the specimen model (point 1') so that, after load removal (point 2'), the material surrounding the crack tip is affected by a residual stress field as a consequence of the constant amplitude load plastic zone; then, the spike load (overload ratio  $R_{ol} = 2$ ) is applied and, after load removal (point 2''), the corresponding residual stress field, enhanced by the overload effect, is recorded.

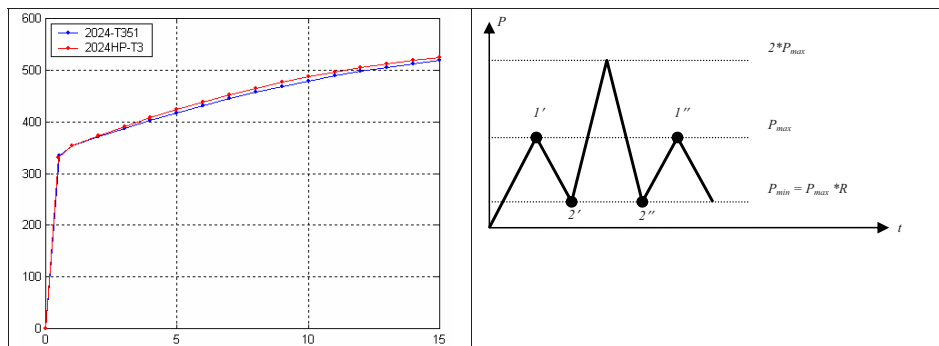


Fig. 2. Averaged true stress (MPa) vs. % logarithmic strain. Fig. 3. Load cycles for residual stress calculations.

Assuming that the principle of superposition still holds true (such approximation is acceptable if the plastic zone dimension is sufficiently small), it is possible to assume that the stress field after the spike load removal

(point 2'' and 1''), is equal to the sum of the stress field produced by the current baseline remote load plus the residual stress field inherited by the application of the previous spike load:

$$\begin{aligned} \sigma_{y,\text{tot}} &= \sigma_{y,\text{appl}} + \sigma_{y,\text{res}} \\ \sigma_y^{(1'')} &= \sigma_y^{(1')} + \sigma_{y,\text{res}}^{(1)} \quad \text{and consequently} \quad \sigma_{y,\text{res}}^{(1)} = \sigma_y^{(1'')} - \sigma_y^{(1')} \end{aligned} \quad (4_1)$$

$$\sigma_y^{(2'')} = \sigma_y^{(2')} + \sigma_{y,\text{res}}^{(2)} \quad \text{and consequently} \quad \sigma_{y,\text{res}}^{(2)} = \sigma_y^{(2'')} - \sigma_y^{(2')} \quad (4_2)$$

Fig. 4 shows the finite element mesh adopted for the 3D analyses (22000 8-node linear elements): only a quarter of the CT specimen is modelled because of the presence of two symmetry planes.

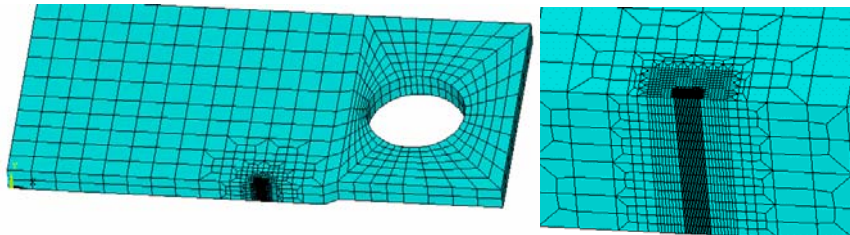


Fig. 4. Mesh used for the 3D FEM analyses with close up of the area surrounding the crack tip.

The elastic-plastic analyses are performed assuming an isotropic-hardening behaviour for the material, with Von-Mises yield criterion. In order to use the 3D FEM results for a 2D crack growth simulation, the residual stress profile is averaged along the thickness: after evaluating the residual stress profiles on different planes equally spaced along the thickness ( $z$  direction), average values are provided by an equilibrium condition:

$$\bar{\sigma}_{\text{res}}(x) = \frac{1}{B} \int_0^B \sigma_{\text{res}}(x, z) dz \quad (5)$$

#### Approach based on Dual Boundary Element method (DBEM)

**Introduction.** The DBEM incorporates two independent boundary integral equations, the displacement equation applied at the collocation point on one of the crack surfaces and the traction equation on the other crack surface, so that the crack problem can be solved in a single region formulation.

The residual stresses, available along the predefined crack propagation path by the previously mentioned elastic-plastic FEM analysis, are then introduced in the DBEM model, on the propagating crack edges.

Even in case the crack path is not known a priori, it would be possible to determine the crack propagation path by a purely elastic DBEM analysis, where only the remote load is applied (without residual stresses), then calculate by FEM the residual stresses along such virtual line and import them in the DBEM model. The underlying hypothesis is that the crack path is not appreciably affected by few cycles with an increased maximum load, intermingled in a constant amplitude fatigue traction load sequence.

**Procedure description.** If the superposition principle holds true, the residual stress effect on SIFs can be modelled by a distribution of tractions on the advancing crack edges (Figs. 5-6): such tractions are corresponding to the residual stresses existing on a virtual line traced by the advancing crack (the material at this stage is not cracked yet). The following step is to realise a DBEM crack propagation analysis, with SIFs and crack growth rates automatically calculated by the DBEM code, where the chosen crack propagation law (Eq. 1) is implemented, and the CT specimen is modelled with the crack configuration at the moment in which the overload is applied (Fig. 5). Such specimen undergoes a remote traction load equal to 800 N, applied by means of two pins and acting in combination with the residual stresses previously calculated by an FEM elastic-plastic analysis. Such residual stresses are initially applied directly on the crack edges and a crack analysis is performed. In Fig. 6 it is possible to see the deformed plot of the crack tip, comparing the case with and without residual stresses superimposed to the remote load: it is clear the beneficial closure effect of the compressive residual stresses generated at the crack tip by the overload.

Applying the residual stresses directly on the crack edges, even if more precise than using the body loads, has some drawbacks with the DBEM code adopted: the automatic crack propagation is prevented and manual intervention is needed to change the applied load on crack edges after each crack propagation step. Consequently, the simulation of the aforementioned crack edge tractions is made by parallel load lines, with

a small offset (Fig. 7). A convergence analysis is made for this specific example with  $R=0.15$ , in order to compare the differences in the calculated SIFs, provided by the application of the tractions directly on crack edges or, alternatively, on the aforementioned load lines with a variable distance from the crack axis (Table 3). This is aimed at understanding how much the load lines must be close to the crack axis in order to simulate a load on the crack edges with a sufficient accuracy. On the other hand, in order to avoid numerical round off errors, it is necessary to keep the ratio between the load line distance and the crack tip element length above a given threshold. The use of double precision for the numerical resolution becomes mandatory. In Fig. 8 a deformed contour plot of Von Mises stresses in the final cracked configuration is shown, and in Fig. 9 the SIF results are plotted as varying during the crack propagation.

Again a convergence study is performed based on a variable distance of the body lines from the crack axis and on a variable growth increment: the convergence is judged satisfactory (SIFs difference error below 2%) with a growth increment  $\Delta a=0.014$  mm and a load line distance from the crack axis  $d=0.005$  mm.

In Fig. 10 the crack model with highlight of applied body loads is shown: it is evident the beneficial effect of the superimposed residual stresses, that reduce the crack opening in that part of the crack that, during the propagation, is crossing the residual stress field.

**Crack growth rates prediction.** Crack growth rates can be predicted using Eq. 1, where  $\Delta K_{tot}$  and  $K_{max,tot}$  include the contributions from both applied and residual stresses. Results are shown in Figs. 11a-b for the different  $R$  ratios. In Fig. 11a, the crack growth rate for 2024-T351 is plotted for comparison between experimental and simulation results, whereas, in Fig. 11b the total crack length vs. number of cycles is plotted.

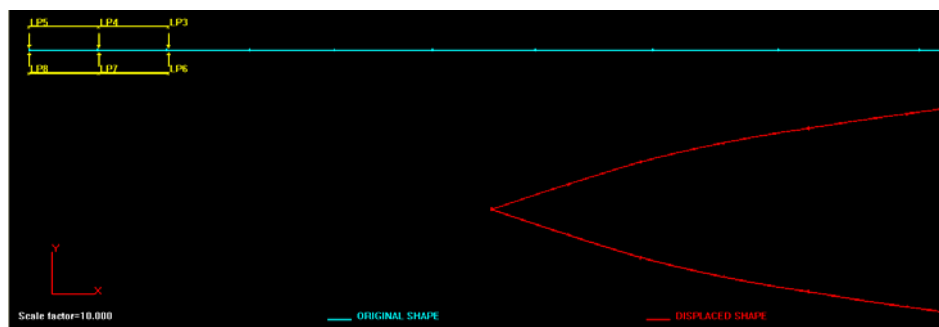
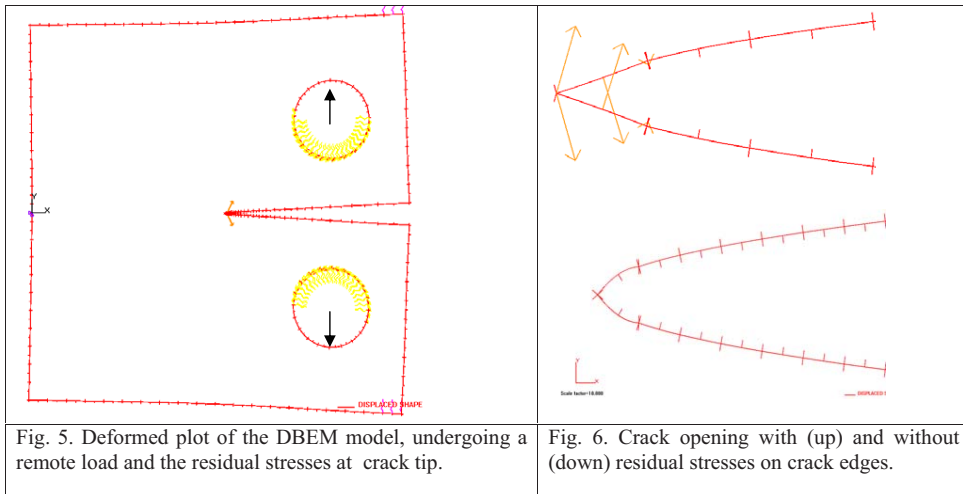


Fig. 7. Crack opening due to remote load with superimposed residual stresses (acting as two load lines).

Load line distance from crack axis (mm)	KI (MPa*mm <sup>1/2</sup> )	% error
0 (load directly applied on crack edge)	186	0
0.01	203	9.1
0.005	196	5
0.0025	182	-2.1

Table 3. Convergence study and comparison between the two load cases: with traction directly applied on the crack edges or alternatively by body load lines parallel to the crack axis.

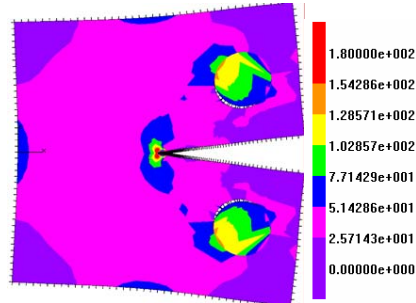


Fig. 8. Von Mises stresses (deformed scale=15).

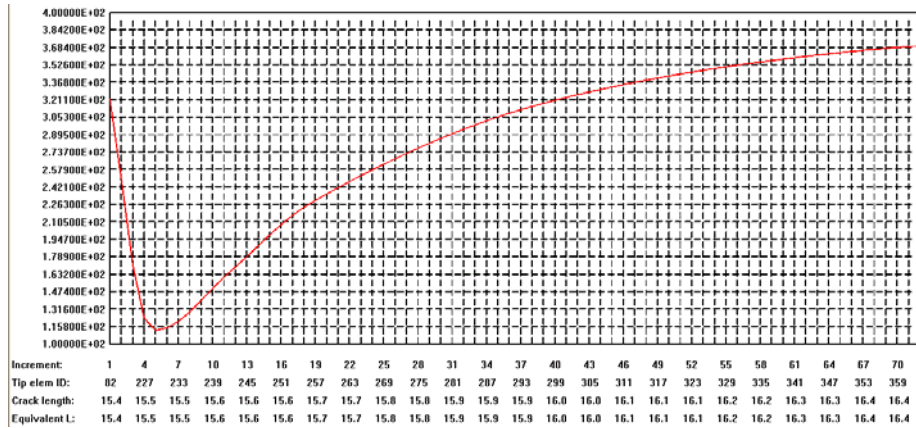


Fig. 9. K<sub>I</sub> (MPa\*mm<sup>1/2</sup>) with superimposed residual stresses by FEM-DBEM procedure with load line distance from crack axis d=0.005 mm and growth increment equal to the tip element length.

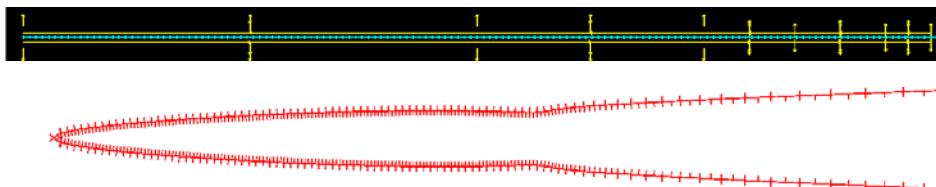


Fig. 10: Crack displaced shape (scale factor = 100) and highlight of residual stress applied by two load lines distant 0.005 mm from the crack axis.

**Conclusions**

The overload effect depends on the following material parameters:

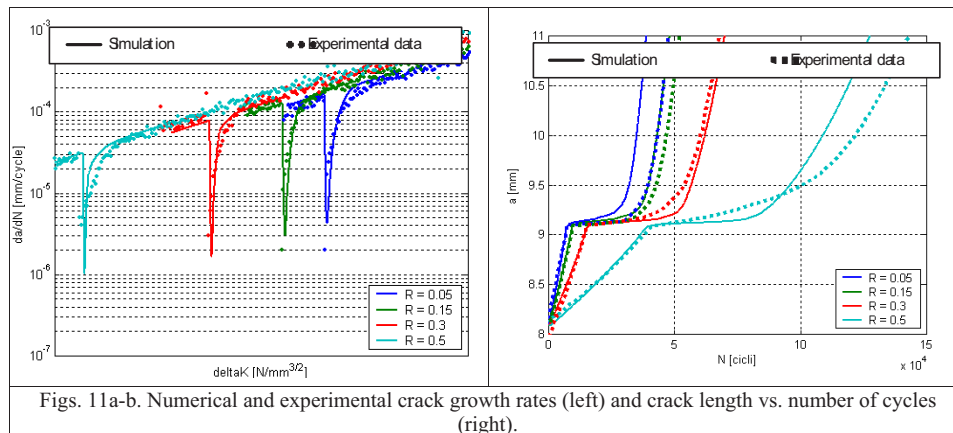
1. The stress-strain curve (that affects the FEM calculations of the residual stress).
2. The thresholds  $\Delta K_{th}^*$  and  $K_{max,th}^*$  of the driving forces.
3. The constant amplitude crack growth curves.

For the two considered alloys, only the thresholds have a non-negligible effect on the model response differences, being the other parameters very close each other.

The errors displayed can be considered acceptable at this stage, considering that: the results for the single material are very good, and they have been obtained without any calibration on the overload experimental

data; the experimental data derives from very few specimen (the allowance for the experimental data scattering would request a higher number of specimens [10]).

Another results of the overall activity is to be related to the enabling of short crack growth propagation under linear elastic fracture mechanics, being the plastic effects simulated by ad hoc generated and imposed body load in the DBEM analysis, without the need for any non physical calibration parameter as in many phenomenological model aimed at load spectra allowance (Generalised Willenborg model, Wheeler model).



Figs. 11a-b. Numerical and experimental crack growth rates (left) and crack length vs. number of cycles (right).

#### References

1. Cali, C., Citarella, R., Perrella, M., Crack growth under general load spectrum: numerical simulation and experimental tests, XI International Conference CEMEM 2003, 12-14 May, Halkidiki, Greece.
2. K. Sadananda, A.K. Vasudevan, R.L. Holtz, E.U. Lee, Analysis of overload effects and related phenomena, *International Journal of Fatigue* 21 (1999), pp. S233–S246.
3. A.K. Vasudevan, K. Sadananda, G. Glinka, Critical parameters for fatigue damage, *International Journal of Fatigue* 23 (2001), pp. S39–S53.
4. K. Sadananda, A.K. Vasudevan, Short crack growth and internal stresses, *Int. J. Fatigue* Vol. 19, Supp. No. 1, pp. S99–S108, 1997.
5. A.K. Vasudevan, K. Sadananda and K. Rajan, Role of microstructures on the growth of long fatigue cracks, *Int. J. Fatigue* Vol. 19, Supp. No. 1, pp. S151–S159, 1997.
6. C. Cali, R. Citarella, G. Cricri, Assessment of allowable dents on aeronautic panels based on the coupled usage of FEM-DBEM methodology, International Conference on Boundary Element Techniques, 24-26th July 2007, Naples, Italy.
7. C. Cali, R. Citarella, G. Cricri, A two-parameter model for crack growth simulation under variable spectrum load by combined fem/analytical approach, The 6th International Conference on Intelligent Processing and Manufacturing of Materials, June, 25-29 2007.
8. Portela A., Aliabadi M.H. & Rooke D.P. Dual Boundary Incremental Analysis of Crack Propagation, *Int. Journal Computers and Structures* 46 (1993), pp 237-247.
9. BEASY, BEASY V10r7 Documentation, C.M BEASY Ltd, 2007.
10. J. K. Kim, D.-D. Shim, A statistical approach for predicting the crack retardation due to a single tensile overload, *International Journal of Fatigue* 25, (2003), pp. 335-342.



## An algorithm for nonlinear BEM with adaptive refinement of the domain mesh

Daniele Gaspari<sup>1</sup>, Maurizio Aristodemo<sup>2</sup>

<sup>1</sup> Dip. di Strutture, Univ. della Calabria, Rende(CS) – Italy, [daniele.gaspari@labmec.unical.it](mailto:daniele.gaspari@labmec.unical.it)

<sup>2</sup> Dip. di Strutture, Univ. della Calabria, Rende(CS) – Italy, [aristodemo@labmec.unical.it](mailto:aristodemo@labmec.unical.it)

**Keywords:** non-linear analysis, adaptive mesh.

**Abstract.** This paper deals with a boundary element algorithm for nonlinear analyses based on adaptive generation of the domain mesh. The automatic refinement is controlled by a tree structure. The algorithm is applied to the analysis of plane states following an initial stress formulation and using an iterative scheme based on the Riks' arc-length method. The boundary element discretization uses straight independent macro-element and B-spline interpolation functions. Domain integrals, which are singular in the nonlinear regions, are transferred to the cell boundary and computed numerically. Numerical results show application to plasticity and damage mechanics.

### Introduction

The Boundary Element Method allows accurate and fast elastic analyses using few variables. Structural problems with material nonlinearities typically show an inelastic behaviour only in limited parts of the domain, so its advantages could also be exploited in non-linear context. The earliest research into plasticity appeared in the seventies. In the last decade some papers dealing with damage mechanics and boundary elements have been published. However, it seems that the development of the method in non-linear analyses was not so fast. This was due to some difficulties in the formulation and some of efficiency in the solution strategies. Crucial tasks in non-linear BEM are an efficient monitoring of the evolution of the inelastic regions and a careful evaluation of the strong singular domain integrals.

In this work attention is paid to the description of the inelastic regions with an efficient domain mesh using an automatic adaptive refinement. This strategy allows a simple constant interpolation of the initial stress to be used. From an algorithmic point of view the evolution of the domain cells is handled by a tree structure and is carried out by recursive procedures. In order to obtain accuracy singular domain contributions ( $1/r^2$  singularities) are transferred on the cell boundaries.

An iterative scheme based on Riks' arc-length method is used. The algorithm is applied to plane analyses considering both the classical context of plasticity and damage mechanics. Some numerical results show the effectiveness of the proposed mesh refinement.

### Boundary Integral Formulation

In this section the equations based on an initial stress approach for a general nonlinear problem are briefly recalled. Considering a domain  $\Omega$  bounded by the boundary  $\Gamma$ , the Somigliana identity states a relationship between the boundary rates. A domain integral collects the contributions from the nonlinear regions represented by a field of initial stress  $\dot{\sigma}_{ij}^p$

$$c_{ij}\dot{u}_j[S] = \int_{\Gamma} u_{ij}^*[S, Q]\dot{t}_j[Q]d\Gamma - \int_{\Gamma} t_{ij}^*[S, Q]\dot{u}_j[Q]d\Gamma + \int_{\Omega} \varepsilon_{ijk}^*[S, q]\dot{\sigma}_{jk}^p[q]d\Omega \quad (1)$$

where body forces are equal to zero,  $S$  is the source point,  $Q$  and  $q$  are the field points (the first one lies on the boundary while the latter is inside the domain),  $c_{ij}$  depend on the geometry of the boundary,  $u^*$ ,  $t^*$  and  $\varepsilon^*$  are the fundamental solutions in terms of displacements, tractions and strains. The stress rate  $\dot{\sigma}_{ij}$  can be obtained from the eq. (1) using the constitutive relations

$$\dot{\sigma}_{ij}[s] = \int_{\Gamma} u_{ijk}^*[s, Q] \dot{t}_k[Q] d\Gamma - \int_{\Gamma} t_{ijk}^*[s, Q] \dot{u}_k[Q] d\Gamma + \int_{\Omega} \varepsilon_{ijkl}^*[s, q] \dot{\sigma}_{kl}^p[q] d\Omega + f_{ij}[\dot{\sigma}_{kl}^p[s]] \quad (2)$$

where  $f_{ij}$  is the free term derived from the singularity of  $\varepsilon_{ijkl}^*$  in  $s$ . The solution of the incremental problem stated by eqs. (1,2) can be obtained iteratively, using a return algorithm in order to make the solution admissible.

### Discrete Model

The boundary is divided into linear macro-elements and each can be subdivided into many elements. The interpolation function is a quadratic B-spline on each macro-element (see Fig. 1) previously used in elasticity [1,2]. This interpolation ensures  $C_1$  inter-element continuity with few parameters, without the explicit use of the derivatives. For this reason it is called HC (High Continuity) interpolation.

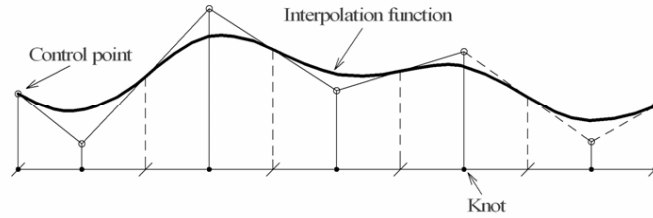


Fig. 1 - B-spline interpolation on a macro-element.

Considering  $n$  elements on a macro-element,  $(n + 2)$  parameters define the interpolation and  $(n + 2)$  sources are needed. Using a local reference system on each element, all the boundary integrals are computed in closed form and it is possible to assemble the system matrix quickly, with great accuracy. The incremental eq. (1) can be written, using typical symbols, in the following discrete form

$$H\dot{u} = G\dot{t} + p[\dot{\sigma}^p] \longrightarrow A\dot{x} = \dot{b} + p[\dot{\sigma}^p] \quad (3)$$

where  $\dot{x}$  is the rate of the boundary unknowns,  $\dot{b}$  is the rate of the known term depending on the boundary conditions and  $p$  represents the initial stress contribution from the nonlinear regions. The stress rate can be expressed similarly by

$$\dot{\sigma} = v[\dot{x}] + \dot{\tilde{b}} + \tilde{p}[\dot{\sigma}^p] \quad (4)$$

### Adaptive Domain Mesh

In a linear elastic analysis the boundary element method needs computational resources only on the boundary. A material nonlinear problem requires the monitoring of the domain for detecting nonlinearities and the computation of the initial stress integrals. In general we have no information about the location of the nonlinearities, and it would be too expensive to use a fine grid of control points over the whole domain. In order to save computational resources a refined control is required in the regions which are near to become nonlinear.

The task of recognizing the nonlinear regions and having a fine mesh in these zones is performed by an adaptive algorithm which generates cells following a refinement criterion based on a check of the elastic stress level. At the beginning of the analysis the stress state is monitored by few points. Each cell has a control point in the centroid and constant interpolation of the stress state is assumed over it. While the analysis proceeds the mesh automatically becomes finer in the regions where the elastic stresses increase. The increase in the mesh density is driven by assumed thresholds, fractions of the value which

activates the nonlinear response. When a threshold value is reached in a cell, four cells having the same structure are generated from it.

From a numerical point of view this kind of adaptive mesh can be effectively managed using a tree structure. Each cell is a record with some variables and four pointers to the parent cells. This kind of structure takes advantage of an efficient algorithmic implementation. In particular, recursive procedures are used to access the cells of the tree.

The constant interpolation of stresses on each cell is not so poor as it appears at first glance. It is worth noting that in the regions of interest a fine mesh is used whereas the remainder of the domain shows elastic behaviour and is well described by the boundary variables. The constant interpolation simplifies the semi-analytical integration of the domain integrals, consisting of the analytical transfer of the integrals on the cell boundaries where they are numerically computed.

**Iterative Solution**

The iterative solution of the equations written in incremental form

$$A\Delta x = \Delta\lambda b + p [\Delta\sigma^P] \tag{5a}$$

$$\Delta\sigma = v [\Delta x] + \Delta\lambda b + \tilde{p} [\Delta\sigma^P] \tag{5b}$$

can be performed in different ways. A general iteration scheme with fixed load increments has no chance to follow the equilibrium path near the limit point where almost zero stiffness occurs. In order to capture the softening branch it is necessary to drive the process with suitable control parameters.

Strategies considering the load factor as a further unknown to be computed in each step are known as arc-length methods [3]. These algorithms introduce a further constraint equation. Different choices for this equation characterize different arc-length schemes. These strategies, extensively used in finite element analyses, have been recently introduced in the boundary element context [4]. The constraint equation can be written in the form

$$\Delta x_j^T C \dot{x}_j + c \Delta\lambda_j \dot{\lambda}_j = 0 \tag{6}$$

This equation imposes the orthogonality (see Fig. 2) between the iterative corrections of the variables  $(\dot{x}_j, \dot{\lambda}_j)$  and the total increments in the step  $(\Delta x_j, \Delta\lambda_j)$ , using the metric defined by  $C$  and  $c$ .

The algorithm is based on an elastic prediction and an iterative loop. For each step the residual  $r_j$  is computed from the boundary equation

$$r_j = \hat{b}\Delta\lambda_j + p_j - A\Delta x_j = p_j - p_{j-1} \tag{7}$$

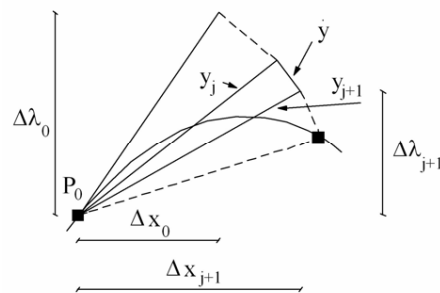


Fig. 2 - Arc-length iteration scheme.

The corrector phase looks for the increments  $\Delta x_{j+1}, \Delta \lambda_{j+1}$  satisfying the following equations

$$\begin{cases} r_j[\Delta x_{j+1}, \Delta \lambda_{j+1}] & = 0 \\ \Delta x_j^T C(\Delta x_{j+1} - \Delta x_j) + c\Delta \lambda_j(\Delta \lambda_{j+1} - \Delta \lambda_j) & = 0 \end{cases} \quad (8)$$

Therefore the load increment can be written as

$$\Delta \lambda_{j+1} = \frac{\Delta x_j^T C \Delta x_j + c\Delta \lambda_j^2 - \Delta x_j^T C A^{-1} p_j}{\Delta x_j^T C A^{-1} \hat{b} + c\Delta \lambda_j} = 0 \quad (9)$$

It is worth noting that the arc-length control can be imposed only for the boundary displacement ( $x = u$ ) and simple hypotheses  $C = I$  and  $c = 0$  are enough. With these choices the iterative scheme can be expressed by

$$\Delta \lambda_{j+1} = \frac{\Delta x_j^T (\Delta x_j - A^{-1} p_j)}{\Delta x_j^T \Delta_0} \quad (10)$$

$$\Delta x_{j+1} = b_0 \Delta \lambda_{j+1} + A^{-1} p_j \quad (11)$$

where  $b_0 = A^{-1} \hat{b}$  is the elastic solution and  $p_j$  is evaluated from the contribution  $\Delta \sigma_j^p$  that makes the stress state  $\sigma_0 + \Delta \sigma_j - \Delta \sigma_j^p$  admissible.

**Numerical Results**

The algorithm described in the previous sections, based on an initial stress approach, is able to deal with general material nonlinearities, such as plasticity and damage. The different constitutive laws are modelled by different return algorithms which correct the solution when it is not admissible. In the case of plasticity a general return mapping algorithm is used in order to obtain the projection on the admissible stress surface. In the context of damage the process iteratively looks for the damage increment that renders the strains admissible for the assumed damage function.

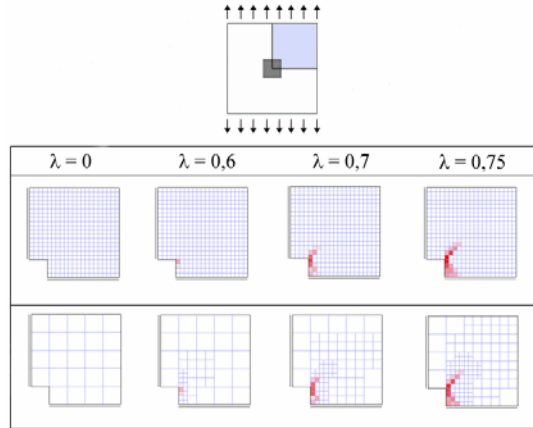


Fig. 3 - Adaptive mesh and plastic work at different loads.

The numerical tests for plasticity problems show the efficiency of the adaptive algorithm. For the tension test (see Fig. 3), the number of cells is significantly reduced in comparison with the uniform mesh, with a great saving in CPU time.

The second test deals with a square plate (see Fig. 4) subjected to a tangential load, using the damage model proposed by Comi and Perego [5] for quasi-brittle materials and used in a boundary element model by Botta et al. [6]. The iterative solution method follows the equilibrium path beyond the limit point. In Fig. 5 the evolutions of the stresses and of the damage level are plotted.

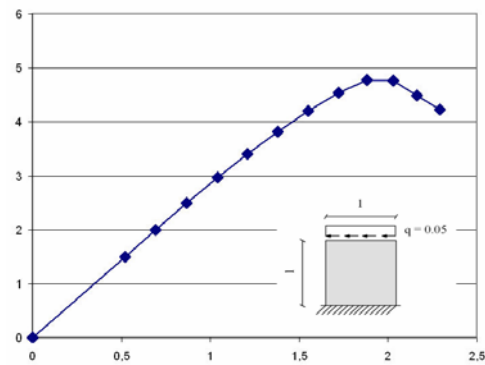


Fig. 4 - Equilibrium path for the plate under tangential load.

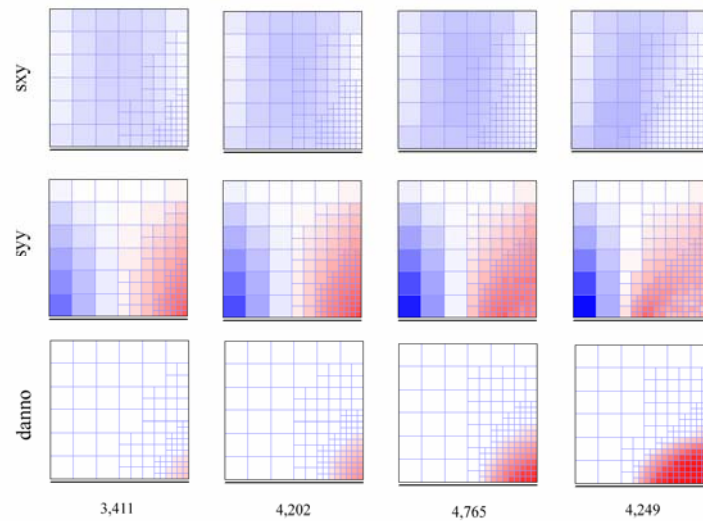


Fig. 5 – Stresses and damage at different load levels.

**References**

- [1] M. Aristodemo and E. Turco *International Journal for Numerical Methods in Engineering*, **37**, 965-987 (1994).
- [2] D. Gaspari and M. Aristodemo *Engineering Analysis with Boundary Elements*, **29/9**, 850-858 (2005).
- [3] E. Riks *International Journal of Solids and Structures*, **15**, 529-551 (1979).
- [4] V. Mallardo and C. Alessandri *Engineering Analysis with Boundary Elements*, **28**, 547-559 (2004).
- [5] C. Comi and U. Perego *International Journal of Solids and Structures*, **38**, 6427-6454 (2001).
- [6] A.S. Botta, W.S. Venturini, A. Benallal *Engineering Analysis with Boundary Elements*, **29**, 814-827 (2005).

## The Integral Boundary Method for the analysis of mid-frequency NVH problems

A. Pratellesi<sup>1</sup>, M. Pierini<sup>1</sup>, N. Baldanzini<sup>1</sup>, M. Viktorovitch<sup>2</sup>

<sup>1</sup> Dipartimento di Meccanica e Tecnologie Industriali, UNIFI, Via  
S.Marta 3, 50139 Firenze, Italia,  
[alessandro.pratellesi@unifi.it](mailto:alessandro.pratellesi@unifi.it), [marco.pierini@unifi.it](mailto:marco.pierini@unifi.it),  
[niccolo.baldanzini@unifi.it](mailto:niccolo.baldanzini@unifi.it)

<sup>2</sup> RIETER Automotive Mgt AG, Schlosstalstrasse, 43, CH-8406 Winterthur, Switzerland,  
[Michel.Viktorovitch@rieterauto.com](mailto:Michel.Viktorovitch@rieterauto.com)

**Abstract.** In the NVH analysis of car structures, there are manifold applications dealing with fluid-structure coupling and vibro-acoustic responses affected from uncertainties especially in the mid- and high frequency range. In this paper a probabilistic formulation based on BEM, able to account for the uncertainties in the geometric description of structures, is presented. The starting point is the classical integral boundary formulation, introducing a probabilistic description of the boundaries, which is solved in terms of expected values. The method, named SIF, can be applied to both acoustic domains and structures. In this paper some application of this method to 2D systems are reported. When dealing with systems made of components which exhibit different vibro-acoustic behaviour as a function of frequency, the probabilistic formulation can be coupled with deterministic methods, like FEM and BEM, to obtain a consistent formulation. The results obtained coupling the SIF with BEM or FEM, and solving some mid-frequency problems are reported in this paper. Those results prove that the application of the boundary element method to NVH problem, affected from uncertainties, leads to relevant results.

### Introduction

The automotive industry is used to divide the vibro-acoustic analysis into three different ranges according to frequency value and to structure behaviour.

First, the low frequency range is identified as the domain for which the investigations are mainly focused on the structure-borne contributions. In this frequency domain, the finite element method (FEM) [1] and classical direct and indirect boundary element methods (BEM) [2,3] yield effective numerical solutions.

Second, the high frequency field is the domain for which the air-borne contribution is predominant and for which the classical simulation tools involve a huge number of degrees of freedom. Employing these formulations leads to high computing time and thus, alternative formulations such as the Statistical Energy Analysis (SEA) [4] are generally employed in the high frequency domain. Moreover, when dealing with structures which exhibit HF behaviour in the frequency range of analysis, also the effect of uncertainties must be included. Using the classical boundary method to predict the behaviour of structures in the high frequency field is numerically possible but physically unrealistic. The reason is that the deterministic response of any mechanical system is more and more sensitive to small perturbations of the geometrical and mechanical parameters of the structures, as the frequency increases.

The mid-frequency field is usually defined as the domain for which a complex vibrating structure may be divided into parts which have deterministic "low-frequency" behaviour, and parts which present "high-frequency" behaviour. This combination of high- and low-frequency behaviour implies that the structure-borne contribution may not be neglected, as in a SEA model, but, on the other hand, the classical low-frequency predictive tools are ineffective for modelling the "high-frequency" part.

In view of some characteristic properties of the mid-frequency dynamic behaviour of vibro-acoustic systems, the prediction techniques should meet the following requirements:

- The prediction techniques must be applicable for general, real-life vibro-acoustic engineering applications.

- In contrast with SEA models, in which all local information is lost, the prediction techniques should still provide detailed information on the spatial distribution of the mid-frequency response variables within the various components of the considered vibro-acoustic system.
- The prediction techniques must account for the effects of product and process variability and provide ensemble statistics of the mid-frequency dynamic behaviour.
- Many engineering structures, especially built-up structures such as vehicles, trains, truck cabins, etc., have a particular mid-frequency dynamic behaviour: parts of the structure consist of stiff and strongly connected components that still exhibit long wavelength dynamic deformations in the mid-frequency range, while other parts exhibit already a highly resonant behaviour with short wavelength deformations. The mid-frequency prediction techniques should enable a hybrid modelling approach in which the long wavelength components are modelled deterministically, while the short wavelength components are described in a probabilistic manner.

The aim of this paper is to present a statistical formulation, the SIF, based on the BEM integral formulation, to model the vibro-acoustic behaviour of structures in the mid and high-frequency ranges. This method can be effectively coupled with classical deterministic methods to obtain a hybrid formulation suited for the mid-frequency applications. Two different numerical applications of SIF formulation are presented: an acoustic analysis of a 2D acoustic domain affected from uncertainties, and the vibro-acoustic modelling of a mid-frequency structure made of an HF acoustical domain coupled with two LF beams. The second application has been chosen in order to show the effectiveness of the method when dealing with fluid-structure coupling, and to illustrate the application of the hybrid method.

#### The SIF formulation

In the mid nineties, Viktorovitch et al. [5,6] developed a novel formulation, the Smooth Integral Formulation (SIF), valid on the whole frequency domain but whose practical application was the high frequency field. The fundamental idea of this work relied on the assumption that the dynamic behaviour of any mechanical system is intrinsically random, and the influence of this randomness grows with the frequency. The analytical formulation is based on the dynamic boundary integral equations. These integral equations are multiplied by well-chosen variables, in order to obtain a formulation governing the cross product of the kinematic variables. Gaussian randomness is then introduced to the geometrical parameters of the structures and the stochastic expectations of the terms in the new integral equations are taken into account. Some assumptions are introduced to limit the number of high order moment unknowns. Finally, the unknowns of the new formulation are the second order stochastic moments of the boundary kinematic variables.

**The boundary integral representation for second order differential governing equations.** The initial stage for deriving the SIF equations is a direct boundary integral formulation. The integral representation for a homogeneous, isotropic and linear mechanical system of domain  $\Omega$  and smooth boundary  $\partial\Omega$ , subjected to a harmonic loading  $f$  on boundary  $\partial\Omega_f$ , may be written:

$$c \cdot u(\xi) = \int_{\Omega_f} f(\mathbf{y})G(\mathbf{y}, \xi) d\Omega + \int_{\partial\Omega} [u(\mathbf{x}) \cdot dG(\mathbf{x}, \xi) - T(\mathbf{x}) \cdot G(\mathbf{x}, \xi)] d\partial\Omega \quad (1)$$

the integral representation is completed with the following boundary conditions:

$$\begin{cases} u(\mathbf{x}) = \hat{u}(\mathbf{x}) & \text{on } \partial\Omega_u \\ T(\mathbf{x}) = \hat{T}(\mathbf{x}) & \text{on } \partial\Omega_T \end{cases} \text{ and } \begin{cases} c = \frac{1}{2} & \xi \in \partial\Omega \\ c = 0 & \text{otherwise} \end{cases}$$

where  $u(\mathbf{x})$  is the kinematic unknown (e.g. pressure, displacement),  $T(\mathbf{x})$  is the boundary force unknown,  $G$  denotes the Green kernel,  $dG$  is the first order derivative of the Green kernel with respect to the variable  $\mathbf{x}$ ,  $\partial\Omega_u$  and  $\partial\Omega_T$  constitute a partition of  $\partial\Omega$ .

The formulation is very general and stands for one-, two- and three-dimensional problems.

**The random formulation.** The general idea of the formulation is based on the introduction of randomness to the description of the geometry of the structure. This randomness does not affect the

predictions in the low frequency field; on the other hand, the response is extremely sensitive to any structural perturbation in the high frequencies.

The SIF formulation can be developed starting from eq.(1): the locations of the loading and the boundary of the structure are then randomized. These two new random parameters are respectively denoted by  $\tilde{\Omega}_f$  and  $\partial\tilde{\Omega}$ . Accordingly, the partition of the boundary defined in the previous subsection, becomes  $\partial\tilde{\Omega} = \partial\tilde{\Omega}_u + \partial\tilde{\Omega}_T$ . The task of this work is to derive an integral representation whose unknowns are the expectations of the cross product of the force and displacement unknowns. Therefore, for any boundary location  $\tilde{\xi} \in \partial\tilde{\Omega}$ , the right- and left-hand sides of the integral equations are multiplied by the conjugate of the random boundary unknown at the same spatial position. The collocation method is then employed, which enables the transformation of the integral equations into a discrete set of equations. As an illustration, the equation evaluated at point  $\tilde{\xi} \in \partial\tilde{\Omega}_u$  is reported.

$$\begin{aligned} \frac{1}{2} \cdot \tilde{u}_j &= \int_{\tilde{\Omega}_f} f(\mathbf{y}) \cdot G(\mathbf{y}, \tilde{\xi}) d\Omega \\ &+ \sum_{j=1}^{N_T} \int_{\partial\tilde{\Omega}_j} \left[ \hat{u}_j \cdot dG(\mathbf{x}, \tilde{\xi}) - \hat{T}_j \cdot G(\mathbf{x}, \tilde{\xi}) \right] d\partial\Omega \\ &+ \sum_{k=1}^{N_u} \int_{\partial\tilde{\Omega}_k} \left[ \hat{u}_k \cdot dG(\mathbf{x}, \tilde{\xi}) - \hat{T}_k \cdot G(\mathbf{x}, \tilde{\xi}) \right] d\partial\Omega \end{aligned} \quad (2)$$

In eq.(2)  $\tilde{u}_j$  is the boundary random unknown at element  $j$ ,  $\hat{u}_j$  and  $\hat{T}_k$  are the boundary conditions respectively at location  $j$  and  $k$ .

The expectations of the equations are considered. They are represented by  $\langle - \rangle$ .

Finally, one obtains  $N_u + N_T$  boundary element equations, where  $N_u$  and  $N_T$  are the number of boundary elements defined for  $\partial\tilde{\Omega}_u$  and  $\partial\tilde{\Omega}_T$  respectively.

**Limiting the number of unknowns and derivation of the final formulation.** To solve the  $N_u + N_T$  equations some statistical assumptions for limiting the number of unknowns were defined. These assumptions rule the correlation of the different variables appearing in the equations above. They are based on a physical interpretation of the integral equations.

The right-hand side of the integral equation, eq.(2) are interpreted as the sum of the contributions of extended sources located on the boundary elements of the structure, plus the contributions of the external loadings. The amplitude of these sources are the boundary unknowns and the value of the external loading  $f(\mathbf{x})$ .

The first assumption deals with the statistical behaviour of the different sources.

*Assumption 1:* The contributions of two sources are statistically independent when the positions of the source or the target points of the contributions are distinct.

Two types of sources are distinguished: the external loadings which are called primary sources and the boundary sources (on which no loading is applied) which are called secondary sources. The latter are constituted by the multiple wave reflections of the waves stemming from the loadings. The second assumption rules the random behaviour of the force and displacement variables.

*Assumption 2:* It is considered that a force or a displacement variable expressed at any point of the structure, is only correlated with the contributions of the primary sources at that point.

Finally, applying the two assumptions, and assuming a constant value of the boundary unknown over the element extension, the fundamental equation of the formulation may be written:

- $\tilde{x}_i \in \partial\tilde{\Omega}_i, i \in [1, N_T]$ :

$$\begin{aligned} \frac{1}{2} \cdot \langle |u_i|^2 \rangle &= \langle \tilde{u}_i^* \cdot \int_{\tilde{\Omega}_f} f(\mathbf{y}) \cdot G(\mathbf{y}, \tilde{x}_i) d\Omega \rangle \\ &+ \langle \tilde{u}_i^* \cdot \sum_{j=1, j \neq i}^{N_T} \langle \tilde{u}_j \rangle \cdot \left\langle \int_{\partial\tilde{\Omega}_j} dG(\mathbf{x}, \tilde{x}_i) d\partial\Omega \right\rangle - \langle \tilde{u}_i^* \rangle \cdot \sum_{j=1}^{N_T} \left\langle \int_{\partial\tilde{\Omega}_j} \hat{T}(\mathbf{x}) \cdot G(\mathbf{x}, \tilde{x}_i) d\partial\Omega \right\rangle \end{aligned} \quad (3)$$

$$\begin{aligned}
& + \langle \tilde{u}_i^* \rangle \cdot \sum_{k=1}^{N_u} \left\langle \int_{\partial\tilde{\Omega}_k} \hat{u}(\mathbf{x}) \cdot dG(\mathbf{x}, \tilde{\mathbf{x}}_i) d\partial\Omega \right\rangle - \langle \tilde{u}_i^* \rangle \cdot \sum_{k=1}^{N_u} \langle \tilde{T}_k \rangle \cdot \left\langle \int_{\partial\tilde{\Omega}_k} G(\mathbf{x}, \tilde{\mathbf{x}}_i) d\partial\Omega \right\rangle \\
& + \langle |\tilde{u}_i|^2 \rangle \cdot \int_{\partial\tilde{\Omega}_i} dG(\mathbf{x}, \tilde{\mathbf{x}}_i) d\partial\Omega
\end{aligned}$$

•  $\tilde{\mathbf{x}}_i \in \partial\tilde{\Omega}_i, i \in [1, N_u]$ :

$$\begin{aligned}
& \frac{1}{2} \cdot \langle \tilde{T}_i^* \rangle \cdot \hat{u}_i = \langle \tilde{T}_i^* \rangle \cdot \int_{\tilde{\Omega}_i} f(\mathbf{y}) \cdot G(\mathbf{y}, \tilde{\mathbf{x}}_i) d\Omega \\
& + \langle \tilde{T}_i^* \rangle \cdot \sum_{j=1}^{N_T} \langle \tilde{u}_j \rangle \cdot \left\langle \int_{\partial\tilde{\Omega}_j} dG(\mathbf{x}, \tilde{\mathbf{x}}_i) d\partial\Omega \right\rangle - \langle \tilde{T}_i^* \rangle \cdot \sum_{j=1}^{N_T} \left\langle \int_{\partial\tilde{\Omega}_j} \hat{T}_j(\mathbf{x}) \cdot G(\mathbf{x}, \tilde{\mathbf{x}}_i) d\partial\Omega \right\rangle \\
& + \langle \tilde{T}_i^* \rangle \cdot \sum_{k=1}^{N_u} \left\langle \int_{\partial\tilde{\Omega}_k} \hat{u}(\mathbf{x}) \cdot dG(\mathbf{x}, \tilde{\mathbf{x}}_i) d\partial\Omega \right\rangle - \langle \tilde{T}_i^* \rangle \cdot \sum_{k=1, k \neq i}^{N_u} \langle \tilde{T}_k \rangle \cdot \left\langle \int_{\partial\tilde{\Omega}_k} G(\mathbf{x}, \tilde{\mathbf{x}}_i) d\partial\Omega \right\rangle \\
& + \langle |\tilde{T}_i|^2 \rangle \cdot \int_{\partial\tilde{\Omega}_i} G(\mathbf{x}, \tilde{\mathbf{x}}_i) d\partial\Omega
\end{aligned} \tag{4}$$

Equations (3) and (4) are the fundamental relationships of the Smooth Integral Formulation. Studying these equations one can observe that the number of unknowns is equal to  $3(N_u + N_T)$ . These unknowns are:

- First order moments:  $\langle \tilde{u}_i \rangle$  and  $\langle \tilde{T}_i \rangle$ .
- Second order moments:  $\langle |\tilde{u}_i|^2 \rangle$  and  $\langle |\tilde{T}_i|^2 \rangle$ .
- Expectation of kinematic variable multiplied by the contribution of the primary source:  $\left\langle \tilde{u}_i^* \cdot \int_{\tilde{\Omega}_i} f(\mathbf{y}) \cdot G(\mathbf{y}, \tilde{\mathbf{x}}_i) d\Omega \right\rangle$  and  $\left\langle \tilde{T}_i^* \cdot \int_{\tilde{\Omega}_i} f(\mathbf{y}) \cdot G(\mathbf{y}, \tilde{\mathbf{x}}_i) d\Omega \right\rangle$ .

In order to obtain a consistent set of equations,  $2(N_u + N_T)$  supplementary equations are added to the formulation.  $N_u + N_T$  equations are the expectation of the basic equation (2) evaluated in  $\tilde{\xi} = \tilde{\mathbf{x}}_i \in \partial\tilde{\Omega}_i$ ,  $i = 1, 2, \dots, N_u + N_T$ . The remaining  $N_u + N_T$  equations come from the conjugate basic equation multiplied by the contribution of the external force  $\int_{\tilde{\Omega}_i} f(\mathbf{y}) \cdot G(\mathbf{y}, \tilde{\mathbf{x}}_i) d\Omega$ , evaluated in  $\tilde{\xi} = \tilde{\mathbf{x}}_i \in \partial\tilde{\Omega}_i$ ,  $i = 1, 2, \dots, N_u + N_T$ .

#### Application of SIF

As an example, the SIF is applied in this paper to a square 2D domain, Fig. 1, characterized by Helmholtz equation. The boundaries,  $S_p$ , of the domain are divided into  $N_p$  elements.  $dp_0$  is the external excitation acting on the domain which is supposed to have pressure release boundary conditions:

$$p(\mathbf{r}_i) = 0 \quad i = 1 : N_p$$

The general BEM equation for Helmholtz problems, for  $i = 1 : N_p$ , reduces to:

$$0 = \sum_{k=1}^{N_p} \frac{\partial p(\mathbf{r}_k)}{\partial \mathbf{n}_k} \cdot \int_{S_k} G(\mathbf{r}, \mathbf{r}_i) dS + \int_{S_f} dp_0 \cdot G(\mathbf{y}, \mathbf{r}_i) dS \quad (5)$$

Randomness is introduced in the boundary description, eq. (5), and it is indicated by  $\tilde{\mathbf{r}}$ .

$$0 = \sum_{k=1}^{N_p} \frac{\partial p(\tilde{\mathbf{r}}_k)}{\partial \tilde{\mathbf{n}}_k} \cdot \int_{S_k} G(\mathbf{r}, \tilde{\mathbf{r}}_i) dS + \int_{S_f} dp_0 \cdot G(\mathbf{y}, \tilde{\mathbf{r}}_i) dS \quad (6)$$

The SIF equations, according to procedure developed on the former section, are obtained multiplying each side of the basic equations (6) for the conjugate of the boundary unknowns,  $\partial p^*(\tilde{\mathbf{r}}_i) / \partial \mathbf{n}_i$ , and getting the expectation.

For  $i = 1 : N_p$ ,  $\tilde{\mathbf{r}}_i \in \tilde{S}_p$ :

$$0 = \left\langle \left| \frac{\partial p(\tilde{\mathbf{r}}_i)}{\partial \tilde{\mathbf{n}}_i} \right|^2 \right\rangle \cdot \left\langle \int_{\tilde{S}_i} G(\mathbf{r}, \tilde{\mathbf{r}}_i) dS \right\rangle + \left\langle \frac{\partial p^*(\tilde{\mathbf{r}}_i)}{\partial \tilde{\mathbf{n}}_i} \right\rangle \cdot \sum_{k=1, k \neq i}^{N_p} \left\langle \frac{\partial p(\tilde{\mathbf{r}}_k)}{\partial \tilde{\mathbf{n}}_k} \right\rangle \cdot \left\langle \int_{\tilde{S}_i} G(\mathbf{r}, \tilde{\mathbf{r}}_i) dS \right\rangle + \left\langle \frac{\partial p^*(\tilde{\mathbf{r}}_i)}{\partial \tilde{\mathbf{n}}_i} \right\rangle \cdot \int_{\tilde{S}_i} dp_0 \cdot G(\mathbf{y}, \tilde{\mathbf{r}}_i) dS \quad (7)$$

The unknowns of the formulation, in eqs. (7), are clearly the expectation of the square modulus of the boundary unknowns  $\left\langle \left| \frac{\partial p(\tilde{\mathbf{r}}_i)}{\partial \tilde{\mathbf{n}}_i} \right|^2 \right\rangle$ , for  $i = 1 : N_p$ .

The auxiliary equation are the expectation of equations (6), to evaluate the first order moments, and the conjugate of equations (6) multiplied by the contribution of the primary source  $\int_{\tilde{S}_i} dp_0 \cdot G(\mathbf{y}, \tilde{\mathbf{r}}_i) dS$ .

The total number of unknowns is  $3N_p$ .

The mechanical and geometrical properties of the structure are given in Table 1, properties which have been selected in such a manner that the membrane has a mid- high-frequency behaviour in the frequency range of interest.

Table 1: Acoustic 2D domain: Geometrical and physical properties of the Acoustic domain

	Side Length [m]	Sound speed [m/s]	Density [kg/m <sup>3</sup> ]	$\eta$ %
Acoustic domain	1	50.5	10.5	0.02

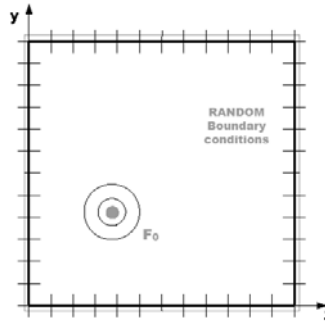


Figure 1: Acoustic 2D domain

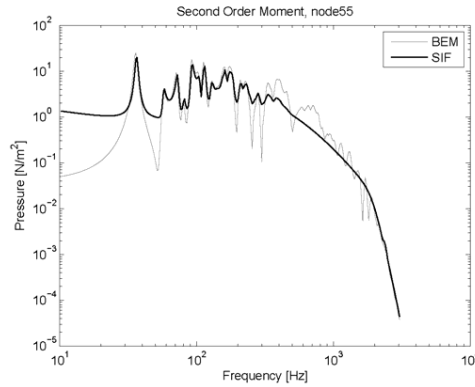


Figure 2: Acoustic 2D domain: Frequency variation of the second order moments of a boundary unknown. Comparison of the deterministic result with the SIF predictions.

The observation of the curves represented in Figure 2 highlights some important elements concerning the effectiveness of the random formulation. At first, one can globally state that the influence of the randomness increases with frequency. The SIF curves give a precise representation of the modal behavior in the low-frequency range. On the other hand, the high-frequency behavior of the random formulation simulation is smooth and only delivers information on the general trend of the frequency variation of the boundary unknowns.

**Application of FEM-SIF hybrid formulation**

The SIF formulation is now coupled with FE to develop and test a hybrid formulation for mid-frequency application. The hybrid formulation is based on FEM-BEM method for fluid-structure

coupling [7,8]. The system is made of a HF acoustical domain, modelled with SIF, coupled with two LF beams, modelled with FEM. The external excitation is located on a beam, Figure 3. The geometrical and physical properties of the structure are reported in Table 2.

Table 2: Mid-frequency structure: Geometrical and physical properties

	Side Length [ m ]	Sound speed [ m/s ]	Density [ kg/m <sup>3</sup> ]	$\eta$ %
Acoustic domain	1	79.5	76.5	0.02

	Length [ m ]	E [ N/m <sup>2</sup> ]	Section Area [ m <sup>2</sup> ]	Density [ kg/m <sup>3</sup> ]	Iz [ m <sup>4</sup> ]	$\eta$ %
Beam 1	1	$2 \cdot 10^{11}$	$2.5 \cdot 10^{-3}$	7800	$3.25 \cdot 10^{-6}$	0.01
Beam 2	1	$1.9 \cdot 10^{11}$	$3.1 \cdot 10^{-3}$	7700	$3.98 \cdot 10^{-6}$	0.01

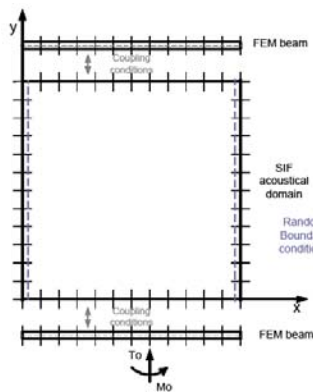


Figure 3: Mid-frequency structure, two beams-acoustic domain: acoustic random domain coupled with two deterministic beams.

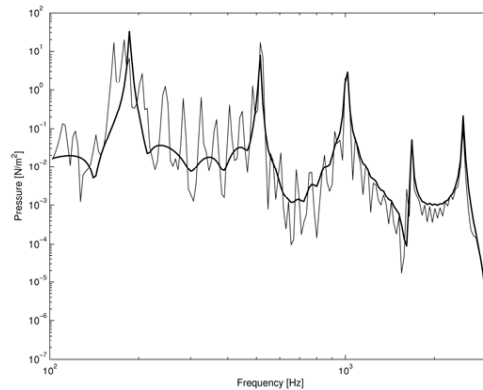


Figure 4: FEM-SIF formulation for mid-frequency application, two beams-acoustic domain: frequency variation of the second order moment at boundary point on the uncoupled side of the domain. Comparison of the deterministic result, FEM-BEM, with the SIF predictions.

We obtain a smooth contribution for the unknowns of the random acoustical domain, and a detailed description of the contribution of the deterministic beam. Figure 4 illustrates that coupling FEM and SIF theory leads to relevant results when dealing with mid-frequency structures.

### Conclusions

The SIF formulation is a statistical method for vibro-acoustic analysis of uncertain structure. It is based on the classical integral boundary formulation. Then, introducing a statistical description of boundary locations and solving in terms of expected values, it is possible to obtain results which are valid on the whole frequency range and account for the importance of uncertainties in the mid and high-frequency fields.

In this paper the development of the statistical method is reported, starting from the BEM formulation. Two numerical applications, a random acoustic domain and a fluid-structure problem, confirm the effectiveness and the capabilities of the formulation, also when coupled with a deterministic formulation.

### References

- [1] C. Zienkiewicz and R.L. Taylor, *The finite Element Method*, Vol. 1, 2 (fourth edition), (McGraw-Hill, London, 1991).

- [2] R. Butterfield and K. Bannerjee, *Boundary Element Methods in Engineering Science*, (New York, 1981).
- [3] C. A. Brebbia, *The Boundary Element Method for Engineers*, (Pentech, London, 1984).
- [4] R.H. Lyon, *Statistical Energy Analysis of Dynamical Systems*, (Cambridge, Massachusetts, 1975).
- [5] M. Viktorovitch, F. Thouverez, and L. Jezequel, *A new random boundary element formulation applied to high frequency phenomena*. *Journal of Sound and Vibration*, 223(2), 273–296, (1999).
- [6] M. Viktorovitch, F. Thouverez, and L. Jezequel, *An integral formulation with random parameters adapted to the study of the vibrational behavior of structures in the mid and high-frequency field*. *Journal of Sound and Vibration*, 247(3), 431 – 452, (2001).
- [7] G.C. Everstine, *Finite elements formulations of structural-acoustics problems*, *Computers & Structures*, 65 (3), 307-321, 1997.
- [8] A. Alia and M. Souli, *Simulation of vibroacoustic problem using coupled FE/BE formulation*, EURO-DYN 2005 Conference, 4-7 September 2005, Paris.



## Assessment of allowable dents on aeronautic panels based on the coupled usage of FEM-DBEM methodology.

C. Cali, R. Citarella, G. Cricri

University of Salerno, dept. of Mechanical Engineering, Fisciano (SA), Italy, rcitarella@unisa.it

**Keywords:** Coupled FEM-DBEM, allowable dent, crack propagation, internal stress

**Abstract.** This paper describes an original implementation of a two-parameters crack growth model for 2D crack propagation simulations in a dented panel undergoing a fatigue load (dents are typical damages observed in service on aircraft fuselage). In such model, in order to unify the damage process, three basic parameters are introduced for describing the overall fatigue process:  $\Delta K$ ,  $K_{max}$  and the internal stress contribution to  $K_{max}$ . The implementation is based on the coupled usage of Finite Element Method (FEM) and Dual Boundary Element Method (DBEM), in order to take advantage of the main capabilities of the two methods. The procedure capability to predict the impact of residual stresses, induced by plastic deformation, on crack growth rates is assessed by comparison with experimental results. The main advantages of the aforementioned procedure are: the simplicity of the crack growth law calibration (few constant amplitude tests on undamaged panels are sufficient without the need for any non physical calibration parameters), and the possibility to simulate plastic deformation effects on crack propagation with a simplified approach, based on linear elastic fracture mechanics. The plastic effects are simulated by body loads, previously calculated by an elastic-plastic FEM analysis, that are introduced in a linear elastic DBEM analysis. The level of accuracy coming from the realized tests is judged satisfactory.

### Introduction

In this paper the implementation of a two-parameters crack growth model [1-5], is recalled and its application to a mode I crack propagation problem is described in details. The coupled usage of Finite Element Method (FEM) and Dual Boundary Element Method (DBEM) is proposed in order to take advantage of the main capabilities of the two methods: FEM is more efficient for elastic-plastic analysis (needed in this case to assess the residual stress profile) whilst DBEM allows an efficient automatic crack propagation, especially for complex geometry or for mixed mode conditions. In particular, the DBEM, as implemented in a commercial code [6], is adopted for the crack propagation simulation, whereas an elastic-plastic analysis made with the FEM code ANSYS is used to calculate the residual stresses induced by the denting process. The proposed application is verified against a series of laboratory tests, in order to evaluate its capability to predict the way in which the crack growth phenomena is affected by the plastic deformations in the cracked area.

### Two-parameters crack propagation law

In presence of a plastic deformation around the cracked area, the stress field at the crack tip is altered by residual stresses. The basic effect of these residual stresses is to change the effective values of the total Stress Intensity Factors (SIFs) at the crack tip, with both  $K_{min}$  and  $K_{max}$  generally affected in the same way, so as to leave unchanged the parameter  $\Delta K$ . Consequently, the primary effects of residual stresses on crack growth rates are related to the  $K_{max}$  variations and not to the  $\Delta K$  variations. This is accounted for by the two parameters approach: according to this theory, fatigue crack growth can be viewed, fundamentally, as a two-parametric problem, where two driving forces,  $K_{max}$  and  $\Delta K$ , drive the growth of a fatigue crack. Since it is assumed that, in presence of an overload,  $K_{max}$  also enters as the major driving force for fatigue crack growth (in addition to the classical parameter  $\Delta K$ ), the corresponding residual stresses can affect the crack growth rates even if they do not affect the parameter  $\Delta K$ . In addition, the theory assumes that there are two fatigue thresholds,  $K_{max,th}^*$  and  $\Delta K_{th}^*$ , corresponding to the two driving forces. These are asymptotic values in the  $\Delta K$ - $K_{max}$  graphs of the fatigue curves, and the driving forces must be both simultaneously larger than the relative thresholds for fatigue crack growth to occur.

Since residual stress effects manifest primarily through a reduction in  $K_{max}$  levels, a crack growth rate retardation generally follows the overload, and an arrest in crack growth can occur if these stresses are sufficiently high (i.e.  $K_{max}$  falls below  $K_{max,th}^*$ ).

The crack growth law (as defined by Vasudevan [1-2]) is assumed to be of the form:

$$\frac{da}{dN} = A (\Delta K - \Delta K_{th}^*)^n (K_{max} - K_{max,th}^*)^m \quad (1)$$

and is calibrated by best fitting the material parameters  $A$ ,  $n$ ,  $m$  based on constant amplitude preliminary tests. The threshold parameters  $K_{max,th}^*$  and  $\Delta K_{th}^*$  are evaluated by experimental tests as well.

The impact on the driving forces  $\Delta K$  and  $K_{max}$  of the residual stresses induced by a plastic deformation in the area surrounding the crack is calculated and, finally, the crack growth model is applied. It is remarkable that the two parameter crack growth law, whose validity is expected to be extended to any plastic deformation within the range of small deformation, is calibrated using only experimental data from constant amplitude tests.

#### Crack growth law fatigue parameters

**Determination of the threshold parameters ( $\Delta K_{th}^*$ ,  $K_{max,th}^*$ ).** Due to the lack of experimental propagation data in the threshold range, the experimental threshold data for the aluminum alloy 6056 T78 are assumed equal to those of the aluminum alloy 2024 HPT3 [3-4],  $\Delta K_{th}^* = 58 \text{ N/mm}^{3/2}$  and  $K_{max,th}^* = 106 \text{ N/mm}^{3/2}$ . Another approximation is related to the fact that the CT specimens used for the threshold assessment are 3.2 mm thick, whilst the dented coupon under investigation is 1.2 mm thick (this could have a non negligible impact on the threshold values).

**Determination of material parameters ( $A$ ,  $n$ ,  $m$ ).** The material parameters ( $A$ ,  $n$ ,  $m$ ) in equation (1) are chosen as best fitting coefficient to interpolate data, taken at different R-ratios (from 0.1 to 0.9) in the range of  $\Delta K = 200:700 \text{ MPa} \cdot \text{mm}^{0.5}$  (Fig. 1), from the following Elber law (Eq. 3), valid for 6056 T78 unclad weldable alloys and for a thickness in the range 0.8-3.2 mm:

$$da/dN = C_{eff} (A + B \cdot R)^n \Delta K^n \quad (3)$$

$$\text{with } C_{eff} = 1.608 \cdot 10^{-7}; \quad A = 0.61; \quad B = 0.39; \quad n = 3.5$$

obtaining:  $A = 2.69 \cdot 10^{-11}$ ,  $n = 2.08$ ,  $m = 0.696$ .

#### Experimental test

The analysed coupons were tested during the European project ‘‘IARCAS’’ (VI framework) in the EADS CCR laboratories. They were dented (Fig. 2) and, afterwards, fatigue cycled up to rupture (Figs. 3a-b), with a traction load applied along the longitudinal specimen direction. In such conditions the crack initiation came out on the denting side. The tested coupon, made of aluminium alloy 6056 T78, have the following geometric dimensions and mechanical properties (Fig. 2):

- Thickness: 1.2 mm; Specimen length: 750 mm; Specimen width: 220 mm; Dent residual depth: 5 mm; Indenter radius: 50 mm; Young modulus  $E = 72 \text{ GPa}$ , Poisson coefficient  $\nu = 0.3$ .

#### Coupled FEM-DBEM numerical procedure

**Introduction.** The numerical FEM-DBEM procedure is based on the following steps:

1. calculate the residual stress scenario after denting, by means of a static elastic-plastic FEM analysis that simulate the skin-indenter impact. The 6056 T78 behaviour is defined by the following yielding and rupture values:  $F_y = 315 \text{ MPa}$  and  $F_u = 325 \text{ MPa}$ . The base hypothesis are isotropic hardening and Von Mises plasticity with associate flow rule.
2. from the overall residual stress scenario only the residual stresses along the experimentally observed crack path are extracted.
3. such residual stresses are exported to the DBEM code adopted and applied on the initial cracked configuration shown in Fig. 3a (the experimental crack growth monitoring starts with this configuration). Such stresses are modelled by line forces (a kind of body loads) along two parallel ‘‘load lines’’ that have a very low offset from the crack axis equal to 0.04 mm (the two load lines should ideally have a zero distance from the crack edges but at a distance inferior to 0.04 mm there are no appreciable differences in the results);
4. a DBEM crack propagation analysis is performed, with a load case defined as the superposition of residual stresses plus the remote fatigue load, in order to obtain the crack growth rates.

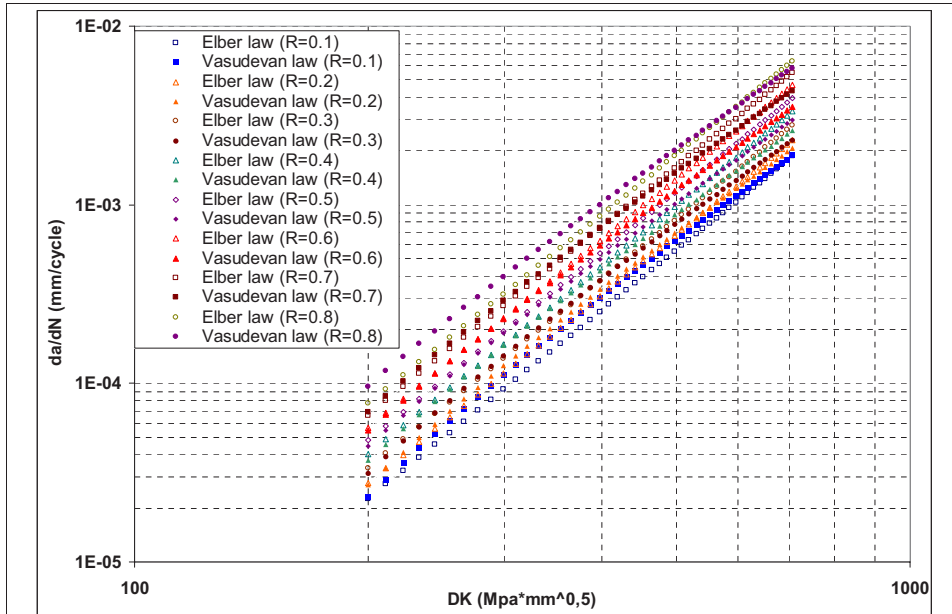


Figure 1. Experimental threshold data for 2024 HPT3, for each R-ratios (left); fitting of A, n, m Vasudevan coefficients against data from the 6056 T78 aluminium alloy (right).

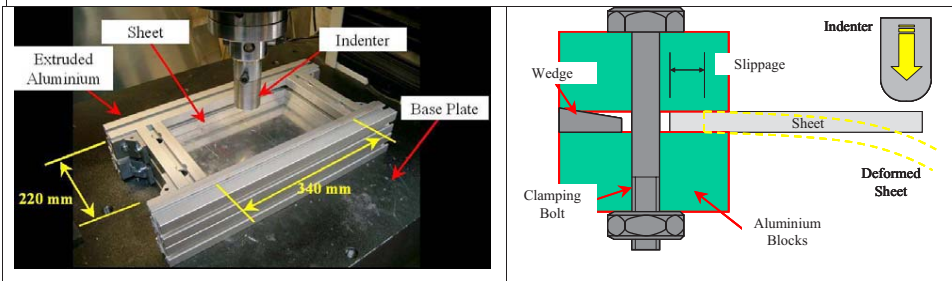


Figure 2. Coupon denting process: the indenter is pressed against the sheet with a gradually increasing load up to a predefined dent depth .

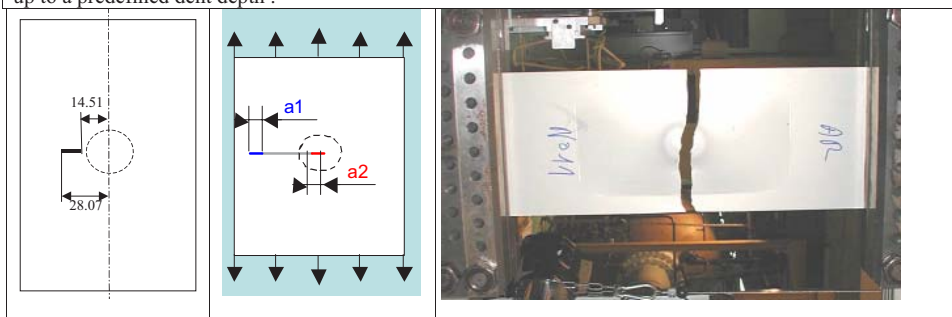


Figure 3a-b. Initial detected scenario (the propagation begins with a crack of length 13.56 mm) and dented coupon undergoing a uniaxial fatigue load.

**FEM elastic-plastic analysis.** The analysis is performed through three load steps with the following boundary conditions:

- The dent is modelled as infinitely rigid and an aluminum strip is introduced between the coupon and the constraints. The z displacement is null out of the black line, where the plate sliding occurs with zero friction (Fig. 4).
- After displacing the denting tool in contact with the plate, an initial dent displacement equal to 14 mm is imposed (Fig. 5).
- The dent displacement goes back to 0 while the other boundary conditions are retained (Fig. 6).
- All the constraints are removed but the symmetry condition and the rigid motion constraints (Fig. 7).
- Calculation of  $\sigma_Y$  residual stress at top, bottom and middle shell surface in correspondence of the plane  $y=0$  (Fig. 8).

In conclusion the residual stress field due to the plastic deformation induced by the denting process is obtained by sequentially removing the indenter and all the constraints. The final results used in the two-dimensional DBEM crack propagation analysis, are the  $\sigma_Y$  residual stress at middle shell surface (this corresponds to consider only the membrane stresses) and in correspondence of the plane  $y=0$ .

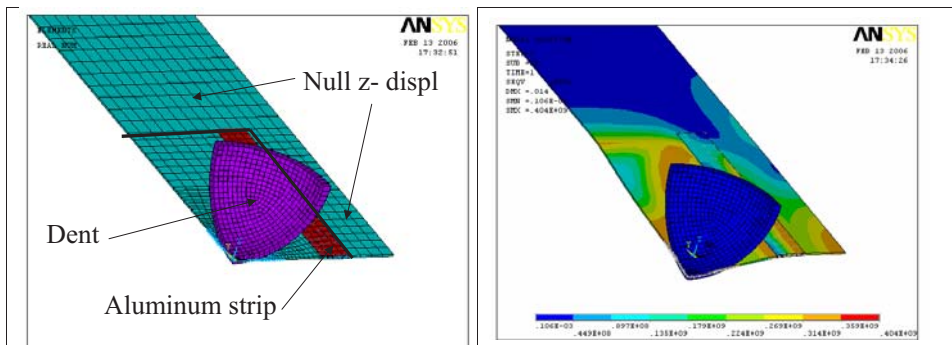


Figure 4. FEM model of skin and indenter with related boundary conditions.

Figure 5. Von Mises stresses at load step 1 (pushing up to a displacement of 14 mm) -  $\sigma_{eq,max}=404$  MPa.

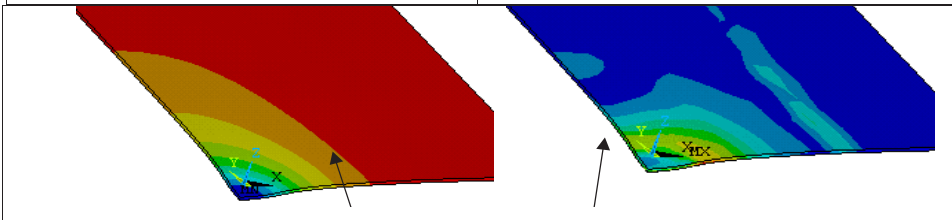


Figure 6. Load step 2 (the indenter is removed): Z displacement with maximum residual dent depth equal to 5.3 mm (left) and Von Mises stresses (right) with maximum value of  $\sigma_{eq,max} = 378$  MPa.

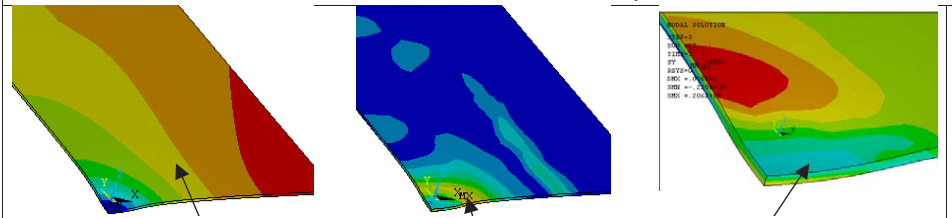


Figure 7. Load step 3 (all the constraints are removed): Z displacement (left); Von Mises stresses with  $\sigma_{eq,max}=361$  MPa (middle);  $\sigma_Y$  residual stress near the denting area with  $\sigma_{Y,max}=206$  MPa (right).

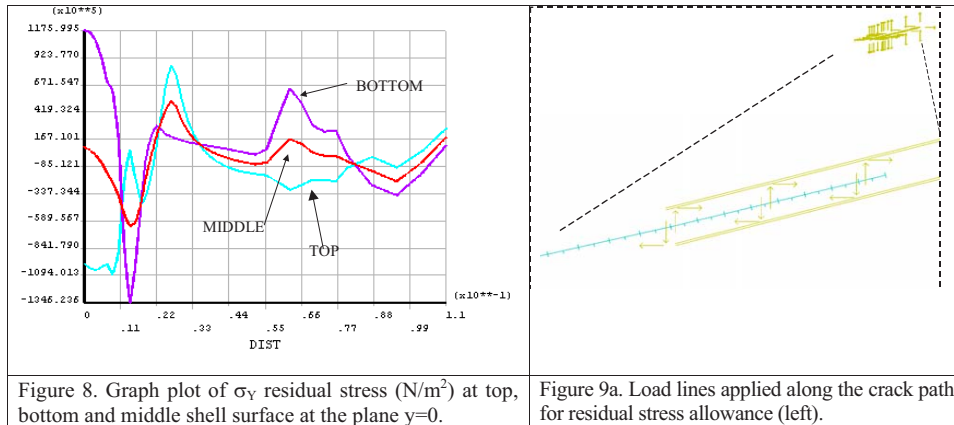
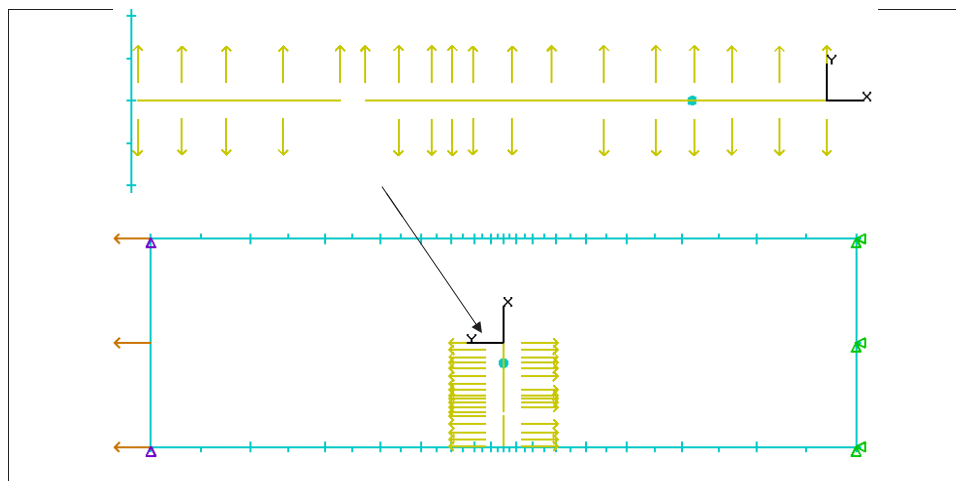


Figure 8. Graph plot of  $\sigma_y$  residual stress ( $N/m^2$ ) at top, bottom and middle shell surface at the plane  $y=0$ .

Figure 9a. Load lines applied along the crack path for residual stress allowance (left).

**DBEM crack propagation.** Having calculated the residual stresses, left by the denting process on the coupon, it is possible to start the crack propagation simulation aimed at reproducing the experimental crack propagation (Fig. 3b). The initial scenario detected in the experimental test is depicted in Fig. 3a: up to this point a maximum remote fatigue load  $t_{max}=140$  MPa with  $R=0.1$  is applied, whilst for the remaining part of the crack propagation the maximum load is set to  $t_{max}=70$  MPa with  $R=0.1$ . The residual stresses are applied as body loads along lines parallel and very close to the crack propagation path (they approximate stresses directly applied on the crack edges) and usually they are both tangential and normal (Fig. 9a) but in this case only the normal (to the crack edges) components are non negligible (Fig. 9b).

The DBEM model is shown in Fig. 9b. In Fig. 10a the Von Mises stresses and the crack deformed plot are shown at an intermediate step of crack propagation: it is possible to see that the crack opening is higher on the left hand side, where opening residual stresses are acting, whilst the opposite occurs on the right hand side, where compressive residual stresses are predominant. The numerical and experimental graphs of crack advance vs. cycles are shown in Fig. 10b for the two crack tips a1 (external) and a2 (internal), showing a satisfactory correlation. The effect of residual stresses on SIFs is shown in Fig. 11.

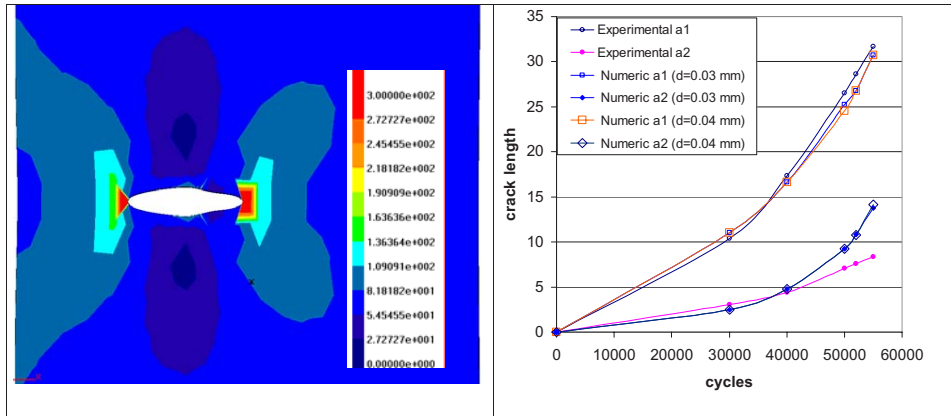


Figures 9b. DBEM coupon with residual stresses applied on crack edges and superimposed to the remote load.

**Conclusions**

The procedure described takes advantage of the best capabilities of the two numerical methods (FEM and DBEM) and can be easily automated, but most of all it does not require extensive calibration tests because

based on a physical description of the crack propagation phenomena across plastically deformed material. The differences between the calculated and experimental delay cycles are comparable with the inherent scatter but further tests are needed to obtain the precise threshold values for the 6056 T78 and to better calibrate the A, n, m values. Moreover a three-dimensional approach for both FEM and DBEM analysis could assess the importance of the bending stresses on the crack propagation, taking also into account the real stress distribution along the thickness, where a strong variation of residual stresses is evident (Fig. 8).



Figures 10a-b. DBEM contour plot of stress results at the final stage of the propagation phase: the residual stress effect causes an unsymmetric crack opening (left); numerical and experimental crack growth (right).

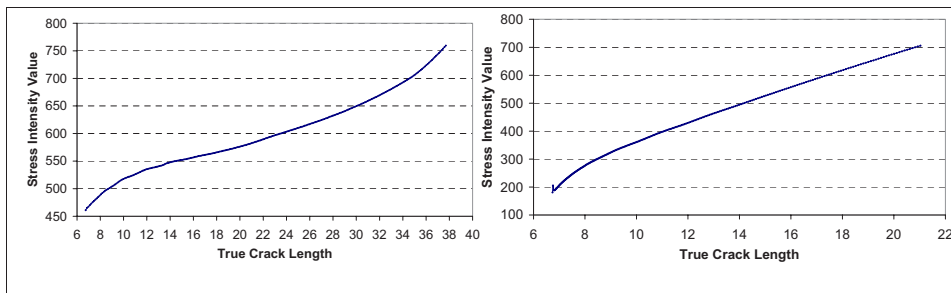


Figure 11. SIFs (MPa\*mm<sup>1/2</sup>) vs. crack length (mm) for crack tip 1 and 2.

#### Literature references

1. K. Sadananda, A.K. Vasudevan, Short crack growth and internal stresses, *Int. J. Fatigue International Journal of Fatigue* 19, (1997), Supp. No. 1, pp. S99–S108.
2. K. Sadananda, A.K. Vasudevan, R.L. Holtz, E.U. Lee, Analysis of overload effects and related phenomena, *Int. J. Fatigue* Vol. 21, pp. S233–S246, 1999.
3. R. Citarella, G. Cricri, A two-parameter model for crack growth simulation under variable load spectrum by combined FEM-DBEM approach, *International Conference on Boundary Element Techniques*, 24-26th July 2007, Naples, Italy.
4. C. Cali, R. Citarella, M. Lepore, M. Perrella, Integrated system for monitoring the initiation and propagation of fatigue cracks, *Conference proceedings "Advances in fracture and damage mechanics IV"*, 12-14 July 2005, Mallorca, Spain.
5. C. Cali, R. Citarella, G. Cricri, A two-parameter model for crack growth simulation under variable spectrum load by combined fem/analytical approach, *The 6th International Conference on Intelligent Processing and Manufacturing of Materials*, June, 25-29 2007.
6. BEASY, BEASY V10r7 Documentation, C.M BEASY Ltd, 2007.

## Boundary element based computation of induced electric fields in the quasistatic regime

L. Marin<sup>1,\*</sup>, C. Cobos Sanchez<sup>2</sup>, P. Glover<sup>2</sup>, H. Power<sup>1</sup>,  
R.W. Bowtell<sup>2</sup>, A.A. Becker<sup>1</sup> and I.A. Jones<sup>1</sup>

<sup>1</sup>School of Mechanical, Materials and Manufacturing Engineering,  
The University of Nottingham, University Park, Nottingham NG7 2RD, UK,

\*liviu.marin@nottingham.ac.uk

<sup>2</sup>Sir Peter Mansfield Magnetic Resonance Centre, School of Physics and Astronomy,  
The University of Nottingham, Nottingham Park, Nottingham NG7 2RD, UK

**Keywords:** Direct problem; Electromagnetism; Quasistatic regime; Magnetic resonance imaging (MRI).

**Abstract.** We formulate the mathematical problem corresponding to an object subject to time varying magnetic field gradients or movement in or around an MRI scanner, in the framework of quasistatic electromagnetism. Based on the integral formulation of the problem, the induced currents in several single and multi-domains exposed to switched gradients are calculated using the BEM.

### Introduction

Magnetic resonance imaging (MRI) relies on the use of both high static magnetic fields and rapidly switched magnetic field gradients. Natural movement in the large static field can cause induced currents in conducting tissues and have potential bio-effects, such as dizziness and metallic taste on the tongue, whilst the switching of gradients may produce peripheral nerve stimulation (PNS) in subjects. Since it is not feasible to measure the induced current or electric field in an object directly, various numerical techniques, such as the finite-difference time domain method (FDTD) [1] or impedance method [2], are usually employed to calculate the induced electric field for complex geometries.

The boundary element method (BEM) has already been applied for computing the electromagnetic field in the case of both magneto-encephalography (MEG) [3] and electro-encephalography (EEG) [4], and has been shown to provide excellent results for low frequency studies. Therefore, in this paper we propose a BEM-based calculation of induced currents in the human body caused by exposure to time varying magnetic field gradients or movement in or around an MRI scanner. The efficiency of the proposed BEM approach is illustrated by considering simply shaped objects exposed to switched gradients, for which analytical solutions are available [5], as well as a head model in the bore of a 7T magnet.

### Mathematical Formulation

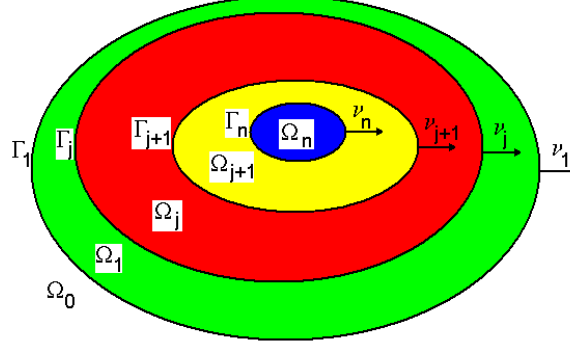
Consider a non-magnetic material occupying the domain  $\Omega = \bigcup_{j=1}^n \Omega_j \subset \mathbb{R}^3$  such that  $\Gamma_j = \partial\Omega_j \cap \partial\Omega_{j-1}$ ,

$j = 1, \dots, n$ , where  $\Omega_0 = \mathbb{R}^3 \setminus \bar{\Omega}$  is the free-space and  $n \geq 1$ , see Fig. 1, and assume that every subdomain  $\Omega_j$ ,  $j = 0, 1, \dots, n$ , is homogeneous and characterised by the electrical permittivity,  $\epsilon_j = \epsilon_0 \epsilon_j^r$ , permeability,  $\mu_j = \mu_0 \mu_j^r$  and conductivity,  $\sigma_j$ . Here  $\epsilon_j^r$  and  $\mu_j^r$ ,  $j = 0, 1, \dots, n$ , are the relative permittivity and permeability of  $\Omega_j$ , respectively, where  $\epsilon_0 = c^{-2} \mu_0^{-1}$  F/m is the permittivity of the free-space,  $c \approx 3.0 \times 10^8$  m/s the speed of light and  $\mu_0 = 4\pi \times 10^{-7}$  H/m the permeability of the free-space.

**Maxwell Equations.** The electric field,  $\mathbf{E}_j(\mathbf{x}, t)$ , electric displacement,  $\mathbf{D}_j(\mathbf{x}, t) = \epsilon_j \mathbf{E}_j(\mathbf{x}, t)$ , magnetic field,  $\mathbf{H}_j(\mathbf{x}, t)$ , and magnetic induction,  $\mathbf{B}_j(\mathbf{x}, t) = \mu_j \mathbf{H}_j(\mathbf{x}, t)$ , satisfy Maxwell's equations [6]:

$$\left\{ \begin{array}{ll} \nabla \cdot \mathbf{D}_j(\mathbf{x}, t) = \rho_j(\mathbf{x}, t) & \text{(Coulomb's law)} \\ \nabla \cdot \mathbf{B}_j(\mathbf{x}, t) = 0 & \text{(Absence of free magnetic poles)} \\ \nabla \times \mathbf{E}_j(\mathbf{x}, t) = -\frac{\partial \mathbf{B}_j(\mathbf{x}, t)}{\partial t} & \text{(Faraday's law)} \\ \nabla \times \mathbf{H}_j(\mathbf{x}, t) = \mathbf{J}(\mathbf{x}, t) + \mathbf{J}_j^c(\mathbf{x}, t) + \frac{\partial \mathbf{D}_j(\mathbf{x}, t)}{\partial t} & \text{(Ampère's law)} \end{array} \right. \quad (1)$$

for  $\mathbf{x} \in \Omega_j$ ,  $j = 0, 1, \dots, n$ , and  $t \in [0, \infty)$ . Here  $\rho_j(\mathbf{x}, t)$  is the charge density,  $\mathbf{J}_j^c(\mathbf{x}, t) = \sigma_j \mathbf{E}_j(\mathbf{x}, t)$  is

Figure 1: Schematic diagram of the domain  $\Omega \subset \mathbb{R}^3$ .

the conduction current,  $\mathbf{J}_j^d(\mathbf{x}, t) = \frac{\partial \mathbf{D}_j(\mathbf{x}, t)}{\partial t} = \epsilon_j \frac{\partial \mathbf{E}_j(\mathbf{x}, t)}{\partial t}$  is the displacement current and  $\mathbf{J}(\mathbf{x}, t)$  is the current density in the coil.

In order to close the system of partial differential equations (1), the charge density,  $\rho(\mathbf{x}, t) = \rho_j(\mathbf{x}, t) \chi_{\Omega_j}(\mathbf{x})$ , conduction current,  $\mathbf{J}^c(\mathbf{x}, t) = \mathbf{J}_j^c(\mathbf{x}, t) \chi_{\Omega_j}(\mathbf{x})$ , where  $\chi_{\Omega_j}(\mathbf{x}) = 1$  if  $\mathbf{x} \in \Omega_j$  and  $\chi_{\Omega_j}(\mathbf{x}) = 0$  if  $\mathbf{x} \notin \Omega_j$ , and the current density in the coil,  $\mathbf{J}(\mathbf{x}, t)$ , are required to satisfy the continuity equation [6], namely

$$\nabla \cdot [\mathbf{J}(\mathbf{x}, t) + \mathbf{J}^c(\mathbf{x}, t)] + \frac{\partial \rho(\mathbf{x}, t)}{\partial t} = 0, \quad \mathbf{x} \in \mathbb{R}^3, \quad t \in [0, \infty). \quad (2)$$

The current density in the coil,  $\mathbf{J}(\mathbf{x}, t)$ , is defined as a surface current density,  $\mathbf{J}^{\text{coil}}(\mathbf{x}, t)$ , i.e.

$$\mathbf{J}(\mathbf{x}, t) = \mathbf{J}^{\text{coil}}(\mathbf{x}, t) \chi_{\Gamma_{\text{coil}}}(\mathbf{x}), \quad \mathbf{x} \in \mathbb{R}^3, \quad t \in [0, \infty), \quad (3)$$

where  $\Gamma_{\text{coil}} \subset \mathbb{R}^3$  is the coil surface and  $\delta(\mathbf{x}', \mathbf{x})$  is the Kronecker delta function, such that

$$\nabla \cdot \mathbf{J}^{\text{coil}}(\mathbf{x}, t) = 0, \quad \mathbf{J}^{\text{coil}}(\mathbf{x}, t) \cdot \boldsymbol{\nu}^{\text{coil}}(\mathbf{x}) = 0, \quad \mathbf{x} \in \Gamma_{\text{coil}}, \quad t \in [0, \infty). \quad (4)$$

with  $\boldsymbol{\nu}^{\text{coil}}(\mathbf{x})$  the outward unit vector normal to the coil surface  $\Gamma_{\text{coil}}$ . Hence on employing equations (3) and (4), the continuity equation (2) may be recast as

$$\nabla \cdot \mathbf{J}^c(\mathbf{x}, t) + \frac{\partial \rho(\mathbf{x}, t)}{\partial t} = 0, \quad \mathbf{x} \in \mathbb{R}^3, \quad t \in [0, \infty). \quad (5)$$

**Scalar and Vector Potentials.** The magnetic induction,  $\mathbf{B}_j(\mathbf{x}, t)$ , can be expressed using the vector potential  $\mathbf{A}_j(\mathbf{x}, t)$  as:

$$\mathbf{B}_j(\mathbf{x}, t) = \nabla \times \mathbf{A}_j(\mathbf{x}, t), \quad \mathbf{x} \in \Omega_j, \quad t \in [0, \infty). \quad (6)$$

Note that by introducing the vector potential,  $\mathbf{A}_j(\mathbf{x}, t)$ , the equation describing the absence of free magnetic poles (1<sub>2</sub>) is automatically satisfied since  $\nabla \cdot (\nabla \times \mathbf{A}_j) = 0$ . On using equation (6) and the Coulomb gauge [6]

$$\nabla \cdot \mathbf{A}_j(\mathbf{x}, t) = 0, \quad \mathbf{x} \in \Omega_j, \quad t \in [0, \infty), \quad (7)$$

the Ampère's law (1<sub>4</sub>) in every subdomain  $\Omega_j$ ,  $j = 0, 1, \dots, n$ , reduces to the following equation for the vector potential

$$-\frac{1}{\mu_j} \nabla^2 \mathbf{A}_j(\mathbf{x}, t) = \mathbf{J}(\mathbf{x}, t) + \sigma_j \mathbf{E}_j(\mathbf{x}, t) + \epsilon_j \frac{\partial \mathbf{E}_j(\mathbf{x}, t)}{\partial t}, \quad \mathbf{x} \in \Omega_j, \quad t \in [0, \infty). \quad (8)$$

The electric field,  $\mathbf{E}_j(\mathbf{x}, t)$ , can be expressed using a scalar potential,  $\phi_j(\mathbf{x}, t)$ , and the vector potential,  $\mathbf{A}_j(\mathbf{x}, t)$ , introduced in equation (6). To do so, we apply the curl operator to Faraday's law (13) and obtain  $\nabla \times \left( \mathbf{E}_j(\mathbf{x}, t) + \frac{\partial \mathbf{A}_j(\mathbf{x}, t)}{\partial t} \right) = 0$ . Consequently, there exists a scalar potential,  $\phi_j(\mathbf{x}, t)$ , such that

$$\mathbf{E}_j(\mathbf{x}, t) = -\nabla \phi_j(\mathbf{x}, t) - \frac{\partial \mathbf{A}_j(\mathbf{x}, t)}{\partial t}, \quad \mathbf{x} \in \Omega_j, \quad t \in [0, \infty). \quad (9)$$

If we apply the divergence operator to equation (9) multiplied by  $\sigma_j$  and use the Coulomb gauge (7) then we obtain the following equation for the conduction current,  $\mathbf{J}_j^c(\mathbf{x}, t) = \sigma_j \mathbf{E}_j(\mathbf{x}, t)$ , in every subdomain  $\Omega_j$ ,  $j = 0, 1, \dots, n$ ,

$$\nabla \cdot \left( [\sigma_j \mathbf{E}_j(\mathbf{x}, t)] + \frac{\epsilon_j}{\sigma_j} \frac{\partial}{\partial t} [\sigma_j \mathbf{E}_j(\mathbf{x}, t)] \right) = 0, \quad \mathbf{x} \in \Omega_j, \quad t \in [0, \infty). \quad (10)$$

Finally, on applying the divergence operator to Ampère's law (14) and making use of Coulomb's law (11) and the divergence-free property of the current density in the coil (41), we obtain the equation that must be satisfied by the scalar potential,  $\phi_j(\mathbf{x}, t)$ , in every subdomain  $\Omega_j$ ,  $j = 0, 1, \dots, n$ , namely

$$\sigma_j \nabla^2 \phi_j(\mathbf{x}, t) + \nabla \cdot [\sigma_j \mathbf{E}_j(\mathbf{x}, t)] = 0, \quad \mathbf{x} \in \Omega_j, \quad t \in [0, \infty). \quad (11)$$

**Boundary Conditions.** If we impose the conservation of the induced current,  $\mathbf{J}_j^c(\mathbf{x}, t) = \sigma_j \mathbf{E}_j(\mathbf{x}, t)$ , flowing through the surface  $\Gamma_j$ ,  $j = 1, 2, \dots, n$ , that defines the interface of two different media  $\Omega_j$  and  $\Omega_{j-1}$ , we obtain the following boundary conditions

$$\left[ \mathbf{J}_j^c(\mathbf{x}, t) + \frac{\epsilon_j}{\sigma_j} \frac{\partial \mathbf{J}_j^c(\mathbf{x}, t)}{\partial t} \right] \cdot \boldsymbol{\nu}_j^-(\mathbf{x}) + \left[ \mathbf{J}_{j-1}^c(\mathbf{x}, t) + \frac{\epsilon_{j-1}}{\sigma_{j-1}} \frac{\partial \mathbf{J}_{j-1}^c(\mathbf{x}, t)}{\partial t} \right] \cdot \boldsymbol{\nu}_{j-1}^-(\mathbf{x}) = 0, \quad \mathbf{x} \in \Gamma_j, \quad t \in [0, \infty). \quad (12)$$

where  $\boldsymbol{\nu}_j^-(\mathbf{x})$  and  $\boldsymbol{\nu}_{j-1}^-(\mathbf{x})$  are the outward unit normal vectors at  $\mathbf{x} \in \partial\Omega_j$  and  $\mathbf{x} \in \partial\Omega_{j-1}$ , respectively. Since  $\boldsymbol{\nu}_j(\mathbf{x}) = \boldsymbol{\nu}_j^-(\mathbf{x}) = -\boldsymbol{\nu}_{j-1}^-(\mathbf{x})$  for  $\mathbf{x} \in \Gamma_j$ , see also Fig. 1, the boundary conditions (12) on the surface  $\Gamma_j$ ,  $j = 1, 2, \dots, n$ , may be recast as

$$\left[ \sigma_j \mathbf{E}_j(\mathbf{x}, t) + \epsilon_j \frac{\partial \mathbf{E}_j(\mathbf{x}, t)}{\partial t} - \sigma_{j-1} \mathbf{E}_{j-1}(\mathbf{x}, t) - \epsilon_{j-1} \frac{\partial \mathbf{E}_{j-1}(\mathbf{x}, t)}{\partial t} \right] \cdot \boldsymbol{\nu}_j(\mathbf{x}) = 0, \quad \mathbf{x} \in \Gamma_j, \quad t \in [0, \infty). \quad (13)$$

On taking into account the continuity of the vector potential and its normal derivative on the surface  $\Gamma_j$ ,  $j = 1, 2, \dots, n$ , from equations (9) and (13) we obtain the following boundary conditions in terms of the normal component of the vector potential and the normal derivative of the scalar potential, i.e.

$$\begin{aligned} & \left[ \sigma_j \nabla \phi_j(\mathbf{x}, t) + \epsilon_j \frac{\partial}{\partial t} \nabla \phi_j(\mathbf{x}, t) - \sigma_{j-1} \nabla \phi_{j-1}(\mathbf{x}, t) - \epsilon_{j-1} \frac{\partial}{\partial t} \nabla \phi_{j-1}(\mathbf{x}, t) \right] \cdot \boldsymbol{\nu}_j(\mathbf{x}) = \\ & - \left[ \sigma_j \frac{\partial A_j^\nu(\mathbf{x}, t)}{\partial t} + \epsilon_j \frac{\partial^2 A_j^\nu(\mathbf{x}, t)}{\partial t^2} \right] + \left[ \sigma_{j-1} \frac{\partial A_{j-1}^\nu(\mathbf{x}, t)}{\partial t} + \epsilon_{j-1} \frac{\partial^2 A_{j-1}^\nu(\mathbf{x}, t)}{\partial t^2} \right], \quad \mathbf{x} \in \Gamma_j, \quad t \in [0, \infty). \end{aligned} \quad (14)$$

where  $A_j^\nu(\mathbf{x}, t) = \mathbf{A}_j(\mathbf{x}, t) \cdot \boldsymbol{\nu}_j(\mathbf{x})$  for  $\mathbf{x} \in \Gamma_j$  and  $t \in [0, \infty)$ .

**Frequency Space.** Assume that the time variations in Maxwell equations are not too rapid, i.e. we consider the quasistatic case, and all the time-dependent quantities involved in equations (1)–(6) vary with time at the angular frequency,  $\omega$ , such that e.g.  $\mathbf{E}_j(\mathbf{x}, t) = \widehat{\mathbf{E}}_j(\mathbf{x}) e^{-i\omega t}$  with  $i = \sqrt{-1}$ . In the frequency space, equations (8), (10) and (11) read as follows

$$-\frac{1}{\mu_j} \nabla^2 \widehat{\mathbf{A}}_j(\mathbf{x}) = \widehat{\mathbf{J}}(\mathbf{x}) + \left( 1 - \frac{i\omega\epsilon_j}{\sigma_j} \right) \sigma_j \widehat{\mathbf{E}}_j(\mathbf{x}), \quad \mathbf{x} \in \Omega_j, \quad (15)$$

$$\nabla \cdot \left[ \left( 1 - \frac{i\omega\epsilon_j}{\sigma_j} \right) \sigma_j \widehat{\mathbf{E}}_j(\mathbf{x}) \right] = 0, \quad \mathbf{x} \in \Omega_j, \quad (16)$$

and

$$-\sigma_j \nabla^2 \widehat{\phi}_j(\mathbf{x}) = \nabla \cdot \left[ \sigma_j \widehat{\mathbf{E}}_j(\mathbf{x}) \right], \quad \mathbf{x} \in \Omega_j, \quad (17)$$

respectively.

It should be mentioned that in the case of biological tissues the conductivities,  $\sigma_j$ ,  $j = 1, \dots, n$ , and permittivities,  $\epsilon_j$ ,  $j = 1, \dots, n$ , are  $\mathcal{O}(1)$  and  $\mathcal{O}(10^{-6})$ , respectively, the angular frequency,  $\omega$ , in the quasistatic regime is  $\mathcal{O}(10^4)$ , whilst the module of the current density in the coil,  $|\widehat{\mathbf{J}}(\mathbf{x})|$ , is  $\mathcal{O}(10^7)$ . Consequently, the effect of the induced current,  $\widehat{\mathbf{J}}_j^c(\mathbf{x}) = \sigma_j \widehat{\mathbf{E}}_j(\mathbf{x})$ , and displacement current,  $\widehat{\mathbf{J}}_j^d(\mathbf{x}) = -\frac{i\omega\epsilon_j}{\sigma_j} \left[ \sigma_j \widehat{\mathbf{E}}_j(\mathbf{x}) \right]$ , on the vector potential,  $\widehat{\mathbf{A}}_j(\mathbf{x})$ , can be neglected since  $|\sigma_j \widehat{\mathbf{E}}_j(\mathbf{x})| \ll |\widehat{\mathbf{J}}(\mathbf{x})|$  and  $\left| \frac{i\omega\epsilon_j}{\sigma_j} \right| \ll 1$ , respectively.

Therefore, in the frequency space equations (15) – (17) reduce to

$$-\frac{1}{\mu_j} \nabla^2 \widehat{\mathbf{A}}_j(\mathbf{x}) = \widehat{\mathbf{J}}(\mathbf{x}), \quad \nabla \cdot \left[ \sigma_j \widehat{\mathbf{E}}_j(\mathbf{x}) \right] = 0, \quad -\sigma_j \nabla^2 \widehat{\phi}_j(\mathbf{x}) = 0, \quad \mathbf{x} \in \Omega_j, \quad (18)$$

respectively, whilst equation (9) recasts as

$$\widehat{\mathbf{E}}_j(\mathbf{x}) = -\nabla \widehat{\phi}_j(\mathbf{x}) + i\omega \widehat{\mathbf{A}}_j(\mathbf{x}), \quad \mathbf{x} \in \mathbb{R}^3. \quad (19)$$

The boundary conditions given by equations (13) and (14) read as

$$\left[ \left( 1 - \frac{i\omega\epsilon_j}{\sigma_j} \right) \sigma_j \widehat{\mathbf{E}}_j(\mathbf{x}) - \left( 1 - \frac{i\omega\epsilon_{j-1}}{\sigma_{j-1}} \right) \sigma_{j-1} \widehat{\mathbf{E}}_{j-1}(\mathbf{x}) \right] \cdot \boldsymbol{\nu}_j(\mathbf{x}) = 0, \quad \mathbf{x} \in \Gamma_j, \quad (20)$$

and

$$\begin{aligned} & \left[ \left( 1 - \frac{i\omega\epsilon_j}{\sigma_j} \right) \sigma_j \nabla \widehat{\phi}_j(\mathbf{x}) - \left( 1 - \frac{i\omega\epsilon_{j-1}}{\sigma_{j-1}} \right) \sigma_{j-1} \nabla \widehat{\phi}_{j-1}(\mathbf{x}) \right] \cdot \boldsymbol{\nu}_j(\mathbf{x}) = \\ & = i\omega \left[ \left( 1 - \frac{i\omega\epsilon_j}{\sigma_j} \right) \sigma_j - \left( 1 - \frac{i\omega\epsilon_{j-1}}{\sigma_{j-1}} \right) \sigma_{j-1} \right] \widehat{\mathbf{A}}_j^{\nu}(\mathbf{x}), \quad \mathbf{x} \in \Gamma_j, \end{aligned} \quad (21)$$

respectively, where  $\widehat{\mathbf{A}}_j^{\nu}(\mathbf{x}) = \widehat{\mathbf{A}}_j(\mathbf{x}) \cdot \boldsymbol{\nu}_j(\mathbf{x})$  for  $\mathbf{x} \in \Gamma_j$ . On using the quasistatic approximations, the boundary conditions (20) and (21) in the frequency space reduce to

$$\left[ \sigma_j \widehat{\mathbf{E}}_j(\mathbf{x}) - \sigma_{j-1} \widehat{\mathbf{E}}_{j-1}(\mathbf{x}) \right] \cdot \boldsymbol{\nu}_j(\mathbf{x}) = 0, \quad \mathbf{x} \in \Gamma_j, \quad (22)$$

and

$$\left[ \sigma_j \nabla \widehat{\phi}_j(\mathbf{x}) - \sigma_{j-1} \nabla \widehat{\phi}_{j-1}(\mathbf{x}) \right] \cdot \boldsymbol{\nu}_j(\mathbf{x}) = i\omega (\sigma_j - \sigma_{j-1}) \widehat{\mathbf{A}}_j^{\nu}(\mathbf{x}), \quad \mathbf{x} \in \Gamma_j, \quad (23)$$

respectively.

### Boundary Integral Equations

In this section, we present the integral equations for the vector and scalar potentials, as well as the electric field, by employing the fundamental solution of the three-dimensional Laplace equation,  $u^*(\mathbf{x}, \mathbf{y}) = 1/(4\pi|\mathbf{x} - \mathbf{y}|)$ ,  $\mathbf{x}, \mathbf{y} \in \mathbb{R}^3$ , and its normal derivative, see e.g. [7, 8].

**Vector Potential.** Since the surface current density,  $\widehat{\mathbf{J}}^{\text{coil}}(\mathbf{x})$ , is known on the coil surface  $\mathbf{x} \in \Gamma_{\text{coil}}$ , the vector potential  $\widehat{\mathbf{A}}_j(\mathbf{x})$  for  $\mathbf{x} \in \Omega_j$ , is determined from the Poisson equation (18<sub>1</sub>) and its integral representation [8]. More precisely, we obtain

$$\widehat{\mathbf{A}}_j(\mathbf{x}) = \mu_j \int_{\mathbb{R}^3} u^*(\mathbf{x}, \mathbf{y}) \widehat{\mathbf{J}}(\mathbf{y}) \, d\mathbf{y} = \mu_j \int_{\Gamma_{\text{coil}}} u^*(\mathbf{x}, \mathbf{y}) \widehat{\mathbf{J}}^{\text{coil}}(\mathbf{y}) \, d\Gamma(\mathbf{y}), \quad \mathbf{x} \in \overline{\Omega}_j. \quad (24)$$

**Scalar Potential.** The following integral representation for the scalar potential,  $\widehat{\phi}_j(\mathbf{x})$ ,  $j = 0, 1, \dots, n$ , holds:

$$\begin{aligned} c_j(\mathbf{x}) \sigma_j \widehat{\phi}_j(\mathbf{x}) &= \int_{\partial\Omega_j} \sigma_j \left[ u^*(\mathbf{x}, \mathbf{y}) \left( \nabla \widehat{\phi}_j(\mathbf{y}) \cdot \boldsymbol{\nu}^-(\mathbf{y}) \right) - (\nabla_{\mathbf{y}} u^*(\mathbf{x}, \mathbf{y}) \cdot \boldsymbol{\nu}^-(\mathbf{y})) \widehat{\phi}_j(\mathbf{y}) \right] d\Gamma(\mathbf{y}) \\ &= \int_{\Gamma_j} \sigma_j \left[ u^*(\mathbf{x}, \mathbf{y}) \left( \nabla \widehat{\phi}_j(\mathbf{y}) \cdot \boldsymbol{\nu}_j(\mathbf{y}) \right) - (\nabla_{\mathbf{y}} u^*(\mathbf{x}, \mathbf{y}) \cdot \boldsymbol{\nu}_j(\mathbf{y})) \widehat{\phi}_j(\mathbf{y}) \right] d\Gamma(\mathbf{y}) \\ &\quad - \int_{\Gamma_{j+1}} \sigma_j \left[ u^*(\mathbf{x}, \mathbf{y}) \left( \nabla \widehat{\phi}_j(\mathbf{y}) \cdot \boldsymbol{\nu}_{j+1}(\mathbf{y}) \right) - (\nabla_{\mathbf{y}} u^*(\mathbf{x}, \mathbf{y}) \cdot \boldsymbol{\nu}_{j+1}(\mathbf{y})) \widehat{\phi}_j(\mathbf{y}) \right] d\Gamma(\mathbf{y}) \end{aligned} \quad (25)$$

for  $\mathbf{x} \in \mathbb{R}^3$  and  $t \in [0, \infty)$ , where the identities  $\boldsymbol{\nu}^-(\mathbf{y})|_{\Gamma_j} = \boldsymbol{\nu}_j(\mathbf{y})|_{\Gamma_j}$  and  $\boldsymbol{\nu}^-(\mathbf{y})|_{\Gamma_{j+1}} = -\boldsymbol{\nu}_{j+1}(\mathbf{y})|_{\Gamma_{j+1}}$  have been used, and  $c_j(\mathbf{x})$ ,  $j = 0, 1, \dots, n$ , is given by

$$c_j(\mathbf{x}) = \begin{cases} \delta_{jk}, & \mathbf{x} \in \Omega_k \\ \frac{1}{2} \delta_{jk}, & \mathbf{x} \in (\overline{\Omega}_k \cap \Gamma_k) \cup (\overline{\Omega}_k \cap \Gamma_{k+1}) \\ -\frac{1}{2} \delta_{jk}, & \mathbf{x} \in (\overline{\Omega}_{k-1} \cap \Gamma_k) \cup (\overline{\Omega}_{k+1} \cap \Gamma_{k+1}). \end{cases} \quad (26)$$

It should be mentioned that equation (25) reduces to

$$c_0(\mathbf{x}) \sigma_0 \widehat{\phi}_0(\mathbf{x}) = - \int_{\Gamma_1} \sigma_0 \left[ u^*(\mathbf{x}, \mathbf{y}) \left( \nabla \widehat{\phi}_0(\mathbf{y}) \cdot \boldsymbol{\nu}_1(\mathbf{y}) \right) - (\nabla_{\mathbf{y}} u^*(\mathbf{x}, \mathbf{y}) \cdot \boldsymbol{\nu}_1(\mathbf{y})) \widehat{\phi}_0(\mathbf{y}) \right] d\Gamma(\mathbf{y}) \quad (27)$$

and

$$c_n(\mathbf{x}) \sigma_n \widehat{\phi}_n(\mathbf{x}) = \int_{\Gamma_n} \sigma_n \left[ u^*(\mathbf{x}, \mathbf{y}) \left( \nabla \widehat{\phi}_n(\mathbf{y}) \cdot \boldsymbol{\nu}_n(\mathbf{y}) \right) - (\nabla_{\mathbf{y}} u^*(\mathbf{x}, \mathbf{y}) \cdot \boldsymbol{\nu}_n(\mathbf{y})) \widehat{\phi}_n(\mathbf{y}) \right] d\Gamma(\mathbf{y}) \quad (28)$$

for  $j = 0$  and  $j = n$ , respectively. On summing up equation (25) for  $j = 0, 1, \dots, n$ , we obtain

$$\begin{aligned} &\sum_{j=0}^n c_j(\mathbf{x}) \sigma_j \widehat{\phi}_j(\mathbf{x}) = \\ &= \sum_{j=1}^n \int_{\Gamma_j} \sigma_j \left[ u^*(\mathbf{x}, \mathbf{y}) \left( \nabla \widehat{\phi}_j(\mathbf{y}) \cdot \boldsymbol{\nu}_j(\mathbf{y}) \right) - (\nabla_{\mathbf{y}} u^*(\mathbf{x}, \mathbf{y}) \cdot \boldsymbol{\nu}_j(\mathbf{y})) \widehat{\phi}_j(\mathbf{y}) \right] d\Gamma(\mathbf{y}) \\ &\quad - \sum_{j=1}^n \int_{\Gamma_j} \sigma_{j-1} \left[ u^*(\mathbf{x}, \mathbf{y}) \left( \nabla \widehat{\phi}_{j-1}(\mathbf{y}) \cdot \boldsymbol{\nu}_j(\mathbf{y}) \right) - (\nabla_{\mathbf{y}} u^*(\mathbf{x}, \mathbf{y}) \cdot \boldsymbol{\nu}_j(\mathbf{y})) \widehat{\phi}_{j-1}(\mathbf{y}) \right] d\Gamma(\mathbf{y}). \end{aligned} \quad (29)$$

In the case of domain points  $\mathbf{x} \in \Omega_k$ ,  $k = 0, 1, \dots, n$ , equation (29) yields

$$\begin{aligned} \sum_{j=0}^n \delta_{jk} \sigma_j \widehat{\phi}_j(\mathbf{x}) &= \sum_{j=1}^n \int_{\Gamma_j} u^*(\mathbf{x}, \mathbf{y}) \left[ \underbrace{(\sigma_j \nabla \widehat{\phi}_j(\mathbf{y}) - \sigma_{j-1} \nabla \widehat{\phi}_{j-1}(\mathbf{y})) \cdot \boldsymbol{\nu}_j(\mathbf{y})}_{= i\omega (\sigma_j - \sigma_{j-1}) \widehat{\mathbf{A}}_j^{\nu}(\mathbf{y})} \right] d\Gamma(\mathbf{y}) \\ &\quad - \sum_{j=1}^n \int_{\Gamma_j} (\nabla_{\mathbf{y}} u^*(\mathbf{x}, \mathbf{y}) \cdot \boldsymbol{\nu}_j(\mathbf{y})) \underbrace{(\sigma_j \widehat{\phi}_j(\mathbf{y}) - \sigma_{j-1} \widehat{\phi}_{j-1}(\mathbf{y}))}_{= (\sigma_j - \sigma_{j-1}) \widehat{\phi}_j(\mathbf{y})} d\Gamma(\mathbf{y}) \end{aligned} \quad (30)$$

and by employing the boundary conditions (23) and the continuity of the scalar potential on the boundary  $\Gamma_j$ , i.e.  $\widehat{\phi}_j(\mathbf{y})|_{\Gamma_j} = \widehat{\phi}_{j-1}(\mathbf{y})|_{\Gamma_j}$ , we obtain the integral representation for domain points  $\mathbf{x} \in \Omega_k$ ,  $k = 0, 1, \dots, n$ , as

$$\widehat{\phi}_k(\mathbf{x}) = \sum_{j=1}^n \frac{\sigma_j - \sigma_{j-1}}{\sigma_k} \left( i\omega \int_{\Gamma_j} u^*(\mathbf{x}, \mathbf{y}) \widehat{\mathbf{A}}_j^{\nu}(\mathbf{y}) d\Gamma(\mathbf{y}) - \int_{\Gamma_j} (\nabla_{\mathbf{y}} u^*(\mathbf{x}, \mathbf{y}) \cdot \boldsymbol{\nu}_j(\mathbf{y})) \widehat{\phi}_j(\mathbf{y}) d\Gamma(\mathbf{y}) \right). \quad (31)$$

In a similar manner, from equation (29) we obtain the integral representation for boundary points  $\mathbf{x} \in \Gamma_k = \overline{\Omega}_{k-1} \cap \overline{\Omega}_k$ ,  $k = 1, 2, \dots, n$ , namely

$$\widehat{\phi}_k(\mathbf{x}) = 2 \sum_{j=1}^n \frac{\sigma_j - \sigma_{j-1}}{\sigma_k + \sigma_{k+1}} \left( i\omega \int_{\Gamma_j} u^*(\mathbf{x}, \mathbf{y}) \widehat{A}_j^\nu(\mathbf{y}) d\Gamma(\mathbf{y}) - \int_{\Gamma_j} (\nabla_{\mathbf{y}} u^*(\mathbf{x}, \mathbf{y}) \cdot \boldsymbol{\nu}_j(\mathbf{y})) \widehat{\phi}_j(\mathbf{y}) d\Gamma(\mathbf{y}) \right). \quad (32)$$

**Electric Field.** The integral representations for domain points  $\mathbf{x} \in \Omega_k$ ,  $k = 0, 1, \dots, n$ ,

$$\begin{aligned} \widehat{\mathbf{E}}_k(\mathbf{x}) &= i\omega\mu_k \int_{\Gamma_{\text{coil}}} u^*(\mathbf{x}, \mathbf{y}) \widehat{\mathbf{J}}^{\text{coil}}(\mathbf{y}) d\Gamma(\mathbf{y}) \\ &+ \sum_{j=1}^n \frac{\sigma_j - \sigma_{j-1}}{\sigma_k} \left( i\omega \int_{\Gamma_j} \nabla_{\mathbf{x}} u^*(\mathbf{x}, \mathbf{y}) \widehat{A}_j^\nu(\mathbf{y}) d\Gamma(\mathbf{y}) - \int_{\Gamma_j} \nabla_{\mathbf{x}} (\nabla_{\mathbf{y}} u^*(\mathbf{x}, \mathbf{y}) \cdot \boldsymbol{\nu}_j(\mathbf{y})) \widehat{\phi}_j(\mathbf{y}) d\Gamma(\mathbf{y}) \right) \end{aligned} \quad (33)$$

and boundary points  $\mathbf{x} \in \Gamma_k = \overline{\Omega}_{k-1} \cap \overline{\Omega}_k$ ,  $k = 1, 2, \dots, n$ ,

$$\begin{aligned} \widehat{\mathbf{E}}_k(\mathbf{x}) &= i\omega\mu_k \int_{\Gamma_{\text{coil}}} u^*(\mathbf{x}, \mathbf{y}) \widehat{\mathbf{J}}^{\text{coil}}(\mathbf{y}) d\Gamma(\mathbf{y}) \\ &+ 2 \sum_{j=1}^n \frac{\sigma_j - \sigma_{j-1}}{\sigma_k + \sigma_{k+1}} \left( i\omega \int_{\Gamma_j} \nabla_{\mathbf{x}} u^*(\mathbf{x}, \mathbf{y}) \widehat{A}_j^\nu(\mathbf{y}) d\Gamma(\mathbf{y}) - \int_{\Gamma_j} \nabla_{\mathbf{x}} (\nabla_{\mathbf{y}} u^*(\mathbf{x}, \mathbf{y}) \cdot \boldsymbol{\nu}_j(\mathbf{y})) \widehat{\phi}_j(\mathbf{y}) d\Gamma(\mathbf{y}) \right) \end{aligned} \quad (34)$$

are obtained from equations (9), (24), (31) and (32).

### Numerical Results

For all examples investigated in this study, the boundary integral equations (24) and (31) – (34) have been discretised by employing constant triangular boundary elements, see e.g [7], for both the coil surface,  $\Gamma_{\text{coil}}$ , and interfaces,  $\Gamma_j$ ,  $j = 1, 2, \dots, n$ , whilst  $|\widehat{\mathbf{J}}^{\text{coil}}|$  is taken to make the gradient strength of each coil equal to 30.0 mT/m and  $\omega = 1$  kHz.

Fig. 2 illustrates the numerical results obtained for the scalar potential,  $\widehat{\phi}_1(\mathbf{x})$ , at the collocation

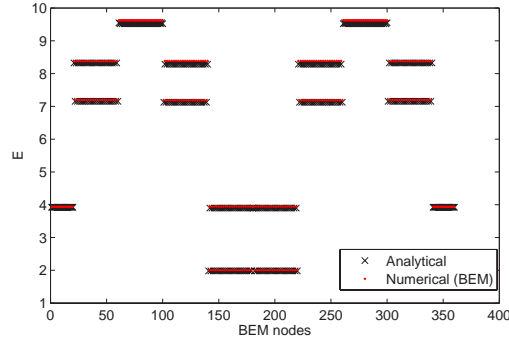


Figure 2: Analytical and BEM values for the scalar potential,  $\widehat{\phi}_1(\mathbf{x})$ , at the BEM nodes on the surface  $\Gamma_1 = \overline{\Omega}_0 \cap \overline{\Omega}_1$  of a single ( $n = 1$ ) spherical conductor  $\Omega = \Omega_1 = \{\mathbf{x} \in \mathbb{R}^3 \mid \|\mathbf{x} - \mathbf{x}^c\| < r_1\}$ , where  $r_1 = 0.2$  m and  $\mathbf{x}^c = (0.3, 0, 0)^T$ , with conductivity  $\sigma_1 = 1.0$  S/m, in the case of a switched x-gradient.

points on the surface  $\Gamma_1 = \partial\Omega_1$  of a single ( $n = 1$ ) spherical conductor  $\Omega = \Omega_1 = \{\mathbf{x} \in \mathbb{R}^3 \mid \|\mathbf{x} - \mathbf{x}^c\| < r_1\}$ , where  $r_1 = 0.2$  m and  $\mathbf{x}^c = (0.3, 0, 0)^T$ , with conductivity  $\sigma_1 = 1.0$  S/m, in the case of a switched x-gradient, in comparison with its corresponding analytical values [5]. It can be seen from this figure that the analytical and BEM based numerical results for the scalar potential on the surface  $\Gamma_1$  are in

very good agreement for a single spherical conductor, i.e.  $n = 1$ . Although not presented here, it is reported that similar results have been obtained for the electric field,  $\hat{\mathbf{E}}_1(\mathbf{x})$ , at the collocation points on the surface  $\Gamma_1 = \partial\Omega_1$ .

Further, we consider a spherical conductor  $\Omega = \Omega_1 \cup \Omega_2$  made of  $n = 2$  materials  $\Omega_1 =$

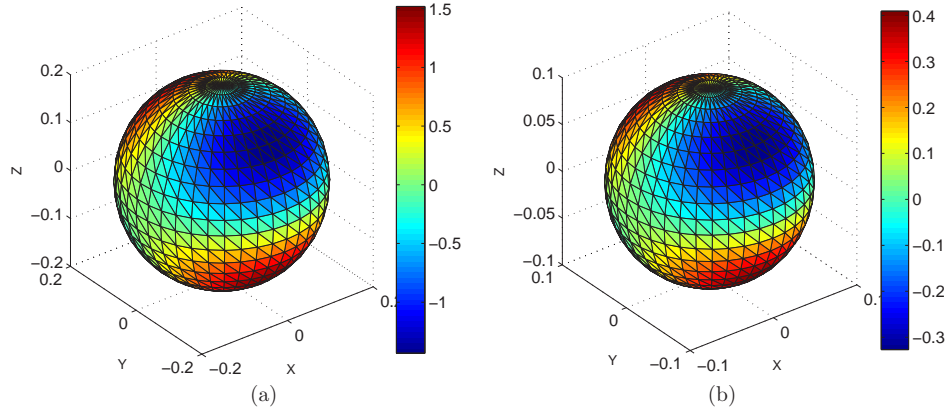


Figure 3: Numerical scalar potential,  $\hat{\phi}_j(\mathbf{x})$ ,  $j = 1, 2$ , on the surfaces (a)  $\Gamma_1 = \bar{\Omega}_0 \cap \bar{\Omega}_1$ , and (b)  $\Gamma_2 = \bar{\Omega}_1 \cap \bar{\Omega}_2$ , of the spherical conductor  $\Omega = \Omega_1 \cup \Omega_2$  consisting of  $n = 2$  materials  $\Omega_1 = \{\mathbf{x} \in \mathbb{R}^3 \mid r_2 < \|\mathbf{x} - \mathbf{x}^c\| < r_1\}$  and  $\Omega_2 = \{\mathbf{x} \in \mathbb{R}^3 \mid \|\mathbf{x} - \mathbf{x}^c\| < r_2\}$ , where  $r_1 = 0.2$  m,  $r_2 = 0.1$  m and  $\mathbf{x}^c = (0.3, 0, 0)^T$ , with conductivities  $\sigma_1 = 0.1$  S/m and  $\sigma_2 = 1.0$  S/m, respectively, in the case of a switched z-gradient.

$\{\mathbf{x} \in \mathbb{R}^3 \mid r_2 < \|\mathbf{x} - \mathbf{x}^c\| < r_1\}$  and  $\Omega_2 = \{\mathbf{x} \in \mathbb{R}^3 \mid \|\mathbf{x} - \mathbf{x}^c\| < r_2\}$ , where  $r_1 = 0.2$  m,  $r_2 = 0.1$  m and  $\mathbf{x}^c = (0.3, 0, 0)^T$ , with conductivities  $\sigma_1 = 0.1$  S/m and  $\sigma_2 = 1.0$  S/m, respectively, in the case of a switched z-gradient. The numerical results retrieved for the scalar potentials,  $\hat{\phi}_j(\mathbf{x})$ , on the surfaces  $\Gamma_j$ ,  $j = 1, 2$ , are shown in Figs. 3(a) and (b), respectively, and they represent very good approximations for their corresponding analytical values. Although not presented, it is reported that similar results have been obtained for the electric field,  $\hat{\mathbf{E}}(\mathbf{x})$ , in the subdomains  $\Omega_1$  and  $\Omega_2$ , as well as on the interfaces  $\Gamma_1$  and  $\Gamma_2$ . The present approach works equally well for a spherical conductor  $\Omega = \Omega_1 \cup \Omega_2 \cup \Omega_3$  consisting of  $n = 3$  materials  $\Omega_1 = \{\mathbf{x} \in \mathbb{R}^3 \mid r_2 < \|\mathbf{x}\| < r_1\}$ ,  $\Omega_2 = \{\mathbf{x} \in \mathbb{R}^3 \mid r_3 < \|\mathbf{x}\| < r_2\}$  and  $\Omega_3 = \{\mathbf{x} \in \mathbb{R}^3 \mid \|\mathbf{x}\| < r_3\}$ , where  $r_1 = 0.09$  m,  $r_2 = 0.06$  m and  $r_3 = 0.03$  m, with conductivities  $\sigma_1 = 1.0$  S/m,  $\sigma_2 = 0.0125$  S/m and  $\sigma_3 = 0.1$  S/m, respectively, in the case of a switched x-gradient. This is illustrated in Fig. 4, which shows the numerical electric field,  $\hat{\mathbf{E}}(\mathbf{x})$ , in the cross-section  $y = 0$ .

Finally, we consider a three-compartment model for the head, namely  $\Omega = \Omega_1 \cup \Omega_2 \cup \Omega_3$ , where the subdomains  $\Omega_1$ ,  $\Omega_2$  and  $\Omega_3$  represent the scalp ( $\sigma_1 = 1.0$  S/m), skull ( $\sigma_2 = 0.0125$  S/m) and brain ( $\sigma_3 = 1.0$  S/m), respectively. Fig. 5(a) presents the numerically retrieved scalar potential,  $\hat{\phi}_1(\mathbf{x})$ , on the brain surface,  $\Gamma_3 = \bar{\Omega}_2 \cap \bar{\Omega}_3$ , for a switched z-gradient, whilst the associated numerical electric field,  $\hat{\mathbf{E}}(\mathbf{x})$ , in the plane  $x = 0$ , is shown in Fig. 5(b).

### Conclusions

In this paper, the mathematical problem corresponding to an object subject to time varying magnetic field gradients or movement in or around an MRI scanner has been formulated in the framework of quasistatic electromagnetism. Based on the integral formulation of the problem, the induced currents in several single and multi-domains exposed to switched gradients have been calculated using constant BEM. The numerical results presented in this study for simply shaped objects exposed to switched gradients, for which analytical solutions are available, as well as a head model in the bore of a 7T magnet, have illustrated the efficiency of the proposed BEM approach. The present method can be

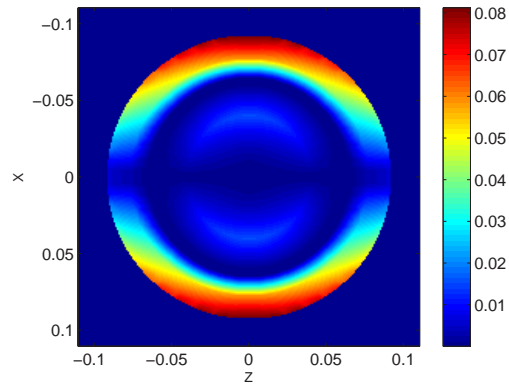


Figure 4: Numerical electric field,  $\widehat{\mathbf{E}}(\mathbf{x})$ , in the plane  $y = 0$  of the spherical conductor  $\Omega = \Omega_1 \cup \Omega_2 \cup \Omega_3$  consisting of  $n = 3$  materials  $\Omega_1 = \{\mathbf{x} \in \mathbb{R}^3 \mid r_2 < \|\mathbf{x}\| < r_1\}$ ,  $\Omega_2 = \{\mathbf{x} \in \mathbb{R}^3 \mid r_3 < \|\mathbf{x}\| < r_2\}$  and  $\Omega_3 = \{\mathbf{x} \in \mathbb{R}^3 \mid \|\mathbf{x}\| < r_3\}$ , where  $r_1 = 0.09$  m,  $r_2 = 0.06$  m and  $r_3 = 0.03$  m, with conductivities  $\sigma_1 = 1.0$  S/m,  $\sigma_2 = 0.0125$  S/m and  $\sigma_3 = 0.1$  S/m, respectively, in the case of a switched x-gradient.

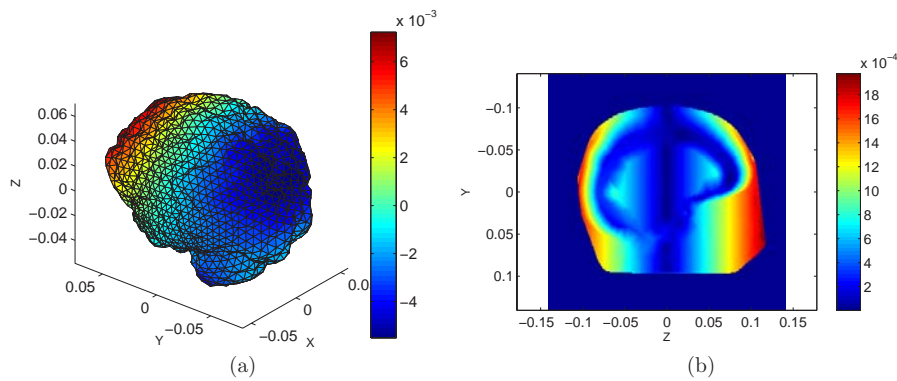


Figure 5: Numerical (a) scalar potential,  $\widehat{\phi}_1(\mathbf{x})$ , on the brain surface,  $\Gamma_3 = \overline{\Omega_2} \cap \overline{\Omega_3}$ , and (b) electric field,  $\widehat{\mathbf{E}}(\mathbf{x})$ , in the plane  $x = 0$ , for the head model  $\Omega = \Omega_1 \cup \Omega_2 \cup \Omega_3$ , where  $\Omega_1$ ,  $\Omega_2$  and  $\Omega_3$  are the scalp ( $\sigma_1 = 1.0$  S/m), skull ( $\sigma_2 = 0.0125$  S/m) and brain ( $\sigma_3 = 1.0$  S/m), respectively, in the case of a switched z-gradient.

extended to high-order BEM and combined with the domain decomposition (DDM) and fast multipole (FMM) methods in order to improve the accuracy of the results and decrease the computational time, respectively, but these are deferred to future work.

#### References

- [1] S. Crozier and L. Feng, *Progress in Biophysics and Molecular Biology*, **87**, 267-278 (2004).
- [2] N. Orcutt and O. Gandhi, *IEEE Transactions on Biomedical Engineering*, **35**, 577-583 (1998).
- [3] J. Kybic, M. Clerc, O. Faugeras, R. Keriven and T. Papadopoulos, *Physics in Medicine and Biology*, **51**, 1333-1346 (2006).
- [4] J. Kybic, M. Clerc, T. Abboud, O. Faugeras, R. Keriven and T. Papadopoulos, *IEEE Transactions on Biomedical Engineering*, **24**, 12-28 (2005).
- [5] D.B. Geselowitz, *Biophysics*, **7**, 1-11 (1967).
- [6] J.D. Jackson, *Classical Electrodynamics*, John Wiley & Sons (1999).
- [7] C.A. Brebbia, J.F.C. Telles and L.C. Wrobel, *Boundary Element Techniques*, Springer-Verlag (1984).
- [8] P.M. Morse and H. Feshbach, *Methods of Theoretical Physics*, McGraw-Hill (1953).



## Fracture analysis of magnetoelastic solids under time-harmonic loading

R. Rojas-Díaz<sup>1A</sup>, A. Sáez<sup>1B</sup>, F. García-Sánchez<sup>2</sup> and Ch. Zhang<sup>3</sup>

<sup>1</sup> Continuum Mechanics Dept. Escuela Superior de Ingenieros. University of Sevilla. Camino de los Descubrimientos S/N, E-41092 Sevilla (Spain). E-mail: <sup>1A</sup>andres@us.es and <sup>1B</sup>rrojasdiaz@us.es

<sup>2</sup> Civil Engineering Dept. Escuela de Ingenieros Industriales. University of Málaga. Campus de El Ejido S/N, E-29013 Málaga (Spain). E-mail: fgsanchez@uma.es

<sup>3</sup> Civil Engineering Dept. University of Siegen. Paul-Bonatz-Str. 9-11, D-57076 Siegen (Germany). E-mail: c.zhang@uni-siegen.de

**Keywords:** Boundary element method (BEM), magnetoelastic materials, dynamic crack analysis, fractures mechanics.

**Abstract.** The dual boundary element method (BEM) is implemented for the study of crack problems in two-dimensional (2-D) magnetoelastic solids under time-harmonic loading conditions. The Radon transform technique is used to derive the dynamic time-harmonic Green's functions for 2-D fully anisotropic magnetoelastic media. The resulting dynamic fundamental solution is obtained in the form of line integrals over a unit circumference and can be split into singular plus regular terms. The singular terms correspond to the static magnetoelastic Green's functions. In this manner, integrals containing the singular and hypersingular terms arising in the displacement and traction boundary integral equations (BIEs) are computed following the same procedure developed by the authors for statics, so that subsequently only regular (frequency dependent) terms need to be added in order to solve the dynamic problem.

### Introduction

Since the pioneering work by Van Suchtelen [1] reporting that composite materials composed of piezoelectric and elastomagnetic phases not only have the original piezoelectric and elastomagnetic properties, but also show an electromagnetic coupling effect that is not present in the constituents, these so-called magnetoelastic materials have been receiving increasing attention. Their ability to convert energy between mechanical, electric and magnetic fields makes them suitable for smart structural applications.

In this work the dual BEM is implemented for the study of crack problems in 2-D magnetoelastic solids under time-harmonic loading conditions. The Radon transform technique presented by Wang and co-workers [2,3] for anisotropic elastic and piezoelectric solids is extended to derive the dynamic time-harmonic Green's functions for 2-D fully anisotropic magnetoelastic media. As for anisotropic elastic and piezoelectric solids, the resulting dynamic fundamental solution is obtained in the form of line integrals over a unit circumference that can be further decomposed into a singular part plus a regular part. The singular part corresponds to the static magnetoelastic Green's functions, whilst the regular part represents the contribution of the inertial terms in the equations of motion. In this manner, integrals containing the singular and hypersingular terms arising in the displacement and traction BIEs are computed following the same procedure developed by the authors [4] for statics, so that subsequently only regular (frequency dependent) terms need to be added in order to solve the dynamic problem. Results for scattering of P-waves by various crack configurations are presented and discussed.

### Basic Equations and Dual BEM Formulation

The governing equations for a linear magnetoelastic material may be written in an elastic-like fashion by considering a generalized displacement vector extended with the electric ( $\phi$ ) and magnetic potentials ( $\varphi$ ) and a generalized stress tensor extended with the electric displacements ( $D_i$ ) and the magnetic inductions ( $B_i$ ) [5]

$$u_I = \begin{cases} u_i & I=1,2 \\ \phi & I=3 \\ \varphi & I=4 \end{cases} ; \quad \sigma_{iJ} = \begin{cases} \sigma_{ij} & J=1,2 \\ D_i & J=3 \\ B_i & J=4 \end{cases} \quad (1)$$

so that the generalized equations of motion can be expressed as

$$C_{iJKl} u_{K,il} = -F_J + \rho \delta_{JK}^* \frac{\partial^2 u_K}{\partial t^2} \quad (2)$$

where  $\rho$  is the mass density and  $C_{iJKl}$  is the extended elasticity tensor

$$C_{iJKl} = \begin{cases} C_{ijkl} & J, K=1,2 & e_{ikl} & J=3; K=1,2 & h_{ikl} & J=4; K=1,2 \\ e_{ij} & J=1,2; K=3 & -\kappa_{il} & J, K=3 & -\beta_{il} & J=4; K=3 \\ h_{ij} & J=1,2; K=4 & -\beta_{il} & J=3; K=4 & -\gamma_{il} & J, K=4 \end{cases} \quad (3)$$

where  $C_{ijkl}$ ,  $\kappa_{il}$  and  $\gamma_{il}$  denote elasticity tensor, dielectric permittivities and magnetic permeabilities, respectively and  $e_{ij}$ ,  $h_{ij}$  and  $\beta_{il}$  are the piezoelectric, piezomagnetic and magnetoelastic coupling coefficients, respectively. In eq (2)  $\delta_{JK}^*$  is the generalized Kronecker delta and  $F_J$  is the generalized body force vector

$$\delta_{JK}^* = \begin{cases} \delta_{jk} & J, K=1,2 \\ 0 & J, K=3,4 \end{cases} ; \quad F_J = \begin{cases} b_j & J=1,2 \\ -f_e & J=3 \\ -f_m & J=4 \end{cases} \quad (4)$$

where  $b_j$  are the body forces and  $f_e$  and  $f_m$  are the electric charge density and the magnetic current density, respectively.

The dual BEM approach for fracture mechanics applications may be then expressed using the extended formulation in terms of both the displacement and traction boundary integral equations as usual [6]

$$c_{IJ} u_J + \int_{\Gamma} p_{IJ}^* u_J d\Gamma = \int_{\Gamma} u_{IJ}^* p_J d\Gamma \quad ; \quad c_{IJ} p_J + N_r \int_{\Gamma} s_{rIJ}^* u_J d\Gamma = N_r \int_{\Gamma} d_{rIJ}^* p_J d\Gamma \quad (5)$$

In eq (5),  $c_{IJ}$  represents the free-term coefficients,  $p_J$  denotes the extended traction vector,  $N_r$  is the unit outward normal vector,  $u_{IJ}^*$  is the displacement fundamental solution,  $p_{IJ}^*$  is the traction fundamental solution, and the fundamental solutions  $s_{rIJ}^*$  and  $d_{rIJ}^*$  are defined by eq (18).

The 2-D and 3-D time-harmonic fundamental solutions have been recently derived by Rojas-Díaz et al. [5] by extending the Radon transform technique [2,3] to the magnetoelastoelectric case. The resulting fundamental solution is further decomposed into a sum of singular plus regular parts. Since the singular part coincides with the static fundamental solution, integrals containing the singular and hypersingular terms arising in the displacement and traction BIEs can be computed following the same procedure developed by the authors [4] for statics, so that subsequently only regular (frequency dependent) terms need to be added in order to solve the dynamic problem.

Furthermore, since the obtained fundamental solution expressions show deep similarities with the ones previously presented for the anisotropic [2] and piezoelectric [3] material cases, the meshing strategy and the regularization of the singular and hypersingular kernels follow from extending the previous work by Sáez et al. [6] for piezoelectric dynamic fracture analysis.

In particular, cracks are meshed using discontinuous quadratic elements and the asymptotic behavior of the extended crack-opening-displacements near the tip of the crack is captured by the use of discontinuous

quarter-point elements. As in [4], extended field intensity factors (electric displacement intensity factor (EDIF)  $K_D$ , magnetic induction intensity factor (MIIF)  $K_B$  and stress intensity factors (SIF)  $K_I$  and  $K_{II}$ ) can be obtained directly from the nodal values of the extended crack-opening-displacements  $\Delta u_1$ ,  $\Delta u_2$ ,  $\Delta \phi$  and  $\Delta \varphi$  at the quarter-point element from

$$\mathbf{K} = \begin{pmatrix} K_{II} \\ K_I \\ K_D \\ K_B \end{pmatrix} = \sqrt{\frac{\pi}{8r}} \mathbf{H}^{-1} \begin{pmatrix} \Delta u_1 \\ \Delta u_2 \\ \Delta \phi \\ \Delta \varphi \end{pmatrix} \quad (6)$$

with  $r$  being the distance from the collocation node to the crack tip and  $\mathbf{H}$  depending on the material constants [4].

**Time-Harmonic Fundamental Solutions**

The displacements of the 2-D time-harmonic fundamental solutions obtained in reference [5] are given by

$$u_{KM}^*(\mathbf{x}, \omega) = u_{KM}^{*S}(\mathbf{x}) + u_{KM}^{*R}(\mathbf{x}, \omega) \quad (7)$$

with

$$u_{KM}^{*S}(\mathbf{x}) = -\frac{1}{4\pi^2} \int_{|\eta|=1} \frac{\varepsilon_{KM}^q}{\rho c_q^2 E_{pp}^q} \log|\boldsymbol{\eta} \cdot \mathbf{x}| dL(\boldsymbol{\eta}) - \frac{1}{4\pi^2} \int_{|\eta|=1} \Lambda_{KM} \log|\boldsymbol{\eta} \cdot \mathbf{x}| dL(\boldsymbol{\eta}) \quad (8)$$

$$u_{KM}^{*R}(\mathbf{x}, \omega) = \frac{1}{16\pi^2} \int_{|\eta|=1} \frac{\varepsilon_{KM}^q}{\rho c_q^2 E_{pp}^q} \Phi^R(k_q, |\boldsymbol{\eta} \cdot \mathbf{x}|) dL(\boldsymbol{\eta}) \quad (9)$$

where the line integrals are defined along a unit circumference and

$$E_{km}^q = \text{adj}(Z_{km} - \rho c_q^2 \delta_{km}) \quad (10)$$

with  $c_q$  being the phase velocities and

$$Z_{km} = \Gamma_{km} + \alpha_m^4 \Gamma_{k4} + \alpha_m^5 \Gamma_{k5} \quad ; \quad \alpha_m^4 = \frac{\Gamma_{4k} \Gamma_{55} - \Gamma_{45} \Gamma_{5k}}{\Gamma_{45} \Gamma_{54} - \Gamma_{44} \Gamma_{55}} \quad ; \quad \alpha_m^5 = \frac{\Gamma_{44} \Gamma_{5k} - \Gamma_{4k} \Gamma_{54}}{\Gamma_{45} \Gamma_{54} - \Gamma_{44} \Gamma_{55}} \quad (11)$$

$$\Gamma_{KM} = C_{iKM} \eta_i \eta_l \quad (12)$$

$$\varepsilon_{KM}^q = \begin{cases} E_{km}^q & K, M = 1, 2, 3 \\ \alpha_i^K E_{lm}^q & K = 4, 5 \quad ; \quad M = 1, 2, 3 \\ \alpha_i^K \alpha_j^M E_{ij}^q & K, M = 4, 5 \end{cases} \quad (13)$$

$$\Lambda_{KM}(\mathbf{x}) = \frac{1}{\Gamma_{45} \Gamma_{54} - \Gamma_{44} \Gamma_{55}} \left\{ \Gamma_{KM} (\delta_{4K} \delta_{5M} + \delta_{5K} \delta_{4M}) - \frac{\Gamma_{44} \Gamma_{55}}{\Gamma_{KM}} (\delta_{4K} \delta_{4M} + \delta_{5K} \delta_{5M}) \right\} \quad (14)$$

$$\Phi^R(k_q, |\mathbf{n} \cdot \mathbf{x}|) = \Phi(k_q |\mathbf{n} \cdot \mathbf{x}|) + 2 \log(|\mathbf{n} \cdot \mathbf{x}|) \quad (15)$$

$$\Phi(\zeta) = i\pi e^{i\zeta} - 2 \left[ \cos(\zeta) \text{ci}(\zeta) + \left[ \sin(\zeta) \text{si}(\zeta) \right] \right] \tag{16}$$

$$\text{ci}(\zeta) = - \int_{\zeta}^{\infty} \frac{\cos z}{z} dz \quad ; \quad \text{si}(\zeta) = - \int_{\zeta}^{\infty} \frac{\sin z}{z} dz \tag{17}$$

The traction fundamental solution  $p_{MJ}^*$  follows from the differentiation of the displacements and the substitution into the generalized Hooke's law and the kernels of the traction BIEs follow from

$$d_{r,lj}^* = C_{rIMl} u_{MJ,l}^* \quad ; \quad s_{r,lj}^* = C_{rIMl} p_{MJ,l}^* \tag{18}$$

**Numerical Examples**

Scattering of a time-harmonic plane P-wave impinging normally onto a straight-line crack in an infinite domain is first analyzed. The material is a degenerate one that models a piezoelectric PZT-6B, so that the obtained results may be compared with the semi-analytical solution given by Shindo and Ozawa [7] in order to validate the approach. Fig. 1 illustrates the good agreement obtained between both sets of results for the normalized values of mode I SIF versus dimensionless frequency  $\omega a / c_s$  where  $c_s = \sqrt{C_{66} / \rho}$ .

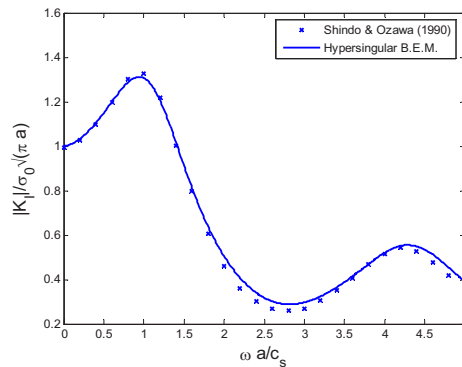


Figure 1: Normalized mode I SIF for straight-line crack under impinging P-wave

Wave scattering by a circular arch crack in an infinite magneto-electroelastic BaTiO<sub>3</sub>-CoFe<sub>2</sub>O<sub>4</sub> composite with a volume fraction V<sub>f</sub>=0.5 is next considered. Material properties can be found in reference [4]. The geometry of the problem is shown in Fig. 2. The magnetic and the electric poling directions of the material coincide with the x<sub>2</sub>-axis. All crack-faces are free of tractions, external charge and electric current. Electrically and magnetically impermeable boundary conditions on the crack-faces are assumed. The incident P-wave impinges along the material poling axis and normally to the x<sub>1</sub>-axis. The crack is meshed with 10 elements. The ones at the tips are very small (arch length/30) quarter-point straight elements whilst the rest are curved quadratic discontinuous boundary elements.

The incident P-wave motion is characterized by the following extended displacement components

$$\begin{pmatrix} u \\ v \\ \varphi \\ \phi \end{pmatrix} = \begin{pmatrix} 0 \\ v_0 \\ \varphi_0 \\ \phi_0 \end{pmatrix} \exp \left[ i\omega \left( \frac{y}{c_p} + t \right) \right] \quad \text{where} \quad c_p = \sqrt{\frac{1}{\rho} \left( C_{22} + \frac{e_{22}^2}{\kappa_{22}} + \frac{h_{22}^2}{\alpha_{22}} \right)} \tag{19}$$

with the associated extended stress components given by

$$\begin{pmatrix} \sigma_x \\ \sigma_y \\ \sigma_{xy} \\ D_x \\ D_y \\ B_x \\ B_y \end{pmatrix} = \begin{pmatrix} C_{12}v_0 + e_{21}\phi_0 + h_{21}\phi_0 \\ C_{22}v_0 + e_{22}\phi_0 + h_{22}\phi_0 \\ 0 \\ 0 \\ e_{22}v_0 - \kappa_{22}\phi_0 - \alpha_{22}\phi_0 \\ 0 \\ h_{22}v_0 - \alpha_{22}\phi_0 - \gamma_{22}\phi_0 \end{pmatrix} \frac{i\omega}{c_p} \exp \left[ i\omega \left( \frac{y}{c_p} + t \right) \right] \quad (20)$$

Fig. 3 illustrates the behavior of the mode I and mode II SIF for different arch semi-angles  $\theta$  versus the dimensionless frequency. EDIF and MIIF are plotted in Fig. 4.

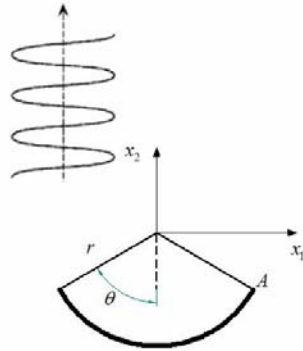


Figure 2: Curved (circular arch) crack under impinging P-wave

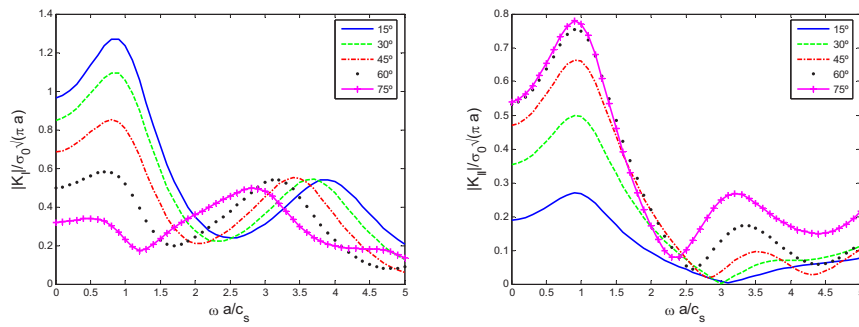


Figure 3: Normalized modes I and II SIF versus dimensionless frequency for curved crack under impinging P-wave

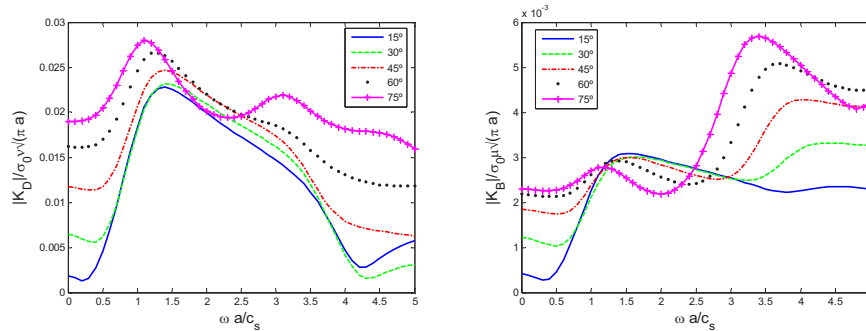


Figure 4: Normalized EDIF and MIIF versus dimensionless frequency for curved crack under impinging P-wave

### Conclusions

A 2-D time-harmonic dynamic crack analysis in fully anisotropic and linear magnetoelastoelectric solids by a hypersingular BEM is presented. The formulation combines the classical displacement BIEs and the hypersingular traction BIEs. The fundamental solution is derived by using the Radon transform. Strongly singular and hypersingular boundary integrals computation follows the previous work by the authors for static fracture analysis [4]. Numerical examples for computing the dynamic fracture parameters are presented to verify the present frequency-domain BEM.

### References

- [1] J. Van Suchtelen, Product properties: a new application of composite materials, Phillips Research Reports 27 (1972) 28-37.
- [2] C.-Y. Wang and J.D. Achenbach, Elastodynamic fundamental solutions for anisotropic solids, Geoph. J. Int. 118 (1994) 384-392.
- [3] C.-Y. Wang and Ch. Zhang, 3-D and 2-D dynamic Green's functions and time-domain BIEs for piezoelectric solids, Engng. Anal. Bound. Elem. 29 (2005) 454-465.
- [4] F. García-Sánchez, R. Rojas-Díaz, A. Sáez and Ch. Zhang, Fracture of magnetoelastoelectric composite materials using boundary element method (BEM), Theoretical and Applied Fracture Mechanics 47 (2007) 192-204.
- [5] R. Rojas-Díaz, A. Sáez, F. García-Sánchez and Ch. Zhang, Time-harmonic Green's functions for anisotropic magnetoelastoelectricity, Int. J. Solids & Struc., submitted for publication (2006).
- [6] A. Sáez, F. García-Sánchez and J. Domínguez, Hypersingular BEM for dynamic fracture in 2-D piezoelectric solids, Comput. Methods Appl. Mech. Engrg 196 (2006) 235-246.
- [7] Y. Shindo, and E. Ozawa, Dynamic analysis of a cracked piezoelectric material, Mechanical Modelling of New Materials, Ed. R.K.T Hsieh, Elsevier Science Publishers B.V., 1990:297-304.

**OPTIMAL SHAPE DESIGN OF FIBERS IN COMPOSITES**P.Prochazka<sup>1</sup>, Z. Sharif Khodaei<sup>2</sup> and J.Zeman<sup>3</sup>

<sup>1</sup>Czech Technical University in Prague, Faculty of Civil Engineering, Department of Mechanics,  
Thákurova 7, 166 29 Prague 6, Czech Republic,  
e-mail:petr.proch@gmail.com

<sup>2</sup>Czech Technical University in Prague, Faculty of Civil Engineering, Department of Mechanics,  
Thákurova 7, 166 29 Prague 6, Czech Republic  
e-mail:Zahra.sharif@gmail.com

<sup>3</sup>Czech Technical University in Prague, Faculty of Civil Engineering, Department of Mechanics,  
Thákurova 7, 166 29 Prague 6, Czech Republic,  
e-mail:zemanj@cml.fsv.cvut.cz

**Keywords:** Optimal shape design, composites, Inverse variational principles, Boundary elements

**1. Introduction**

Inverse variational principles proved their importance in shape optimization of structures. In this paper, they are applied to search of optimal shape of fibers in a composite structure. As the boundary element method seems to be more promising than other modern numerical methods in moving boundary problems, the boundary element method is redefined to enable one an approach, which leads to a possibility of expressing optimal interfacial energies and, hence, to the optimal bearing capacity of the composite structure. Standard procedure in the finite elements leads to dependence of the stiffness matrix on the shape of the fibers, it means the way of meshing plays very important role and the results are directly dependent of the meshing strategy. In this case, following the basic idea for homogenization and localization, concentration factors have to be expressed in terms of the boundary element method instead. These terms are dependent on the shape of the fibers. It appears that still the procedure is not convergent (we solve a strongly nonlinear problem); additional constraint has to be involved in the formulation.

Conventionally, the optimal shape design problems consist of minimization of an appropriate cost functional with certain constraints, such as equilibrium and compatibility conditions and design requirements. The formulation of the cost functional depends of the concrete intention of a designer. One of a reasonable and practical form of the cost functional respects the minimization of the strain energy of the body subjected to a specific load. Such a problem can easily be formulated in terms of inverse variational principles, which assure that the surface energy attains its minimum.

Inverse variational principles, leading to optimization of surface energy of bodies, were established by Prof. Buefner from Darmstadt University, Germany, at the end of sixties of the previous century. Later on, they were developed by some authors, but published mostly at local, although international, conferences. Interesting application of the inverse variational principles is issued in [1], [2], where numerical experience is discussed. The results from these discussions are also used in this paper. Numerical tools for solving the problems in terms of the inverse variational principles are finite elements. General formulation of the inverse variational principles is presented in [3] for elastic media.

Paper [4] is focused on optimization problems based on the inverse variational principles solved by boundary elements. In the paper optimal thickness of beams (stretched plates) is studied and on some examples the ability of the procedure is shown. This approach is extraordinarily advantageous, as no internal mesh has to be generated (the results are strongly dependant on a topology of the mesh), but new variational principle has to be formulated, namely the internal energy is expressed using the integral relations following from the boundary element method.

Since we are concentrated on optimization of composite structures using homogenization, the theory for periodic media given by Suquet, [5], is used in this paper. Similarly to Suquet's examples symmetric problems are considered.

First, optimization problem is formulated in this paper, and a solution of it is suggested and discussed from the point of solvability and uniqueness. Then homogenization and localization, having the principal

meaning in the approach introduced in this paper, are briefly discussed using the boundary element method. The main goal is the computation of concentration factors, which can be received from localization on unit cell and applied to homogenization and energetic functional, important for obtaining optimal shape design of fibers.

## 2. Formulation of the problem

Problems of optimal shape of structures can be formulated as follows: Let the displacements field  $\mathbf{u}$  be a solution of a partial differential equation (or, alternatively,  $\mathbf{u}$  is a solution of a variational principle) in the domain  $\Omega$ . Let  $E(\mathbf{u}, \Omega)$  be a real function of  $\mathbf{u}$  and  $\Omega$ . The problem of optimal shape consists of finding such a domain from a class  $O$  of admissible domains, which minimizes  $E$ . It may symbolically be written as:

$$\text{Min } \{E(\mathbf{u}, \Omega); A(\mathbf{u}, \Omega) = 0\} \quad (1)$$

where  $A$  is a differential operator, which for each  $\Omega \in O$  uniquely determines the displacement field  $\mathbf{u}$ .

One of a reasonable and practical form of requirements of designers is assumption of minimum deformation energy of structure subject to a certain load distribution. Just such a problem may be formulated in terms of inverse variational principles. In order to ensure the correctness of this formulation, additional constraint conditions have to be applied. In our case we assume the constant volume of the structure; this is one of the main features of inverse variational principles.

Note that in the other problems other constraints may be applied. Even the coefficient  $C$  may be made free and turned to a variable (it remains no longer constant). Then more complicated formulation is expected, involving  $C$  as an additional variable in the principle.

Inverse variational principle based on the principle of minimum strain energy constrained by a constant volume of the structure can be written in the following form:

$$\Pi(\mathbf{u}, \Omega) = \frac{1}{2} \int_{\Omega} \sigma_{ij} \varepsilon_{ij} d\Omega - \int_{\Gamma_p} \bar{p}_i u_i d\Gamma + \lambda \left( \int_{\Omega} d\Omega - C \right) \rightarrow \text{stationary}, \quad i, j = 1, 2 \quad (2)$$

where  $u_i, \varepsilon_{ij}$ , and  $\sigma_{ij}$  are components of the admissible displacement vector, strain tensor, and stress tensor, respectively,  $\bar{p}_i$  are components of the prescribed tractions along the boundary  $\Gamma$  of the domain  $\Omega \in O$  ( $\Gamma = \Gamma_u \cup \Gamma_p, \Gamma_u \cap \Gamma_p = \emptyset$ ).  $\Gamma_p$  is the part of the boundary  $\Gamma$  where the tractions are prescribed. Body forces are neglected.

For homogeneous material of the body under consideration Clapeyron's theorem turns the functional (2) to a form involving only the boundary integrals, see [6]. In the cited paper even some improvement of the accuracy of the integral equations is proposed. Actually, when applying the Green's theorem to the functional (2) we get, [4]:

$$\Pi(\mathbf{u}, \Omega) = \frac{1}{2} \int_{\Gamma} u_i p_i d\Gamma - \int_{\Gamma_p} \bar{p}_i u_i d\Gamma + \lambda \left( \int_{\Omega} d\Omega - C \right) \rightarrow \text{stationary}, \quad i, j = 1, 2 \quad (3)$$

Let us approximate the boundary displacement vector and vector of the tractions as

$$u_i(x) = \Phi_{ij}(x) U_j, \quad p_i(x) = \Psi_{ij} P_j, \quad x \in \Gamma \quad (4)$$

where  $\Phi$  and  $\Psi$  are matrices of interpolation (base) functions of  $u_i$  and  $p_i$  on the boundary elements. Vectors  $U_i$  and  $P_i$ ,  $i = 1, \dots, n$ , are ordered approximations of the displacements and tractions, respectively, at selected boundary nodal points.  $n$  is the number of freedom on the boundary. The direct boundary element method leads us to the matrix equation, see [6]:

$$A_{ij} U_j = B_{ij} P_j, \quad P_i = B_{ij}^{-1} A_{jk} U_k = Z_{ik} U_k. \quad (5)$$

where  $A_{ij}, B_{ij}$  are square matrices  $n \times n$ . The second equation (5) is derived from the fact that the matrix  $\mathbf{B}$  is regular. Actually, if the displacements  $\mathbf{u}$  will be prescribed all over the boundary, the tractions are uniquely defined.

Substituting (5) and (4) to (3) yields:

$$\Pi(\mathbf{u}, \Omega) = \frac{1}{2} K_{ij} U_i U_j - F_i U_i + \lambda \left( \int_{\Omega} d\Omega - C \right) \rightarrow \text{stationary}, \quad i, j = 1, 2 \quad (6)$$

where

$$K_{ij} = \int_{\Gamma} \Phi_{ki}(x) \Psi_{kj}(x) d\Gamma Z_{ji}, \quad F_i = \int_{\Gamma_p} \Phi_{ji}(x) \bar{p}_j d\Gamma. \quad (7)$$

Our aim will now be to formulate the domain by means of its corresponding boundary. This can be done in many ways, for example suppose a polygonal shape of the structure under study, where the edges of the polygon are created by boundary elements. One can choose some fixed point  $P$  (pole) and connect it with each vertex of this polygonal boundary. In this way we obtain  $N$  triangles  $T_k$ , where  $k = 1, \dots, N$ ,  $N$  is the number of vertices. Since integral  $\int_{\Omega} d\Omega = \text{meas } \Omega$ , i.e. measure of the domain, the measure may then be

written as:

$$\text{meas } \Omega = \sum_{k=1}^N \text{meas}(T_k), \quad (8)$$

where  $\text{meas}(T_k)$  stands for the algebraic measure of  $T_k$ .

Now define the shape variables  $s_k$ ,  $k = 1, \dots, M$ . Taking account of the above arguments, the discretized inverse variational principle is formulated in the following manner:

$$\Pi(\mathbf{u}, \Omega) = \frac{1}{2} K_{ij}(s) U_i U_j - F_i U_i + \lambda \left( \int_{\Omega} \text{meas}(T_k) - C \right) \rightarrow \text{stationary}, \quad i, j = 1, 2 \quad (9)$$

where  $\mathbf{s} = \{s_1, s_2, \dots, s_M\}$  is the vector of shape variables.

### 3. Localization and homogenization of symmetric periodic structures

Localization and homogenization is concisely described in Suquet, [5]. Here we only briefly mention the approach and will not go into details. Recall some basic consumption which we use later in the integral formulations. First, we denote quantities used in this text. Two different scales will naturally be introduced. The macroscopic scale, the homogeneous law in which is sought, will be described in coordinate system  $\mathbf{x} \equiv \{x_1, x_2, x_3\}^T$  and the microscopic scale - heterogeneous - is characterized in the system of coordinates  $\mathbf{y} \equiv \{y_1, y_2, y_3\}^T$ . The medium is generally heterogeneous, but locally - in the microscopic scale - is assumed to be periodic, thus a representative volume element may be cut out from the structure and the periodicity conditions can be introduced on the boundary of this element.

Let us distinguish the quantities under study in dependence of the macroscopic or microscopic scale in the following manner: The displacements in the macroscopic level will be denoted as  $\mathbf{U} \equiv \{U_1, U_2, U_3\}^T$  while in the microscopic level as  $\mathbf{u} \equiv \{u_1, u_2, u_3\}^T$ . Moreover, in macroscopic level, let us denote strains as  $\mathbf{E} \equiv \{E_{ij}\}$ ,  $i, j = 1, 2, 3$  and stresses as  $\mathbf{S} \equiv \{S_{ij}\}$ ,  $i, j = 1, 2, 3$ . In the microscopic level let us denote strains as  $\mathbf{\varepsilon} \equiv \{\varepsilon_{ij}\}$ ,  $i, j = 1, 2, 3$  and stress as  $\boldsymbol{\sigma} \equiv \{\sigma_{ij}\}$ ,  $i, j = 1, 2, 3$ . Define also the microscopic-macroscopic relation of the averaged stresses and strains by

$$S_{ij} = \frac{1}{\text{meas}\Omega} \int_{\Omega} \sigma_{ij} \, d\Omega = \langle \sigma_{ij} \rangle, \quad E_{ij} = \frac{1}{\text{meas}\Omega} \int_{\Omega} \varepsilon_{ij} \, d\Omega = \langle \varepsilon_{ij} \rangle \quad (10)$$

where  $\langle . \rangle$  stands for the average,  $\Omega$  is the representative volume element, and  $\text{meas } \Omega$  is its volume,  $\Omega = \Omega^f \cup \Omega^m$ ,  $\Omega^f \cap \Omega^m = 0$ ,  $\Omega^f$  denotes the domain of fiber and  $\Omega^m$  is the domain of matrix. As usual,  $\text{meas } \Omega$  is set to be a unity. Note that average usually means homogenization, but one should use that term with care: there are many kinds of averaging.

The elasticity system (equilibrium equations, kinematical conditions and Hooke's law) is defined as (small deformation theory is imposed):

$$\text{div } \boldsymbol{\sigma}(\mathbf{y}) = 0, \quad \boldsymbol{\sigma}(\mathbf{y}) = \mathbf{L}(\mathbf{y}) : \boldsymbol{\varepsilon}(\mathbf{y}), \quad \boldsymbol{\varepsilon} = \frac{1}{2}(\nabla \mathbf{u} + \nabla^T \mathbf{u}) \quad \text{in } \Omega \quad (11)$$

and periodic boundary conditions along the boundary of the unit cell  $\partial\Omega$  are given.

*Localization* consists of the solution of system of elasticity system (equilibrium equations, kinematical conditions and Hooke's law) on the representative volume element (or unit cell) for concentration factors  $A^f$  of fibers and  $A^m$  for matrix:

$$\begin{aligned} \varepsilon_{ij}^f(\mathbf{u}(\mathbf{y})) &= A_{ijkl}^f(\mathbf{y}) E_{kl}, & \mathbf{y} \in \Omega^f \\ \varepsilon_{ij}^m(\mathbf{u}(\mathbf{y})) &= A_{ijkl}^m(\mathbf{y}) E_{kl}, & \mathbf{y} \in \Omega^m \end{aligned} \quad (12)$$

Periodic boundary conditions will be employed on  $\partial\Omega$ . If  $\mathbf{n} \equiv \{n_1, n_2, n_3\}$  is outward unit normal to  $\partial\Omega$ , it holds:

stress: components of tractions  $p_i = \sigma_{ij} n_j$  are opposite on the opposite sides,

strains: the local strain tensor  $\boldsymbol{\varepsilon}(\mathbf{u})$  is split into its average  $\mathbf{E}$  and a fluctuating term  $\bar{\boldsymbol{\varepsilon}}(\mathbf{u})$  as:

$$\boldsymbol{\varepsilon}(\mathbf{u}) = \mathbf{E} + \bar{\boldsymbol{\varepsilon}}(\mathbf{u}), \quad \bar{\boldsymbol{\varepsilon}}(\mathbf{u}) = \boldsymbol{\varepsilon}(\mathbf{u}^*), \quad \langle \boldsymbol{\varepsilon}(\mathbf{u}^*) \rangle = 0 \quad (13)$$

displacements:  $u_i^*$  are the same at opposite sides. Hence, the fluctuating displacement  $\mathbf{u}^*$  may be considered a *periodic field*, up to a rigid displacement that will be disregarded. The geometry and denotation is obvious from Fig. 1 for 2D case. Interfacial surface between fiber and matrix is denoted by  $\Gamma$ .

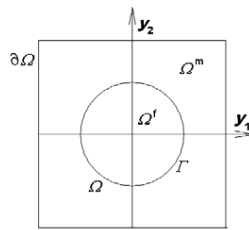


Figure 1: Unit cell used in the study

As we concentrate on symmetric problems, and linear elasticity is considered the problem is studied only in the first quarter of the unit cell.

Under the above described circumstances Hill's energy condition holds valid, as can be easily proved:

$$\langle \sigma_{ij}(\mathbf{y}) \varepsilon_{ij}(\mathbf{y}) \rangle = S_{ij} E_{ij} \quad (14)$$

Using (1), (2) and (3) the components of the overall stresses are written in the following way:

$$S_{ij} = \langle \sigma_{ij}(\mathbf{y}) \rangle = \langle L_{ijkl}(\mathbf{y}) \varepsilon_{kl}(\mathbf{y}) \rangle = \langle L_{ijkl}^f A_{kla\beta}^f(\mathbf{y}) \rangle_f + \langle L_{ijkl}^m A_{kla\beta}^m(\mathbf{y}) \rangle_m E_{a\beta} \quad (15)$$

where  $\langle \cdot \rangle_f$  stands for the average on the fiber and  $\langle \cdot \rangle_m$  is the average on the matrix. This averaging process is made in such a way that the integrals are taken over the fiber and matrix, respectively.

By definition, the homogenized stiffness matrix  $L^*$  is written as:

$$S_{ij} = L_{ijkl}^* E_{kl} \quad (16)$$

Comparing (15) and (16) the overall stiffness matrix follows as

$$L_{ijkl}^* = \langle L_{ijkl}^f A_{kla\beta}^f(\mathbf{y}) \rangle_f + \langle L_{ijkl}^m A_{kla\beta}^m(\mathbf{y}) \rangle_m \quad (17)$$

Since the problem remains linear elastic, superposition of loadings due to successively given by components of the overall strain tensor can be used. The overall strain  $E_{ij}$  is assumed to be given independently of the shape of the unit cell and of the shape of the fiber. The loading of this unit cell will be given by unit impulses of  $E_{ij}$ , i.e. we successively select  $E_{i_0 j_0} = E_{j_0 i_0} = 1$ ;  $E_{ij} = 0$  for either  $i_0 \neq i$  or  $j_0 \neq j$ .

#### 4. Euler's equations

The stationary requirement leads to differentiation of the functional by the shape (design) parameters  $p_s$ .

$$\frac{\partial \Pi(\mathbf{u}, \Omega)}{\partial s_t} = \frac{1}{2} [L_{ijkl}^f \langle \frac{\partial A_{kla\beta}^f(s)}{\partial s_t} \rangle_f + L_{ijkl}^m \langle \frac{\partial A_{kla\beta}^m(s)}{\partial s_t} \rangle_m] E_{ij} E_{a\beta} + \lambda \frac{\partial}{\partial s_t} \int_{\Omega^t} d\Omega = 0 \quad (18)$$

which can be rewritten as:

$$E_t + \lambda = 0, \quad t = 1, 2, \dots, n \quad (19)$$

where

$$\lambda = - \frac{\frac{1}{2} [L_{ijkl}^f \langle \frac{\partial A_{kla\beta}^f(s)}{\partial s_t} \rangle_f + L_{ijkl}^m \langle \frac{\partial A_{kla\beta}^m(s)}{\partial s_t} \rangle_m] E_{ij} E_{a\beta}}{\frac{\partial}{\partial s_t} \int_{\Omega^t} d\Omega} \quad \text{for each } t = 1, \dots, n$$

If we have claimed  $s_t$ ,  $t = 1, \dots, n$  the distances of the origin from the current boundary of the fiber,  $E_t$  corresponds to the strain energy density at the point of the interfacial boundary, in our case at the nodal point  $\xi_t$ . The equation (16) requires  $E_t$  to have the same value for any  $t$ . In other words, if the strain energy density were the same at any point on the "moving" part of the boundary, the optimal shape of the trial body would be reached. For this reason the body of the structure should increase its area (in 3D its volume) at the nodal point  $\xi_t$  of the boundary, if  $E_t$  is larger than the true value of  $-\lambda$ , while it should decrease its value when  $E_t$  is smaller than the correct  $-\lambda$ . As, most probably, we will not know the real value  $-\lambda$  in advance; we estimate it from the average of the current values at the nodal points.

Since  $E_t$ , prove large differences in their values, logarithmic scale was proposed by Tada, Seguchi and Soh, [2]. The computational procedure follows this idea.

Differentiation by  $\lambda$  completes the system of Euler's equations to get (8).

#### 5. Example

Unit cell is considered with fiber volume ratio equal to 0.6. Since we compare energy densities at nodal points of the interfacial boundary, the relative energy density may be regarded as the comparative quantity influencing the movement of the boundary  $\Gamma$ . As said in the previous section, the higher value of this energy, the larger movement of the nodal point of  $\Gamma$  should aim at the optimum.

In both cases of volume ratios we used the following material properties of phases: Young's modulus of fiber  $E^f = 210$  MPa, Poisson's ratio  $\nu^f = 0.16$ ; on the matrix  $E^m = 17$  MPa, and  $\nu^m = 0.3$ .

We started with the radius  $r = 0.714$  of a circle and "unit moves" of the parameters  $p_s$  where given by the change of radius by 2.2 %.

In Fig. 3 the distribution of relative energies  $E_s$  is depicted along the interfacial boundary and the optimal shape of the fiber is drawn. These results are obtained using boundary elements, [7], and are in accordance with results gained from the FEM.

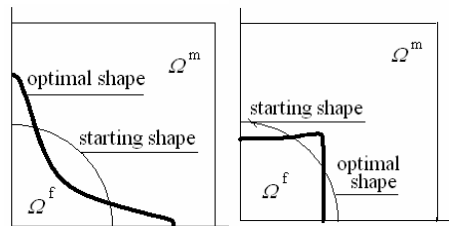


Figure 2: Relative energy in the first step and optimal shape

## 6. Conclusions

In this paper inverse variational principle has been applied to the solution of optimal fiber shape design on a unit cell of periodic composite structure. When searching for optimal shape design of fibers in composite structures, many formulations have been used in the past. They very often start with minimum strain energy function. This assumption is in inverse variational principles fulfilled implicitly. A natural requirement is the restriction to the constant volume or area in many methods of solution of optimal shape design of composites, say, when solving a periodic distribution of fibers.

The requirement of the constant volume or area seems to be restrictive, particularly when expecting application of inverse variational principles to larger range of problems. Actually, it is not so. The constant  $C$  may change, too. Thus the formulation has to be extended in such a way that  $C$  is involved into the problem as a new variable and may be varied (differentiated) in some reasonable way. It is necessary to point out that the extreme of the functional  $I$  is found as neither the minimum nor the maximum, but the functional should be minimum with respect to the displacements and maximum with respect to the lagrangian multiplier  $\lambda$ .

**Acknowledgments:** The financial support of this work provided by grants No.GACR 103/07/0304 and CZE MSM 684 077 0001,3 of the Grant Agency of the Czech Republic is gratefully acknowledged.

## References

- [1] Seguchi, Y. and Tada, Y., "Shape Determination of Structure Based on the Inverse Variational Principle, the Finite Element Approach", Proc. of International Symposium on Optimal Shape Design, University of Arizona, 1981
- [2] Tada, Y., Seguchi, Y. and Soh, T., "Shape Determination Problems of Structures by the Inverse Variational Principle", Feasibility Study about Application to Actual Structures. Bulletin of JSME, 29, 253, July 1986
- [3] Gao, Y., "Inverse variational principle in finite elasticity", Mechanics Research Communications, Volume 15, Issue 3, 161-166, 1988
- [4] Prochazka, P., "Shape optimal design using Inverse Variational Principles", submitted to EABE
- [5] Suquet P.M., "Elements of homogenization for inelastic solid mechanics", Lecture Notes in Physics, 272 - Homogenization Technique for Composite Media, 1987
- [6] Banerjee, P.K. and Butterfield, R., "Boundary Element Methods in Engineering Science", McGraw-Hill, London, New York, 1981

## Error reduction strategy in the analysis via SGBEM

Panzeca T., Milana V. and Salerno M.

Diseg Viale delle Scienze, 90128 Palermo, Italy,

tpanzeca@tiscali.it, archemilana@libero.it, mgsalerno@tiscali.it

**Keywords:** Symmetric Boundary Element Method, Galerkin residuals, meshes optimization.

**Abstract.** The Symmetric Galerkin Boundary Element Method (SGBEM) is assuming an always more effective rule in the solution of the mechanics problems in different fields of engineering. Its main characteristics consist in the high performance of the response because of use of the input easiness and of the boundary discretization adaptability. A wide bibliography, drawn up in the field of the structural mechanics, is quoted in a paper of Bonnet, Maier and Polizzotto [1].

The paper has as objective the estimation of the error in the structural analysis performed by using the mixed approach of the SGBEM and suggests a strategy able to reduce this error through an appropriate change of the boundary discretization.

### 1 Introduction

There were several researches who have dealt with the evaluation of the errors and the consequent techniques of discretization adaptability in the BEM [2-3]. In the collocation approach, Paulino et al. [4] suggest a technique of the error check based on the combination of the singular and hypersingular integral equations; after finding the approximate solution by using a typology of boundary integral equation, they obtain an error estimation of residual type by substituting the approximate solution into the remaining integral equation. In the analysis via SGBEM, Paulino and Gray [5] assert that it is necessary to obtain the solution by using both the typologies of the boundary equation; after, by substituting the approximate solution into the alternate equations in the energetic sense is possible to improve the structural response. This approach contemplates the introduction of the Galerkin Residuals and their use as local and global error estimation involves an adaptive mesh refinement strategy.

In the present paper the solid of domain  $\Omega$  and boundary  $\Gamma^-$ , is thought as embedded in a complementary domain  $\Omega_\infty \setminus \Omega$  of boundary  $\Gamma^+$ . The strain energy computed in  $\Omega$  and in  $\Omega_\infty \setminus \Omega$  is proved numerically equivalent to the work  $L_\Omega$  along  $\Gamma^-$  and  $L_{\Omega_\infty \setminus \Omega}$  along  $\Gamma^+$ , computed as generalized works and obtained as product among nodal and weighed quantities. The ratio between the generalized work  $L_{\Omega_\infty \setminus \Omega}$  and the total generalized work  $L_{\Omega_\infty} = L_\Omega + L_{\Omega_\infty \setminus \Omega}$  allows to obtain an indication regarding the level of the response goodness, therefore represents the error. The generalized work  $L_{\Omega_\infty \setminus \Omega}$ , which represents the scattered energy, must be computed at every boundary element of  $\Gamma^+$ . In order to reduce the entity of such energy, one or more nodes are introduced in the boundary element where it has the greatest values. Subsequent analyses and checks of the error, made in a recursive way, allow to obtain solutions which are closer to the actual one.

### 2 Mixed-value analysis via SGBEM

Embedding the real solid  $\Omega$  into a boundless domain  $\Omega_\infty$ , the quantities that characterize the whole boundary are redefined as layered forces and relative displacements:

$$\mathbf{f}(\mathbf{x}) = -\mathbf{t}_1^+(\mathbf{x}, \mathbf{n}) + \mathbf{t}_1^-(\mathbf{x}, \mathbf{n}); \quad \mathbf{v}(\mathbf{x}) = \mathbf{u}_2^+(\mathbf{x}) - \mathbf{u}_2^-(\mathbf{x}) \quad \text{on } \Gamma_1 \cup \Gamma_2 \quad (1a,b)$$

The following punctual relations written on the boundary of the complementary domain  $\Omega_\infty \setminus \Omega$

$$\mathbf{u}^+ = \mathbf{0}, \quad \mathbf{t}^+ = \mathbf{0} \quad \text{on} \quad \Gamma_1^+ \cup \Gamma_2^+ \quad (2a,b)$$

regarding the displacements and the tractions, represent the more restrictive conditions whose imply the presence of the strain and stress state only in the solid  $\Omega$ .

Let us introduce an appropriate boundary discretization and the weighting second Galerkin of the known and unknown modelled quantities. In order to obtain the equations system via mixed-value symmetric BEM, the punctual relationships (2a,b), written for the whole boundary, take on the following generalized form:

$$\mathbf{W}^+ = \int_{\Gamma^+} \Psi_1^T \mathbf{u}^+ d\Gamma^+ = \mathbf{0}, \quad \mathbf{P}^+ = \int_{\Gamma^+} \Psi_2^T \mathbf{t}^+ d\Gamma^+ = \mathbf{0} \quad (3a,b)$$

where Somigliana's Identities are utilized into eqs.(3a,b). According to the strategy introduced in [6], taking into account of the different typology of the boundary, constrained  $\Gamma_1^+$  and free  $\Gamma_2^+$ , in the hypothesis of domain load absence, we may write the following generalized equations

$$\begin{bmatrix} \mathbf{W}_2^+ \\ \mathbf{W}_1^+ \\ \mathbf{P}_2^+ \\ \mathbf{P}_1^+ \end{bmatrix} = \begin{bmatrix} \mathbf{B}_{u2u2} & \mathbf{B}_{u2u1} & \mathbf{B}_{u2t2} & \mathbf{B}_{u2t1} \\ \mathbf{B}_{u1u2} & \mathbf{B}_{u1u1} & \mathbf{B}_{u1t2} & \mathbf{B}_{u1t1} \\ \mathbf{B}_{t2u2} & \mathbf{B}_{t2u1} & \mathbf{B}_{t2t2} & \mathbf{B}_{t2t1} \\ \mathbf{B}_{t1u2} & \mathbf{B}_{t1u1} & \mathbf{B}_{t1t2} & \mathbf{B}_{t1t1} \end{bmatrix} \begin{bmatrix} \bar{\mathbf{F}}_2 \\ \mathbf{F}_1 \\ -\mathbf{U}_2 \\ -\bar{\mathbf{U}}_1 \end{bmatrix} = \begin{bmatrix} \mathbf{0} \\ \mathbf{0} \\ \mathbf{0} \\ \mathbf{0} \end{bmatrix} \quad (4)$$

where the quantities known ( $\bar{\mathbf{F}}_2, -\bar{\mathbf{U}}_1$ ) and unknown ( $\mathbf{F}_1, -\mathbf{U}_2$ ) are evaluated at the boundary  $\Gamma^-$ . The matrix of the coefficient  $\mathbf{B}$  is the following:

$$\mathbf{B} = \begin{bmatrix} \mathbf{A}_{u2u2} & \mathbf{A}_{u2u1} & \mathbf{A}_{u2t2} & \mathbf{A}_{u2t1} \\ \mathbf{A}_{u1u2} & \mathbf{A}_{u1u1} & \mathbf{A}_{u1t2} & \mathbf{A}_{u1t1} \\ \mathbf{A}_{t2u2} & \mathbf{A}_{t2u1} & \mathbf{A}_{t2t2} & \mathbf{A}_{t2t1} \\ \mathbf{A}_{t1u2} & \mathbf{A}_{t1u1} & \mathbf{A}_{t1t2} & \mathbf{A}_{t1t1} \end{bmatrix} + \begin{bmatrix} \mathbf{0} & \mathbf{0} & 1/2 \cdot \mathbf{C}_{u2t2} & \mathbf{0} \\ \mathbf{0} & \mathbf{0} & \mathbf{0} & 1/2 \cdot \mathbf{C}_{u1t1} \\ -1/2 \cdot \mathbf{C}_{t2u2} & \mathbf{0} & \mathbf{0} & \mathbf{0} \\ \mathbf{0} & -1/2 \cdot \mathbf{C}_{t1u1} & \mathbf{0} & \mathbf{0} \end{bmatrix} \quad (5)$$

The generalized Dirichlet and Neumann conditions  $\mathbf{W}_1^+ = \mathbf{0}$  and  $\mathbf{P}_2^+ = \mathbf{0}$  deduced by the second and third line of the precedent system (4), leads to the following equation system

$$\mathbf{K} \mathbf{X} + \mathbf{H} \bar{\mathbf{Y}} = \mathbf{0} \quad (6)$$

where

$$\mathbf{K} = \begin{bmatrix} \mathbf{B}_{u1u1} & \mathbf{B}_{u1t2} \\ \mathbf{B}_{t2u1} & \mathbf{B}_{t2t1} \end{bmatrix}; \quad \mathbf{X} = \begin{bmatrix} \mathbf{F}_1 \\ -\mathbf{U}_2 \end{bmatrix}; \quad \mathbf{H} = \begin{bmatrix} \mathbf{B}_{u1u2} & \mathbf{B}_{u1t1} \\ \mathbf{B}_{t2u2} & \mathbf{B}_{t2t1} \end{bmatrix}; \quad \bar{\mathbf{Y}} = \begin{bmatrix} \bar{\mathbf{F}}_2 \\ -\bar{\mathbf{U}}_1 \end{bmatrix} \quad (7a-d)$$

Now we have to characterize the way according to which the error in phase of analysis can be calculated and to suggest a technique of the error reduction based on the boundary mesh refinement. This approach is founded on the computation of the strain energy, regarding whether that inside the body or that scattered outside the body. At this aim the other two equations of system (4), not employed in the phase analysis, will be considered.

### 3 Energetic balance in the unlimited domain

In the domain  $\Omega_\infty$  the classical relationship of the energetic balance is valid between the work  $L$  produced by the external forces and the potential energy  $U$  stored in the domain. The unlimited domain is subdivided in two sub domains, the first made by the examining body  $\Omega$ , the second by the complementary domain  $\Omega_\infty \setminus \Omega$ ; it can be written:

$$L = U \rightarrow L_c^+ + L_c^- = U_{(\Omega_\infty - \Omega)} + U_\Omega \quad (8)$$

The problem solution has to respect the eqs. (2a,b), it implicating that the complementary domain doesn't have to be stressed and strained. But such condition never is respected. If we introduce the distinction of the boundary in an originally constrained part  $\Gamma_1^-$  and in an originally free part  $\Gamma_2^-$ , the previous eq. (8) becomes in explicit form:

$$\frac{1}{2} \int_{\Gamma_2^-} (\mathbf{t}_2^-)^T \mathbf{u}_2^- d\Gamma_2^- + \frac{1}{2} \int_{\Gamma_1^-} (\mathbf{u}_1^-)^T \mathbf{t}_1^- d\Gamma_1^- - \frac{1}{2} \int_{\Gamma_2^+} (\mathbf{t}_2^+)^T \mathbf{u}_2^+ d\Gamma_2^+ - \frac{1}{2} \int_{\Gamma_1^+} (\mathbf{u}_1^+)^T \mathbf{t}_1^+ d\Gamma_1^+ = \frac{1}{2} \int_{\Omega_\infty} \boldsymbol{\sigma}^T \boldsymbol{\varepsilon} d\Omega_\infty \quad (9)$$

which may be divided in two equations, each being the energetic balance

- for the real sub domain

$$\frac{1}{2} \int_{\Gamma_2^-} (\mathbf{t}_2^-)^T \mathbf{u}_2^- d\Gamma_2^- + \frac{1}{2} \int_{\Gamma_1^-} (\mathbf{u}_1^-)^T \mathbf{t}_1^- d\Gamma_1^- = \frac{1}{2} \int_{\Omega} \boldsymbol{\sigma}^T \boldsymbol{\varepsilon} d\Omega \quad (10)$$

- for the complementary sub domain

$$-\frac{1}{2} \int_{\Gamma_2^+} (\mathbf{t}_2^+)^T \mathbf{u}_2^+ d\Gamma_2^+ - \frac{1}{2} \int_{\Gamma_1^+} (\mathbf{u}_1^+)^T \mathbf{t}_1^+ d\Gamma_1^+ = \frac{1}{2} \int_{(\Omega_\infty \setminus \Omega)} \boldsymbol{\sigma}^T \boldsymbol{\varepsilon} d(\Omega_\infty \setminus \Omega) \quad (11)$$

#### 4 Error evaluation and boundary discretization optimization

The vector  $\mathbf{X}$ , obtained by eq. (6), do not satisfy the first and fourth block equations of the system (4) rewritten below:

$$\begin{bmatrix} \mathbf{W}_2^+ \\ \mathbf{P}_1^+ \end{bmatrix} \equiv \begin{bmatrix} \mathbf{B}_{u2u2} & \mathbf{B}_{u2t1} \\ \mathbf{B}_{t1u2} & \mathbf{B}_{t1t1} \end{bmatrix} \begin{bmatrix} \bar{\mathbf{F}}_2 \\ -\bar{\mathbf{U}}_1 \end{bmatrix} + \begin{bmatrix} \mathbf{B}_{u2u1} & \mathbf{B}_{u2t2} \\ \mathbf{B}_{t1u1} & \mathbf{B}_{t1t2} \end{bmatrix} \begin{bmatrix} \mathbf{F}_1 \\ -\mathbf{U}_2 \end{bmatrix} \neq \begin{bmatrix} \mathbf{0} \\ \mathbf{0} \end{bmatrix} \quad (12)$$

These latter represent the generalized conditions written on the complementary boundary, dual of the generalized Dirichlet and Neumann conditions. Indeed, the first equation represents the generalized displacement vector  $\mathbf{W}_2^+$  valued on  $\Gamma_2^+$ , dual quantity of the generalized stresses  $\mathbf{P}_2^+$ , whereas the fourth one represents the generalized traction vector  $\mathbf{P}_1^+$  valued on  $\Gamma_1^+$ , dual quantity of the generalized displacements  $\mathbf{W}_1^+$ .

We will use the inequalities (12) to calculate the error that is made in the structural analysis and to characterize a strategy leading to a more appropriate discretization of the solid boundary to obtain a response that is closer to the actual solution.

Therefore, in order to satisfy the previous block equations (12), we make the hypothesis to consider the vector  $\bar{\mathbf{Y}}$  of the assigned nodal quantities  $\bar{\mathbf{F}}_2$  and  $(-\bar{\mathbf{U}}_1)$  as unknown and to substitute this vector by the vector  $\mathbf{Y}$  of the nodal forces  $\mathbf{T}_2^-$  and displacements  $(-\mathbf{U}_1^-)$  changed in sign, related to the effective boundaries  $\Gamma_2^-$  and  $\Gamma_1^-$  of the examining solid. The vector  $\mathbf{X}$  is assumed as collecting known quantities.

We impose that the vectors  $\mathbf{T}_2^-$  and  $(-\mathbf{U}_1^-)$  satisfy the following system

$$\begin{bmatrix} \mathbf{B}_{u2u2} & \mathbf{B}_{u2t1} \\ \mathbf{B}_{t1u2} & \mathbf{B}_{t1t1} \end{bmatrix} \begin{bmatrix} \mathbf{T}_2^- \\ -\mathbf{U}_1^- \end{bmatrix} + \begin{bmatrix} \mathbf{B}_{u2u1} & \mathbf{B}_{u2t2} \\ \mathbf{B}_{t1u1} & \mathbf{B}_{t1t2} \end{bmatrix} \begin{bmatrix} \mathbf{F}_1 \\ -\mathbf{U}_2 \end{bmatrix} = \begin{bmatrix} \mathbf{0} \\ \mathbf{0} \end{bmatrix} \quad (13)$$

which in compact form may be written in the following way

$$\mathbf{Z} \mathbf{Y} + \mathbf{H}^T \mathbf{X} = \mathbf{0} \quad (14)$$

with

$$\mathbf{Y} = \begin{bmatrix} \mathbf{T}_2^- \\ -\mathbf{U}_1^- \end{bmatrix}; \quad \mathbf{Z} = \begin{bmatrix} \mathbf{B}_{u2u2} & \mathbf{B}_{u2t1} \\ \mathbf{B}_{t1u2} & \mathbf{B}_{t1t1} \end{bmatrix}; \quad \mathbf{H}^T = \begin{bmatrix} \mathbf{B}_{u2u1} & \mathbf{B}_{u2t2} \\ \mathbf{B}_{t1u1} & \mathbf{B}_{t1t2} \end{bmatrix} \quad (15a-c)$$

Because the vector  $\mathbf{X}$  is known by the analysis through eq.(6), we can obtain:

$$\mathbf{Y} = -\mathbf{Z}^{-1} \mathbf{H}^T \mathbf{X} \quad (16)$$

Therefore we can find the corresponding quantities on the boundary  $\Gamma^+ = \Gamma_1^+ \cup \Gamma_2^+$ , through the definition introduced in eq. (1a,b) valid in the continuum field for the layered quantities, i.e.

$$\mathbf{T}_2^+ = -\bar{\mathbf{F}}_2 + \mathbf{T}_2^-, \quad \mathbf{U}_1^+ = -\bar{\mathbf{U}}_1 + \mathbf{U}_1^- \quad (17a,b)$$

As a conclusion of such considerations, it can be observed that the components of the force vector  $\bar{\mathbf{F}}_2$  acting on the nodes of the examining solid are subdivided into a part  $\mathbf{T}_2^-$  really acting on the nodes of  $\Gamma_2^-$ , and into a residual part  $\mathbf{T}_2^+$  acting on the corresponding nodes of the complementary boundary  $\Gamma_2^+$ . And so also, the components of the displacement vector  $(-\bar{\mathbf{U}}_1)$ , changed in sign, imposed on the nodes of the examining solid are subdivided into a displacement vector  $\mathbf{U}_1^-$  interesting the nodes of  $\Gamma_1^-$  and into a displacement vector  $\mathbf{U}_1^+$  regarding the corresponding nodes of the boundary complementary  $\Gamma_1^+$ . Such a strategy permits to give an evaluation whether of the energy stored inside the domain  $\Omega$ , or of the energy scattered in the complementary domain  $\Omega_\infty \setminus \Omega$ .

#### 4.1 Energy valuated in the domain $\Omega$

Let us use the following modelling of the kinematical and mechanical quantities,

$$\mathbf{u}_1^-(\mathbf{x}) = \Psi_u \mathbf{U}_1^-, \quad \mathbf{t}_1^-(\mathbf{x}) = \Psi_t \mathbf{T}_2^- \quad (18a,b)$$

In order to express the energetic balance regarding the domain  $\Omega$  in terms of generalized quantities, let us introduce this modelling in the eq.(10), and evaluate the response  $\mathbf{u}_2^-$  e  $\mathbf{t}_1^-$  on  $\Gamma_2^-$  and  $\Gamma_1^-$  through the SIs. The energetic balance is reached for the examining real subdomain, in terms of quantities on  $\Gamma^-$

$$(\mathbf{T}_2^-)^T \mathbf{W}_2^- + (\mathbf{U}_1^-)^T \mathbf{P}_1^- = \int_{\Omega} \boldsymbol{\sigma}^T \boldsymbol{\varepsilon} d\Omega \quad (19)$$

In the latter expression two new vectors have been introduced, and precisely the generalized displacement vector  $\mathbf{W}_2^-$  calculated on  $\Gamma_2^-$  and the generalized traction vector  $\mathbf{P}_1^-$  calculated on  $\Gamma_1^-$ , expressed in the following form

$$\begin{aligned} \mathbf{W}_2^- &= \mathbf{A}_{u2u2} \bar{\mathbf{F}}_2 + \mathbf{A}_{u2u1} \mathbf{F}_1 + \mathbf{A}_{u2t2} (-\mathbf{U}_2) - \frac{1}{2} \mathbf{C}_{u2t2} (-\mathbf{U}_2) + \mathbf{A}_{u2t1} (-\bar{\mathbf{U}}_1) \\ \mathbf{P}_1^- &= \mathbf{A}_{t1u2} \bar{\mathbf{F}}_2 + \mathbf{A}_{t1u1} \mathbf{F}_1 + \frac{1}{2} \mathbf{C}_{t1u1} \mathbf{F}_1 + \mathbf{A}_{t1t2} (-\mathbf{U}_2) + \mathbf{A}_{t1t1} (-\bar{\mathbf{U}}_1) \end{aligned} \quad (20a,b)$$

#### 4.2 Energy valuated in the complementary domain $\Omega_\infty \setminus \Omega$

Let us use the following modelling of the kinematical and mechanical quantities,

$$\mathbf{t}_2^+(\mathbf{x}) = \Psi_t \mathbf{T}_2^+, \quad \mathbf{u}_1^+(\mathbf{x}) = \Psi_u \mathbf{U}_1^+ \quad (21)$$

In order to express the energetic balance regarding the complementary domain  $\Omega_\infty \setminus \Omega$  in terms of generalized quantities, let us introduce this modelling in eq.(11), and evaluate the response  $\mathbf{u}_2^+$  and  $\mathbf{t}_1^+$  on  $\Gamma_2^+$  and  $\Gamma_1^+$  through the SIs. The energetic balance is reached for the examining complementary domain, in terms of quantities on  $\Gamma^+$

$$L_{\Omega_\infty \setminus \Omega} \equiv -\frac{1}{2} (\mathbf{T}_2^+)^T \mathbf{W}_2^+ - \frac{1}{2} (\mathbf{U}_1^+)^T \mathbf{P}_1^+ = \frac{1}{2} \int_{(\Omega_\infty \setminus \Omega)} \boldsymbol{\sigma}^T \boldsymbol{\varepsilon} d(\Omega_\infty \setminus \Omega) \quad (22)$$

Two analogous relations may be written, analogously to the eqs.(20).

**4.3 Error percentage evaluation in the analysis**

The ratio between the generalized work  $L_{\Omega_e \setminus \Omega}$  on the boundary  $\Gamma^+$  and the total generalized work  $L_{\Omega_e}$  on the whole boundary  $\Gamma^- \cup \Gamma^+$  allows to individualize the error percentage globally made in the analysis:

$$\varepsilon\% = \frac{L_{\Omega_e \setminus \Omega}}{L_{\Omega_e}} = \frac{L_{\Omega_e \setminus \Omega}}{L_{\Omega} + L_{\Omega_e \setminus \Omega}} \tag{23}$$

The latter relationship, evaluated on every element of boundary, permits to individualize the elements where the lost energy is greater; i.e. the elements where the mesh must be thickened.

**5 Example**

Let us consider a structure having the geometry shown in Fig.1a and the thickness  $s = 30 \text{ cm}$ , constrained on the left and subjected to the constant load distribution  $q = 10 \text{ daN/cm}$  at the vertical side. The physical constants of the material are  $E = 200,000 \text{ daN/cm}^2$  and  $\nu = 0.2$ .

Through this example it was possible to verify that, when the load condition and the geometry give rise a stress concentration, particularly in the corners, the proposed approach involving the nodes increase based on the scattered energy in  $\Omega_e$  proves to be particularly advantageous respect to the case of a nodes increase performed with constant step.

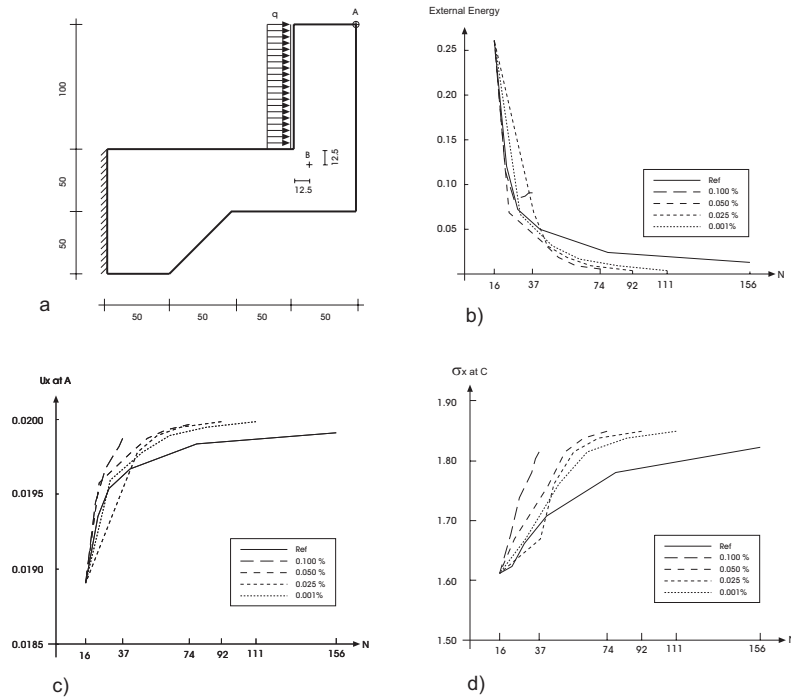


Fig. 1: a) Plate; b) scattered external energy, c) displacements at A, d) stresses  $\sigma_x$  at B.

The initial discretization foresees a distance among nodes each another about of 50 cm., it involving the presence of 16 nodes. In order to make the approach more effective, a procedure was inserted in the KARNAK SGBEM program [7].

In all the analyses the check was made by examining the values of the horizontal displacement of A and those of the stresses  $\sigma_x$  at the point B located at a distance of cm 12.5 from the corner, as it is shown in Fig.1a.

Besides, the external and inner energies, computed in terms of generalized quantities, were carried out in each analysis whether in the case of nodes increase with constant step or in the case of nodes increase based on the scattered generalized energy at  $\Gamma^+$ .

- Analysis performed with a nodes increase with constant step: this analysis was made providing a subdivision of the boundary with decreasing step, i.e. 40, 30, 20, 10, 5, and involving the employing of 23, 29, 41, 78, 156 nodes, distributed uniformly at the boundary.

- Analysis performed with a nodes increase based on the scattered energy in  $\Omega_\infty$  computed through the generalized energy at  $\Gamma^+$ : some analyses were made and a reference percentage value of the scattered generalized energy was fixed for each boundary element. When such reference energy percentage is exceeded, then a new node is inserted inside the examining boundary element. These percentage values were chosen equal to 0.1%, 0.05%, 0.025%, 0.001%. The results are shown in Fig. 1b, 1c, 1d

### Conclusions

In this paper a strategy to evaluate the error in the structural analysis performed by using the SGBEM is employed. After the embedding of the body into an infinite domain, a differentiated computation of the work, defined generalized, is obtained as the product among nodal and weighed quantities on the boundary of the inner and outer sub domains. This computation, made through boundary quantities, allows to obtain the error in percentage terms. When this error can not be neglected, it is possible to modify the boundary discretization by introducing some nodes in the boundary elements where the size of the generalized work is proved higher. Such a strategy, performed in a recursive way, has permitted to give a more appropriate boundary discretization in order to obtain solutions always closer to the actual solution by using a not excessive number of nodes.

### References

- [1] Bonnet, M.; Maier, G.; Polizzotto, C.: Symmetric Galerkin boundary element method. *Appl Mech Rev*, 51, 669-704, 1998.
- [2] Kita, E.; Namiya, N.: Error estimation and adaptative mesh refinement in boundary element method, an overview. *Eng Anal Bound Elem*, 25, 479-495, 2001.
- [3] Denda, M.; Dong, Y.F.: A unified formulation measure for the direct and indirect boundary element methods in elasticity. *Eng Anal Bound Elem*, 25, 557-564, 2001.
- [4] Paulino, G.H.; Gray, L.J.; Zarkian, V.: Hypersingular Residuals – A new approach for error estimation in the boundary element method. *Int J Numer Meth Engng*, 36, 2005-2009, 1996.
- [5] Paulino, G.H.; Gray, L.Y.: Galerkin Residuals for adaptive Symmetric-Galerkin Boundary Element Methods. *J Eng Mech*, 125, 575-585, 1999.
- [6] Terravecchia, S.: Analisi per sottostrutture nel Metodo Simmetrico degli Elementi di Contorno – Lastre. PhD Thesis; Cosenza, 2002.
- [7] Cucco, F.; Panzeca, T.; Terravecchia, S.: The program KARNAK SGBEM Release 1.0. Palermo, 2002. www. bemsoft.

## Damage identification by a BEM approach

V. Mallardo<sup>1</sup>, L. Nunziante<sup>2</sup>

<sup>1</sup> Dept. Architecture, University of Ferrara, via Quartieri 8, 44100 Ferrara, Italy, mlv@unife.it

<sup>2</sup> Dept. Structural Engineering, University of Naples "Federico II", via Claudio 21, 80125 Napoli, Italy, nunsci@unina.it

**Keywords:** Damage, identification, brittle, nonlocal.

**Abstract.** In the present paper the identification of the damage which may occur in the life of a brittle two-dimensional (2D) solid is examined by means of an inverse analysis. The damaged area is identified by minimising the error between numerical results and experimental results of some static load tests. Some design variables are introduced in order to describe the shape of the damaged area and the value of the damage in some key points.

### Introduction

Structural elements made of quasi-brittle materials as concrete may exhibit degradation of their elastic properties, and, eventually, a reduction of strength and stiffness after a certain threshold of stress or strain is reached. Materials presenting this kind of behavior are said to be of damaging type. The degradation of the mechanical properties is mainly related to a diffused micro-cracking. Such a micro-cracking is a typical failure phenomenon in quasi-brittle materials; it allows the limited ductility which is observed in the experimental tests.

A methodology to identify damage in quasi-brittle solids is presented in this paper. The method couples the damage models with the inverse analysis. The procedure is based on some experimental and numerical tests. The numerical response is obtained by using the integral equations. The main advantage of such a choice is related to the possibility to limit the mesh to the external boundary and to the part of domain where the damage is supposed to have occurred.

It is needless to emphasize the importance of damage detection technique and health monitoring in aerospace, civil and mechanical engineering. The question is even complicated if brittle materials are considered; this is due to the lack of a complete and successful methodology which is capable to correctly describe the nonlinear behaviour of brittle materials. At the moment the continuum models which have been proposed in the scientific literature requires some regularisation techniques in order to prevent unrealistic numerical results. The nonlocal approach of integral type is an example of such techniques.

To date, numerous nondestructive damage detection methods have been proposed and developed using various experimental and theoretical techniques. Most studies of the damage detection use measured dynamic responses. In this paper the problem is formulated as an optimisation problem where static measurements of displacements at few degrees of freedom are used to detect and identify the damage in the structure. The error between experimental results and numerical results is used to build the objective function to be minimised. One of the advantage of using static responses rather than dynamic ones is the higher sensitivity [1].

The numerical procedure is based on the assumption that the brittle behaviour of the solid can be represented by a continuum damage model. Such a model has demonstrated to be an efficient tool to represent correctly the initiation and propagation of micro-cracking. The micro-cracking which has possibly arisen in a previous load history is modelled by means of a scalar parameter  $d$ . Such a parameter, in the range 0-1 (1 means completely damaged), furnishes a representation of the micro-cracking by the deterioration of the mechanical properties, i.e. Young's modulus and Poisson's coefficient. The area which is affected by the damage and the distribution of  $d$  inside such an area can be represented by some design variables. On the basis of the knowledge of the response under some static loads it is possible to build an error function to be minimised. Such a function measures the difference between experimental and numerical results. The numerical response is obtained by applying an approach based on the integral

equations [2]. The main advantage of such an approach is the possibility to limit the mesh to the external boundary and to the part of the domain involved by the damage, i.e. the remeshing effort is reduced enormously if compared to the finite element (FE) approach.

The advantage of the adopted continuum damage model is in the limited number of material parameters which are involved, i.e. the Young's modulus and the Poisson's coefficient only. In [3] an inverse analysis to determine the intrinsic material properties involved in a gradient-enhanced continuum damage model is proposed. The resulting procedure turns out to be difficult to handle due to the high number of intrinsic parameters. In [4], the authors show that a single load displacement curve is not enough to identify the three parameters involved in a nonlocal isotropic damage model.

It must be pointed out that the proposed identification procedure is based on the assumption that some experimental static load tests are carried out in the elastic range. The response in terms of displacements is measured on the boundary and it is supposed that such values are influenced by the presence of the damage inside. Numerical experiments will be devoted to measure the capacity of such an influence to correctly lead the proposed identification procedure to the actual size and shape of the damaged zone.

### Identification as an optimisation problem

One can summarise the present non-destructive damage detection procedure by four main steps: static load testing, representation of the damaged region by design variables, building of the error function, identification as optimisation procedure.

The experimental tests are performed in the hypothesis not to increase the pre-existing damage either in size or in value. The response of the solid to the static load must remain in the elastic range. The existing damaged zone influences the global response, but it is not modified by the applied load.

The identification method here proposed is based on measurements (displacements) taken at NS sensor points on the external boundary of the solid and for D load conditions. The inverse process is iterative and two-fold. It consists of iterative solution of the direct plus non-linear mathematical minimisation method. The damaged area is described by some shape and damage parameters referred to as design variables. The identification process initially starts from an assumed shape and location of the damaged area and from an assumed distribution of the damage parameter inside the area. By using the Boundary Element Method (BEM), the displacement at the sensor points is evaluated and the resulting error function, with its gradient, is computed. The final values of the design variables are determined in order to minimise such an error.

Let  $\mathbf{X}_i$  be the  $i^{\text{th}}$  sensor node. The measured result at this point for the  $d^{\text{th}}$  loading condition is  $\mathbf{u}_d^0(\mathbf{X}_i)$  and the computed value for a set  $\mathbf{Z}^k$  of design variables (iteration k) is  $\mathbf{u}_d^k(\mathbf{X}_i)$ . The error function is given by:

$$f(\mathbf{Z}) = \frac{1}{D * NS} \sqrt{\sum_{d=1}^D \sum_{i=1}^{NS} \left\| \mathbf{u}_d^k(\mathbf{X}_i) - \mathbf{u}_d^0(\mathbf{X}_i) \right\|^2} \quad (1)$$

The minimisation process is carried out by the Quasi-Newton method where the gradient of the error function is evaluated by the finite difference method.

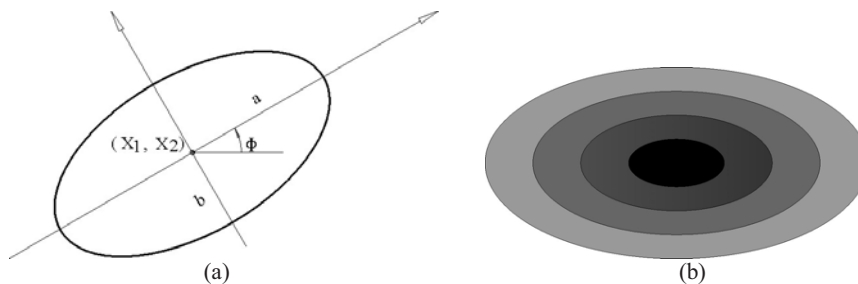


Figure 1. (a) Assumed shape of the damaged area. (b) Assumed distribution of damage.

To find the best representation of the damaged area with the minimum number of parameters is not a simple task. The higher the number DV of design variables is, the most difficult the minimisation process becomes. In this paper the damaged area is described by an ellipse, i.e. by the co-ordinates of the centre  $X_1, X_2$ , the axes  $a$  and  $b$  and the angle  $\Phi$  between the major axis and a reference axis  $x_1$  (see Fig. 1a). The distribution of the damage parameter  $d$  is assumed as in Fig. 1b. In every region with the same color the damage is supposed constant. The number (DV-5) of strips is chosen in terms of the problem under analysis. The assumed distribution should be able to capture the damage which most usually occurs; in fact, the micro-cracking initiates in a very small zone and it spreads in elliptical arches.

The assumed choice of the design variables may lead to implementation difficulties when the damaged area intersects the boundary of the solid. An example is illustrated in Fig. 2. An effective algorithm must be developed in order to handle with such a situation. The region to subtract can be determined by spanning the elliptic area with the dotted lines of Fig. 2 and checking if there is intersection with the external boundary. Where such an intersection occurs, some cells of the discretisation must be eliminated.

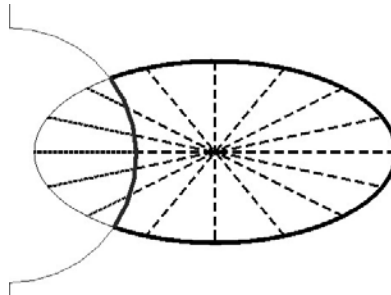


Figure 2. Handling the boundaries. The bold line surrounds the part of the damaged area to be considered.

The algorithm is similar to the one proposed in [5] in the  $h$ - $p$  cloud method context.

The evaluation of the design sensitivities, i.e. of the error function gradient, is straight if the ellipse is entirely contained in the solid. In the case of Fig. 2, such an evaluation is more complicated. A question of existence of the derivative arises if the ellipse approaches the external boundary. It can be demonstrated that the derivatives of the error function with respect to the design variables are continuous almost everywhere.

An implicit differentiation, as presented for instance in [6], may be implemented. It turns out to be mathematically straight provided that the damaged area is entirely contained in the domain, but it becomes difficult to develop in a different situation, i.e. a finite difference approach has to be implemented.

**The direct problem**

In this section the direct problem of the evaluation of the displacement field on the boundary in a 2D solid containing a damaged area is presented. Such a calculation is required at every step of the identification procedure. The basic hypothesis is that the damage occurred in the solid under analysis can be described by an isotropic damage model:

$$\sigma = (1-d)\mathbf{C}^{el} : \varepsilon \tag{2}$$

The mechanical properties, collected in the elastic stiffness matrix of the virgin material  $\mathbf{C}^{el}$ , are deteriorated by the damage parameter  $d$  which varies from 0 to 1 (1 is equivalent to completely damaged). The governing integral equation can be obtained by following an approach which is equivalent to plasticity. The resulting displacement integral equation, in absence of body force, has the following expression:

$$c_{ij}(\xi)u_j(\xi) + \int_{\Gamma} t_{ij}^*(\xi, \mathbf{x})u_j(\mathbf{x})d\Gamma(\mathbf{x}) = \int_{\Gamma} u_{ij}^*(\xi, \mathbf{x})t_j(\mathbf{x})d\Gamma(\mathbf{x}) + \int_{V_d} \varepsilon_{ijk}^*(\xi, \mathbf{x})\sigma_{jk}^d(\mathbf{x})dV_d(\mathbf{x}) \tag{3}$$

The curve  $\Gamma$  is the boundary of the solid with volume  $V$ . The damage is considered equivalent to an inelastic strain field in the part  $V_d$  of the entire body  $V \supset V_d$ . In fact, the total strain can be decomposed:

$$\varepsilon = \varepsilon^{el} + \varepsilon^d = \varepsilon^{el} + d\varepsilon \quad (4)$$

where the strain field  $\varepsilon^{el}$  is responsible of the actual stress. The tensor  $\sigma^d$  involved in the domain integral of eq (3) can be written as:

$$\sigma = \mathbf{C}^{el} : \varepsilon - d\mathbf{C}^{el} : \varepsilon = \sigma^{el} - \sigma^d \quad (5)$$

The fundamental solutions  $u_{ij}^*$ ,  $t_{ij}^*$ ,  $\varepsilon_{ijk}^*$  can be found in any BEM book (see for instance [7]),  $\xi$  and  $\mathbf{x}$  are usually referred as source and field point respectively and  $\mathbf{u}, \mathbf{t}$  are, respectively, displacement and traction fields on the boundary.

It can be noted that the integral equation (3) is not in rate form. This is due to the fact that the response under the applied load is supposed to be elastic, i.e. the damaged area does not change in size, shape and distribution of the damage parameter. The expression of the stress in any point is not necessary as the behaviour is supposed to be purely elastic. Differently from plasticity, no residual stresses are present. In fact, the isotropic damage model is characterised by zero residual strains at the end of the unload.

In order to obtain the numerical solution of the direct problem it is necessary to discretise both the external boundary  $\Gamma$  and the part  $V_d$  of the domain in which the damage is expected to have occurred in the previous load histories. The boundary is discretised in continuous quadratic isoparametric elements and the domain  $V_d$  is discretised in quadratic quadrilateral/triangular cells. By applying the boundary conditions and the collocation technique, the eq (3) can be re-written as:

$$\mathbf{A} \mathbf{x} = \mathbf{f} + \mathbf{Q} \sigma^d \quad (6)$$

The eq (6) is used at any step of the identification procedure to determine the numerical response for a given set of design variables.

### Summary

An identification procedure to estimate the damage in quasi-brittle solids has been proposed. The damage is described by a scalar parameter  $d$  on an elliptic area. The solid is supposed to be loaded by new load conditions in the elastic range. An error function which is a measure of the difference between the experimental and the numerical responses is built. Its minimisation furnishes the exact position and shape of the damaged area and a coarse distribution of the damage parameter inside it.

Numerical analyses are still in progress. The possibility to identify more than one damaged zone is also under investigation.

### References

- [1] J. Chou, J. Ghaboussi, *Computer and Structures*, **79**, 1335-1353 (2001).
- [2] V. Mallardo, *Computer Modelling in Engineering & Sciences*, submitted (2006).
- [3] C. Iacono, L.J. Sluys, J.G.M. van Mier, *Comp. Meth. Applied Mech. Eng.*, **195**, 7211-7222 (2006).
- [4] C. Le Bellégo, J.F. Dubé, G. Pijaudier-Cabot, B. Gérard, *Eu. J. Mech. A/Solids*, **22**, 33-46 (2003).
- [5] C. A. Duarte, J.T. Oden, *Comp. Meth. Applied Mech. Eng.*, **139**, 237-262 (1996).
- [6] V. Mallardo, M.H. Aliabadi, *Int J Num Meth Engng*, **41**, 1527-1541 (1998)
- [7] M.H. Aliabadi *The Boundary Element Method, Vol2: Applications in Solids and Structures*, Wiley (2002).

## High Order Velocities' Estimate for Flapping Foil

Marco La Mantia<sup>1</sup> and Peter Dabnichki<sup>2</sup>

<sup>1</sup> Department of Engineering, Queen Mary, University of London,  
327 Mile End Road, London, E1 4NS, United Kingdom, m.lamantia@qmul.ac.uk

<sup>2</sup> Department of Engineering, Queen Mary, University of London,  
327 Mile End Road, London, E1 4NS, United Kingdom, p.dabnichki@qmul.ac.uk

**Keywords:** panel method, flow potential function, flapping foil.

**Abstract.** The accurate estimate of the thrust produced by a flapping wing is central to the design of such propulsion system. The procedure for obtaining the velocities' distribution over the oscillating wing is essential for achieving a high precision of the forces' estimate. A computer program based on an unsteady potential flow panel method calculating the forces acting on a harmonically heaving and pitching two-dimensional rigid foil is presented. A number of different interpolations (linear, parabolic and cubic) and approximations (cubic and 5<sup>th</sup> order) of the flow potential function are analyzed. The computational results are significantly dependent on the velocities' estimate especially around the foil's edges, where the potential function behaviour is less smooth.

### Introduction

The observations of the swimming and flying behaviour of fish and birds encouraged the idea of utilizing the thrust generated by flapping wings for the propulsion of man-made objects. A number of theoretical and experimental studies were performed over the past few decades: e.g. see the review papers of Rozhdestvensky and Ryzhov [1] and Triantafyllou et al. [2]. The complex and multi-disciplinary character of the problem was underlined and key areas of interest identified, e.g. the effects of flow unsteadiness, wing flexibility and three-dimensionality. In any case, these issues have not been adequately investigated. Moreover, there are not any published studies on biomimetic vehicles capable of both flying and submerging in water, i.e. machines able to fly in water. For example, the possible technology exploitation of the penguins' swimming behaviour appears especially convenient for the development of a vehicle flying in water or another medium denser than air, e.g. an atmosphere denser than the terrestrial one.

The paper is part of a wider investigation of biomimetic systems that focuses on a theoretical and computational analysis of a feasible design for a hybrid wing, i.e. for the flexible and flapping wing of a machine that could fly and submerge in water. A potential flow based panel method computer program was developed to evaluate the forces produced by the unsteady motion of a two-dimensional rigid foil. The forces and the velocities' squares can be considered approximately proportional and here a number of numerical procedures for the evaluation of the velocities' distribution over the foil are analyzed. Besides, it seems that a similar computational issue was not previously studied in the literature.

### Kinematic Model and Unsteady Panel Method

An unsteady panel method code was devised to estimate the forces acting on a harmonically heaving and pitching two-dimensional rigid foil. A NACA 0012 symmetric foil of chord  $c$  is moving forward at an average, steady velocity  $Q_\infty$  and oscillating harmonically with a linear (heave) motion  $z(t)$  transversely to the velocity  $Q_\infty$  and with an angular (pitch) motion  $\gamma(t)$ , which is also the instantaneous angle between  $Q_\infty$  and the chord. The harmonic motions are both defined by the means of a sinusoidal law. The phase difference between the heaving and pitching motions  $\psi$  was set at 90 degrees, the heave amplitude  $z_0$  at three quarter of  $c$  and the pitch axis  $x_{pitch}$  at one third of the foil's chord. An important parameter of the motion is the Strouhal number  $St$  that is proportional to the maximum slope of the path and can be considered a measure of the degree of non-linearity of the motion. It indicates how often vortices are created in the foil's wake and how close they are: it is mathematically expressed by using the product of the frequency of vortex formation behind the foil (in Hz) and the width of the wake (assumed equal to two times the heave amplitude), divided by the flow main speed, i.e.

$$St = \frac{\omega}{2\pi} \frac{2z_0}{Q_\infty} = \frac{\omega z_0}{\pi Q_\infty}. \quad (1)$$

If  $Q_\infty$ ,  $z_0$  and  $St$  are fixed, it is then possible to compute the frequency of oscillation  $\omega$  (in radians per second). The instantaneous angle of attack is not explicitly related to the initial conditions. In general, for each Strouhal number  $St$ , when the maximum of the angle of attack  $\alpha_{max}$  is fixed, there are two possible pitch amplitudes, i.e. two possible angle of attack time paths: one corresponding to drag production and the other to thrust generation.

The most significant kinematic parameters used in the study are  $c=0.1$  m,  $x_{pitch}=0.033$  m,  $Q_\infty=0.4$  m/s,  $z_0=0.075$  m,  $St=0.3$ ,  $\psi=90$  deg,  $\alpha_{max}=15$  deg,  $\omega=5.027$  rad/s (0.8 Hz) and pitch amplitude  $\gamma_0=28.304$  deg (thrust generation).

According to [3], the flow is assumed inviscid, incompressible and irrotational and the foil is geometrically modelled by a finite number  $N$  of linear panels. A constant strength source  $\sigma$  and doublet (dipole)  $\mu$  are placed on each panel, whose midpoint is called the panel's collocation point. The flow potential function  $\phi^*$  at each collocation point is defined as the sum of a local (perturbation) potential  $\phi$ , related to the unknown doublet strength, and a free-stream potential  $\phi_\infty$ , linked to the kinematic flow velocity. An internal Dirichlet boundary condition is imposed, meaning that an inner potential function is specified on the internal foil's surface in order to meet the zero normal flow condition. At each foil's collocation point the source strength is known and related to the fluid's kinematic velocity due to the motion of the foil. The governing integral equation is derived by using the Laplace's equation and the Green's third identity. In the body-fixed coordinate system, at time  $t$  and for each foil's collocation point, it can be written as

$$\frac{1}{2\pi} \int_S [\sigma \ln r - \mu \frac{\partial}{\partial n} (\ln r)] dS - \frac{1}{2\pi} \int_{S_w} \mu_w \frac{\partial}{\partial n} (\ln r) dS_w = 0 \quad (2)$$

where  $S$  and  $S_w$  indicate the foil's and wake's surfaces, respectively,  $r$  is the distance between a generic panel and the respective foil's collocation point,  $n$  defines the direction normal to the surface and  $\mu_w$  is the strength of the wake doublet distribution. It is important to note that  $S_w$  changes with time: at each time step a new wake panel is added and its contribution evaluated. On each wake panel, which has an assigned length  $l_w$ , a constant strength doublet  $\mu_w$  is placed. Besides, the wake shape was properly estimated (the details of the wake modelling are here omitted). It is also important to note that the unknowns are  $N+1$  since at time  $t$  the doublet strengths of the previously shed wake panels are already derived. To identify uniquely the problem  $\mu_w$  needed to be related to the unknown doublets on  $S$  by the means of an appropriate Kutta condition. It is imposed at the trailing edge, at each time step, and is derived from the unsteady Bernoulli equation that, according to [4], can be written as

$$p_l + \frac{1}{2} \rho (q_l^2 - q_{kl}^2) + \rho \frac{\partial \phi_l^*}{\partial t} = p_u + \frac{1}{2} \rho (q_u^2 - q_{ku}^2) + \rho \frac{\partial \phi_u^*}{\partial t} \quad (3)$$

where the subscripts  $l$  and  $u$  indicate the lower and upper surface of the trailing edge, respectively. At these points, a number of variables are defined:  $p$  is the pressure,  $q$  the velocity,  $q_k$  the kinematic velocity due to the motion of the foil and  $\phi^*$  the potential function. The fluid velocity is the sum of  $q_k$  and the perturbation velocity, which is estimated by the means of the derivative of the perturbation potential over the foil, and  $\rho$  is the fluid's density, which is assumed constant and uniform.

The devised code can evaluate the flow potential function, at each time step. It is then possible to calculate the velocities' distribution over the foil in the body-fixed coordinate system linked to the foil. The subsequent calculation of the pressure coefficient is followed by the evaluation of the centre of pressure acceleration in the inertia frame of reference. This last one is later used for the forces' coefficients calculations. A time-averaged force is obtained before computing the coefficients: the mass of the wing needed to be assumed. A 0.6 m wing span  $s$  and a 300 kg/m<sup>3</sup> wing average density are chosen. The wing mass results then equal to roughly 0.15 kg. The water density  $\rho$ , set at 1000 kg/m<sup>3</sup>, is also used for the evaluation of the forces' coefficients.

According to [4], the pressure coefficient  $C_p$  at each foil's collocation point and time step is defined as

$$C_p = \frac{p - p_\infty}{\frac{1}{2} \rho Q_\infty^2} = \frac{q_k^2}{Q_\infty^2} - \frac{q^2}{Q_\infty^2} - \frac{2}{Q_\infty^2} \frac{\partial \phi^*}{\partial t}. \quad (4)$$

The thrust coefficient, which is the forces' coefficient in the direction of the inertia coordinate system parallel to  $Q_\infty$ , i.e. the  $x$  axis, is defined as

$$C_{Fx} = \frac{F_x}{\frac{1}{2} \rho c s Q_\infty^2} \quad (5)$$

where  $F_x$ , which is the time-averaged force in the  $x$  direction of the inertia frame of reference, is evaluated by using the respective acceleration of the centre of pressure. It is also important to note that the forces can be regarded as nearly proportional to the velocities' squares. An accurate estimate of the velocities' distribution over the oscillating foil is then essential for achieving a high precision of the forces' estimate.

### Velocities' Estimate

The fluid's velocity  $q$  at each foil's collocation point is the sum of the fluid velocity due to the motion of the foil  $q_k$  and the perturbation velocity  $q_p$ , which is estimated by the means of the derivative of the perturbation potential over the foil. As the unsteady Bernoulli equation also shown, a smooth behaviour of the potential function over the foil is required to obtain equally smooth velocity trend and avoid flow separation. In other words, sudden changes in the direction and magnitude of the fluid velocity can lead to a flow that is not going to generate on the foil lifting and propulsion forces.

The kinematical parameters of the foil motion are stated above and the number of foil's panels  $N$  was set at 100. The number of time steps is one hundred and eight, i.e. three complete oscillations and thirty six time steps for each loop were considered. Each time step lasts 0.035 s and 3.75 s is the entire duration of the harmonic foil motion.

Three different kind of interpolation were used: linear, parabolic (quadratic) and cubic. The values of the potential function in two, three and four consecutive collocation points of the foil are respectively employed to perform the interpolation and evaluate the flow velocity  $q$  in the considered collocation points. The estimated velocities are averaged by using the results of other interpolations, i.e.  $q$  is calculated taking also into account the velocity in the same position obtained by the interpolation of other sets of points. For example, in the case of the parabolic (quadratic) interpolation, which uses the local potential function values  $\varphi_j$  in three consecutive collocation points, e.g.  $i$ ,  $i+1$  and  $i+2$ , the following equations can be written

$$\varphi_j = a r_k^2 + b r_k + c \quad (6)$$

$$q'_{p,j} = 2 a r_k + b \quad (7)$$

where  $j=i,i+1,i+2$  and  $k=1,2,3$ , respectively.  $q'_{p,j}$  is the perturbation velocity at the considered collocation point. Moreover,  $r_k$  is evaluated by using the lengths of the involved foil's panels. By the means of the previous equations it is possible to estimate the velocities: there are three equations and three unknowns, i.e.  $a$ ,  $b$  and  $c$ . The components of the fluid velocity are calculated at each collocation points as

$$q'_x = q_{kx} + q'_p \cos \theta_j \quad (8)$$

$$q'_z = q_{kz} + q'_p \sin \theta_j \quad (9)$$

where  $\theta_j$  is the inclination of panel  $j$  in the body-fixed coordinate system whereas  $q_{kx}$  and  $q_{kz}$  are the components of  $q_k$  at  $j$ . Once  $q'$  is estimated the fluid velocity  $q$  at the point  $i+1$  is calculated taking into account also the velocity  $q''$  obtained by the interpolation of the following set of points. In other words, the components of  $q$  for the point  $i+1$  in the body-fixed frame of reference are estimated as the average of the respective components of  $q'$  and  $q''$ . Note that the flow velocities at the first and last collocation point are computed only once. The first collocation point is placed at the lower surface of the trailing edge and the last at the upper surface. The panels' numeration is clockwise, from the bottom of the trailing edge of the foil to the top. It is also important to note that, if one of the interpolation procedures is employed to estimate the velocities' distribution, the potential function behaviour does not change.

Two approximations of the local potential function (cubic and 5<sup>th</sup> order) were also considered to evaluate their influence on the velocities' estimate over the foil. The foil is divided into two parts. All the values of the local potential function of the lower (or upper) surface of the foil are employed to estimate a function that can approximate the potential function trend in the considered part of the foil. The approximated potential function is obtained by minimizing the sum of the squares of the differences between the actual (i.e. numerically evaluated) and approximated values in all the points of the considered surface. More generally, the following equations can be written

$$R^2 = \sum_{i=1}^n [y_i - (a_1 + a_2 r_i + a_3 r_i^2 + a_4 r_i^3 + \dots + a_m x_i^{m-1})]^2 \quad (10)$$

$$\frac{\partial R^2}{\partial a_j} = 0 \quad (11)$$

where  $n$  is the number of the involved consecutive collocation points and  $y(r_i)$  the actual function. By the means of Equation (11), a system of  $m$  linear equations ( $j=1, \dots, m$ ) is obtained and the  $m$  unknowns can be calculated. It is then possible to evaluate the function's  $r$ -derivative, i.e. in this case the velocities' distribution over the foil in the body-fixed frame of reference at each time step. Note that  $n$  can be equal to or larger than  $m$ . Besides,  $r_i$  is evaluated by using the lengths of the involved foil's panels. Once the linear system is solved the velocities can be estimated at each collocation point as

$$q_k = a_2 + 2 a_3 r_i + 3 a_4 r_i^2 + \dots + (m-1) a_m r_i^{m-2}. \quad (12)$$

In the case of the cubic approximation  $n=N/2$  and  $m=4$  whereas for the 5<sup>th</sup>-order approximation  $n=N/2$  and  $m=6$ . It is important to note that, if one of the approximation procedures is used to estimate the velocities' distribution, the potential function behaviour results approximate, i.e. the potential values employed for the velocities' estimate are not the same that were numerically evaluated.

In Figure 1, where  $\phi$  is plotted as a function of the collocation point position in the body-fixed coordinate system, at the first time step, it is possible to see how the two approximations affect the local potential function behaviour in the leading-edge region of the foil. It can be noted that the higher order approximation fits more closely the numerically evaluated potential function. However, the three trends look similar, i.e. the potential function trend appears to be smooth.

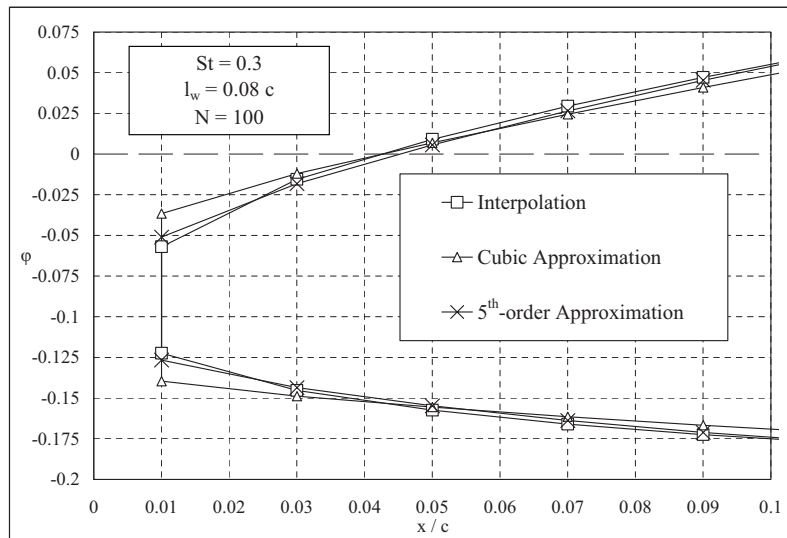


Figure 1. The local potential function is plotted as a function of the collocation point position in the body-fixed coordinate system, in the proximity of the foil's leading edge.

The pressure and thrust coefficients resulted to be affected by the velocities' estimate. Especially the pressure behaviour around the foil's edges, where the potential function trend is less smooth, depends on the procedure used to evaluate the velocities' distribution over the foil.

Table 1 shows the thrust coefficients and the maximum pressure coefficients, at the first time step, as a function of the interpolation or approximation procedure when  $N=100$ ,  $St=0.3$  and the length of the wake panel  $l_w=0.08 c$ . In the column on the right hand side the trailing-edge pressure difference is presented as a

percentage of the maximum pressure coefficient, which, at the first time step, is generally placed close to the leading edge. It is possible to note that the employed numerical procedure affects especially the value of the maximum pressure coefficient. The thrust coefficients seem to be less dependent on the velocities' estimate.

Table 1. The thrust and maximum pressure coefficients, at the first time step, are displayed as a function of the procedure used to evaluate the velocities' distribution over the foil. The number of foil's panel is 100,  $St=0.3$  and  $l_w=0.08 c$ . In the last column the trailing-edge pressure difference is presented as a percentage of the maximum pressure coefficient.

	$C_{Fx}$	$C_{p\ max}$	$\frac{C_{pl} - C_{pu}}{C_{p\ max}} 100$
Linear Interpolation	-0.449	-7.56	4.77
Parabolic Interpolation	-0.486	-10.49	4.75
Cubic Interpolation	-0.499	-12.37	4.61
Cubic Approximation	-0.345	-3.29	10.32
5 <sup>th</sup> -order Approximation	-0.391	-4.55	8.20

As an example, in Figures 2 and 3 the pressure coefficients at the first time step are shown in the trailing-edge region as a function of the numerical procedure employed to estimate the velocities' distribution over the foil.

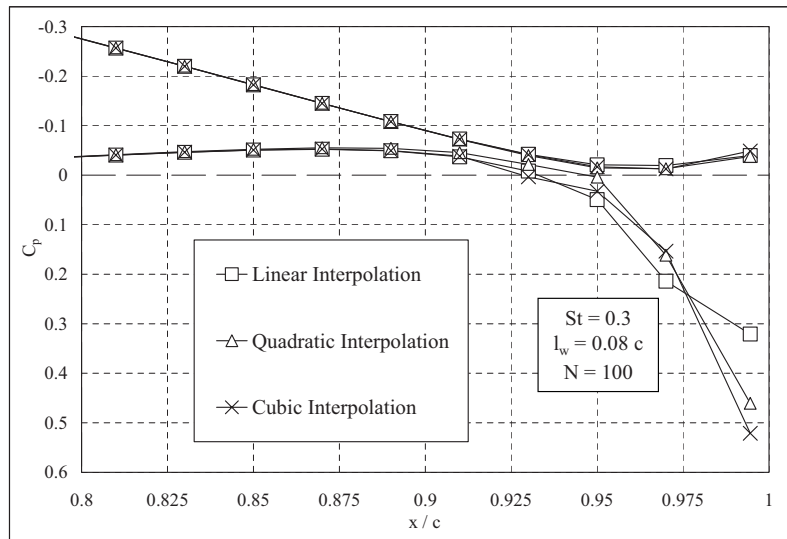


Figure 2. The pressure coefficients, at the first time step, are plotted in the trailing-edge region of the foil as a function of the interpolation procedure used to evaluate the velocities' distribution.

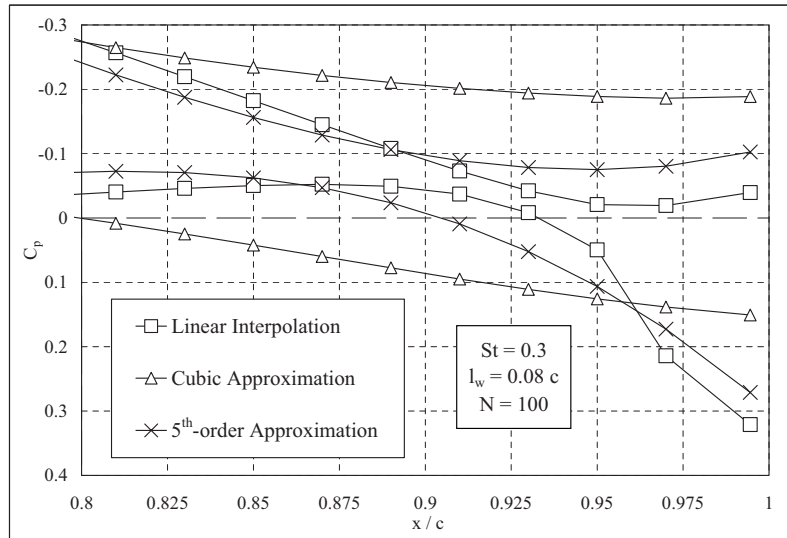


Figure 3. The pressure coefficients, at the first time step, are displayed in the trailing-edge region as a function of the procedure employed to estimate the velocities' distribution over the foil.

### Conclusions

A brief analysis of the numerical procedures employed to estimate the velocities' distribution over a harmonically heaving and pitching two-dimensional rigid foil has been presented. It was shown that the pressure behaviour around the foil's edges, where the potential function trend is less smooth, depends on the velocities' estimate. In other words, the procedure used to evaluate the derivative of the local potential function over the foil has a relevant influence on the thrust and pressure coefficients.

A number of other numerical issues, which were not presented here, have been identified. Those include the influence on the results of the foil and wake modelling and the centre of pressure estimate, which especially appears to be a relevant topic when the foil is moving in a medium denser than air. Besides, the specification of an appropriate Kutta condition seems to be one of the most important details of the numerical implementation.

The need of considering the differences between the actual flow conditions and the potential assumptions appears then an appropriate option to properly choose the mathematical model able to better represent the physical problem.

### References

- [1] K.V. Rozhdestvensky and V.A. Ryzhov, *Aerohydrodynamics of Flapping-Wing Propulsors*, *Progress in Aerospace Science*, 39 (8), 585-633 (2003).
- [2] M.S. Triantafyllou, A.H. Techet and F.S. Hover, *Review of Experimental Work in Biomimetic Foils*, *IEEE Journal of Oceanic Engineering*, 29 (3), 585-594 (2004).
- [3] J. Katz and A. Plotkin, *Low-Speed Aerodynamics – Second Edition*, Cambridge University Press (2001).
- [4] T. Cebeci, M. Platzer, H. Chen, K.-C. Chang and J.P. Shao, *Analysis of Low-Speed Unsteady Airfoil Flows*, Springer (2005).

**ELASTIC MODELLING OF FUNCTIONALLY GRADED MATERIALS  
HASHIN-SHTRIKMAN APPROACH**

Z.Sharif Khodaei<sup>1</sup>, J.Zeman<sup>2</sup> and P.Prochazka<sup>3</sup>

<sup>1</sup> Czech Technical University in Prague, Faculty of Civil Engineering, Department of Mechanics, Thákurova 7, 166 29  
Prague 6, Czech Republic,  
e-mail:Zahra.sharif@gmail.com

<sup>2</sup> Czech Technical University in Prague, Faculty of Civil Engineering, Department of Mechanics, Thákurova 7, 166 29  
Prague 6, Czech Republic  
e-mail:zemanj@cml.fsv.cvut.cz

<sup>3</sup> Czech Technical University in Prague, Faculty of Civil Engineering, Department of Mechanics, Thákurova 7, 166 29  
Prague 6, Czech Republic,  
e-mail:peter.proch@gmail.com

**Keywords:** Functionally graded materials, Statistically non-uniform composites, Microstructural model of fully penetrable spheres, Hashin-Shtrikman variational principles, Boundary element method

### 1. Introduction

Functionally graded materials (FGMs) are two-phase composites with continuously changing microstructure, which is adapted to performance requirements. Traditionally, the overall behavior of FGMs has been determined using local averaging techniques or a given smooth variation of material properties to estimate the material properties of the graded domain. Although these models are computationally efficient, their validity and accuracy remain questionable as their link with the underlying microstructure (including its randomness) is not clear. A brief, but hopefully representative enough, discussion on this subject is available e.g. in [7].

The goal of this work is to make the first step towards the formulation of a model which is free of the above mentioned limitations. The approach adopted in this work is systematically builds on the model of fully penetrable spheres introduced by Quintanilla and Torquato, [5], and is briefly reviewed in Section 2. The statistics of local fields then follow from re-formulation of the Hashin-Shtrikman variational principles introduced in [2] and in the current context summarized in Section 3. To allow for the analysis of finite bodies with arbitrary geometry, recently introduced discretization schemes are employed to obtain low-order statistics of local fields. To this end, in Section 4, we employ the Boundary Element method in the spirit of [4]. The theoretical formulations have been extended to the two-dimensional setting for this work; however for better understanding a simple one-dimensional example has been illustrated in Section 5. A more elaborate description of individual steps and a number of technical details can be found in diploma thesis, [6].

Throughout the paper the following notations have been used;  $a$ ,  $\mathbf{a}$ , and  $\mathbf{A}$  for a scalar quantity, vector and tensor notations, respectively. Other symbols are introduced in the text as needed.

### 2. Microstructural model

As already indicated in the introductory part, the microstructural model adopted in this work is basically the two-dimensional case of a microstructural model studied by Quintanilla and Torquato [5].

A particular realization can be depicted as a collection on  $N$  fully penetrable spheres (fibers in 2D) of radius  $R$  randomly distributed within a plate (matrix material) of size  $H_1 \times H_2$ , whose particle density obeys any specified variation in volume fraction, see Figure 1. The position of the  $i$ -th sphere is specified by the  $x$  and  $y$  coordinates of its reference point  $\mathbf{x}$  which in our case coincides with the center of the sphere. As individual spheres are allowed to freely overlap each other, the family of microstructures attainable by the model is very versatile.

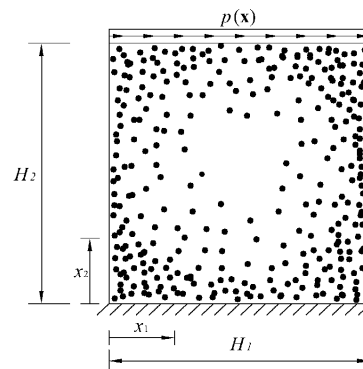


Figure 1. Example of microstructural model realization

To allow for microstructure gradation, the distribution of the reference points is specified using *position-dependent intensity*  $\rho(\mathbf{x})$  giving the expected number of reference points  $d\eta(\mathbf{x})$  found in an infinitesimal segment  $d\mathbf{x}$  around a point  $\mathbf{x}$ , by the product  $\rho(\mathbf{x})d\mathbf{x}$ . Using the theory of general Poisson processes, the probability that there will be exactly  $m$  points located in a finite-sized domain  $B$  is given as[5]

$$P_m(B) = \frac{|B|^m}{m!} \exp\left(-\int_B \rho(\mathbf{x})d\mathbf{x}\right), \quad (1)$$

where  $|B|$  simply denotes the area of  $B$ .

To provide a framework for the statistical characterization of the introduced microstructural model, we introduce a microstructural configuration  $\alpha$  (e.g. Figure 1), chosen from the set of all microstructural configuration denoted as  $\mathbf{S}$ , with the probability density  $\rho(\alpha)$ . Then, the ensemble average or the expected value of a random function  $f(\mathbf{x};\alpha)$  is defined as

$$\langle f(\mathbf{x}) \rangle := \int_{\mathbf{S}} f(\mathbf{x};\alpha) \cdot \rho(\alpha) d\alpha.$$

Now, if we interpret Figure 1 as “fiber” and “matrix” (black circles are fibers) phases, then for a given microstructural configuration  $\alpha$ , the distribution of phase  $r$  is described by a characteristic function  $\chi_r(\mathbf{x};\alpha)$  defined as,

$$\chi_r(\mathbf{x};\alpha) := \begin{cases} 1 & \text{if } \mathbf{x} \text{ is located in phase } r \\ 0 & \text{otherwise,} \end{cases} \quad (2)$$

where  $r = 1$  or  $2$  denote the matrix and fiber phases, respectively. The basic statistical characterization of the model is described by one-point probability function  $c_r(\mathbf{x})$

$$c_r(\mathbf{x}) = \langle \chi_r(\mathbf{x}) \rangle$$

which gives the probability of a point  $\mathbf{x}$  being in phase  $r$ . Evaluating Eq.(1), it gives

$$c_1(\mathbf{x}) = P_0(I(\mathbf{x})) = \exp\left(-\int_{I(\mathbf{x})} \rho(t)dt\right),$$

Where  $I(\mathbf{x})$  denotes a circle of radius  $R$  centered at  $\mathbf{x}$ .

The one-point probability  $c_2(\mathbf{x})$  follows from the identity

$$c_1(\mathbf{x}) + c_2(\mathbf{x}) = 1, \quad (3)$$

which follows directly from the definition of the characteristic function, i.e. Eq.(2). By analogy, we can define the two-point probability function  $S_{rs}$  and evaluate it for  $r = s = 1$  as

$$S_{rs}(\mathbf{x}, \mathbf{y}) := \langle \chi_r(\mathbf{x}) \chi_s(\mathbf{y}) \rangle, \quad S_{11}(\mathbf{x}, \mathbf{y}) = P_0(I(\mathbf{x}) \cup I(\mathbf{y})). \quad (4)$$

Recall that the previous function gives the probability that a point  $\mathbf{x}$  will be located in phase  $r$  while  $\mathbf{y}$  stays in the phase  $s$ . Remaining functions  $S_{rs}$  can be directly evaluated from  $S_{11}$  using relation similar to Eq.(3).; see [6] for more details.

### 3. Hashin-Shtrikman variational formulation

Consider now a two-dimensional elasticity problem for a structure consistent with a realization  $\alpha$  shown in Figure 1. Let us consider a bounded domain  $\Omega$  and closed boundary  $\Gamma$  with prescribed surface traction  $\mathbf{p}(\mathbf{x})$ . Assigning  $\mathbf{L}(\mathbf{x};\alpha)$ , stiffness matrix, to each point together with specifying boundary conditions and loading according to Figure 1 leads to the following problem: Find an unknown displacement field  $\mathbf{u}(\mathbf{x};\alpha) \in \mathbf{K}$ , such that for any test function  $\mathbf{v}(\mathbf{x}) \in \mathbf{K}$

$$\int_{\Omega} \boldsymbol{\varepsilon}(\mathbf{v}(\mathbf{x})) : \mathbf{L}(\mathbf{x};\alpha) : \boldsymbol{\varepsilon}(\mathbf{u}(\mathbf{x})) d\Omega = \int_{\Gamma_u} \mathbf{v}(\mathbf{x}) \cdot \mathbf{f}(\mathbf{x}) d\Gamma_u + \int_{\Gamma_p} \mathbf{v}(\mathbf{x}) \cdot \mathbf{p}(\mathbf{x}) d\Gamma_p \quad (5)$$

Referring to classical VP, Eq.(5) can be equivalently formulated as minimization problem of the energy functional  $\Pi$  in the form:

$$\mathbf{u}(\mathbf{x};\alpha) = \arg \min_{\mathbf{v}(\mathbf{x}) \in \mathbf{K}} \Pi(\mathbf{v}(\mathbf{x});\alpha) \quad (6)$$

Given a realization  $\alpha$ , Eq.(6) allows to define the “true” displacement field  $\mathbf{u}(\mathbf{x};\alpha)$ .

In order to estimate the statistics of the solution, the following averaged energy functional is introduced,

$$\langle \Pi(\mathbf{v}(\mathbf{x});\alpha) \rangle = \int_{\mathbf{S}} \Pi(\mathbf{v}(\mathbf{x});\alpha) \boldsymbol{\mu}(\alpha) d\alpha \quad (7)$$

and the corresponding minimization problem

$$\mathbf{u}(\mathbf{x};\alpha) = \arg \min_{\mathbf{v}(\mathbf{x},\alpha) \in \mathbf{K} \times \mathbf{S}} \langle \Pi(\mathbf{v}(\mathbf{x});\alpha) \rangle \quad (8)$$

In theory, the previous relation fully specifies the distribution displacement fields once the probability distribution  $\boldsymbol{\mu}(\alpha)$  is given. However, a full characterization of the set  $\mathbf{S}$  is rather complex and the probability distribution  $\boldsymbol{\mu}(\alpha)$  is generally not known. Hence, we need to base the solution on partial data such as the one- and two-point probability functions introduced in Section 2.

### 3.1. Hashin-Shtrikman variational principle

Following the classical assumptions of Hashin and Shtikman summarized in [8], we introduce a *reference structure*, which is identical to the original problem in loading and boundary conditions, but possesses a homogenous material data  $L_0$ . To account for the difference between these two bodies, polarization stress  $\tau(\mathbf{x}, \alpha)$  is introduced to ensure the stress equivalence.

$$\boldsymbol{\sigma}(\mathbf{x}; \alpha) = \mathbf{L}(\mathbf{x}; \alpha) : \boldsymbol{\varepsilon}(\mathbf{x}; \alpha) = \mathbf{L}_0 : \boldsymbol{\varepsilon}(\mathbf{x}; \alpha) + \boldsymbol{\tau}(\mathbf{x}; \alpha)$$

where  $\boldsymbol{\sigma}$  denotes the stress field and the polarization stress  $\boldsymbol{\tau}(\mathbf{x}; \alpha)$  becomes a new variable to be determined from the Hashin-Shtrikman functional

$$U(\mathbf{v}(\mathbf{x}), \boldsymbol{\theta}(\mathbf{x}; \alpha); \alpha) = \int_{\Omega} \left\{ \frac{1}{2} \boldsymbol{\varepsilon}(\mathbf{v}) : \mathbf{L}(\mathbf{x}; \alpha) : \boldsymbol{\varepsilon}(\mathbf{v}) + \boldsymbol{\theta}(\mathbf{x}; \alpha) : \boldsymbol{\varepsilon}(\mathbf{x}; \alpha) \right\} d\Omega - \int_{\Gamma_u} \mathbf{v}(\mathbf{x}) \cdot \mathbf{f}(\mathbf{x}) d\Gamma_u - \int_{\Gamma_p} \mathbf{v}(\mathbf{x}) \cdot \mathbf{p}(\mathbf{x}) d\Gamma_p + \int_{\Omega} \frac{1}{2} \boldsymbol{\theta}(\mathbf{x}; \alpha) : \mathbf{L}^{-1}(\mathbf{x}; \alpha) : \boldsymbol{\theta}(\mathbf{x}; \alpha) d\Omega \quad (9)$$

and assuming that  $L_0 \geq L_r$ , an equivalent "stochastic" variational problem can be cast in the form

$$U(\mathbf{u}(\mathbf{x}), \boldsymbol{\tau}(\mathbf{x}; \alpha), \alpha) = \min_{\boldsymbol{\theta}(\mathbf{x}; \alpha) \in F(\alpha)} \min_{\mathbf{v}(\mathbf{x}) \in K} U(\mathbf{v}(\mathbf{x}), \boldsymbol{\tau}(\mathbf{x}; \alpha); \alpha), \quad (10)$$

where  $F(\alpha)$  denotes the *configuration-dependent* set of admissible polarization stresses.

From the point of view of numerical treatment of the problem, we introduce the following split of displacement field

$$\mathbf{u}(\mathbf{x}; \alpha) = \mathbf{u}_0(\mathbf{x}) + \mathbf{u}_1(\mathbf{x}; \alpha) \quad (11)$$

where  $\mathbf{u}_0(\mathbf{x})$  is the displacement corresponding to the microstructure-independent *reference* part (a homogeneous structure subject to loading and non-homogeneous boundary conditions), which can be solved using any appropriate numerical approximation method; and  $\mathbf{u}_1(\mathbf{x}; \alpha)$  is the displacement from the microstructure-dependent *polarization* part, a problem without loading and with homogeneous boundary data loaded by a polarization stress  $\boldsymbol{\theta}(\mathbf{x}; \alpha)$ . The corresponding variational formulations are split into

$$\int_{\Omega} \boldsymbol{\varepsilon}(\mathbf{v}(\mathbf{x})) : \mathbf{L}_0 : \boldsymbol{\varepsilon}(\mathbf{u}_0(\mathbf{x})) d\Omega = \int_{\Gamma_u} \mathbf{v}(\mathbf{x}) \cdot \mathbf{f}(\mathbf{x}) d\Gamma_u + \int_{\Gamma_p} \mathbf{v}(\mathbf{x}) \cdot \mathbf{p}(\mathbf{x}) d\Gamma_p \quad (12)$$

where we consider  $\mathbf{u}^0$  to be a known function, therefore the above equation is a standard problem, and

$$\int_{\Omega} \boldsymbol{\varepsilon}(\mathbf{v}(\mathbf{x})) : \mathbf{L}_0 : \boldsymbol{\varepsilon}(\mathbf{u}_1(\mathbf{x}; \alpha)) d\Omega = - \int_{\Omega} \boldsymbol{\varepsilon}(\mathbf{v}(\mathbf{x})) : \boldsymbol{\theta}(\mathbf{x}; \alpha) d\Omega \quad (13)$$

which the solution of the Eq.(13) can be expected in the form

$$\boldsymbol{\varepsilon}(\mathbf{u}_1(\mathbf{x}; \alpha)) = - \int_{\Omega} \boldsymbol{\Gamma}_0(\mathbf{x}, \mathbf{y}) : \boldsymbol{\theta}(\mathbf{y}; \alpha) d\Omega. \quad (14)$$

where  $\boldsymbol{\Gamma}_0$  is a function related to the Green's function of a homogenous body with stiffness  $L_0$ , see, e.g., [6] for a detailed discussion.

This step completes the minimization with respect to  $\mathbf{v}$  in the Eq.(10). Consequently, we are left with minimizing with respect to the polarization stress  $\boldsymbol{\theta}(\mathbf{x}; \alpha)$

$$H(\boldsymbol{\tau}(\mathbf{x}; \alpha), \alpha) = \min_{\boldsymbol{\theta}(\mathbf{x}; \alpha) \in F(\alpha)} H(\boldsymbol{\theta}(\mathbf{x}; \alpha); \alpha) \quad (15)$$

where the "reduced" Hashin-Shtrikman functional is defined as

$$H(\boldsymbol{\theta}(\mathbf{x}; \alpha); \alpha) := U(\mathbf{u}(\boldsymbol{\theta}(\mathbf{x}; \alpha)), \boldsymbol{\theta}(\mathbf{x}; \alpha); \alpha), \quad (16)$$

Where  $\mathbf{u}(\boldsymbol{\theta}(\mathbf{x}; \alpha))$  is defined by Eq.(11), (12) and (14). From Eq.(16) and the fact that minimum of the Hashin-Shtrikman functional  $U$  coincides with the minimum of the energy functional  $\Pi$ , we can equate

$$\Pi(\mathbf{u}(\mathbf{x}; \alpha)) = H(\boldsymbol{\tau}(\mathbf{x}; \alpha))$$

where

$$\langle \boldsymbol{\theta}(\mathbf{x}; \alpha) \rangle = \int_{\mathcal{S}} H(\boldsymbol{\theta}(\mathbf{x}; \alpha); \alpha) \cdot \boldsymbol{\mu}(\alpha) d\alpha \quad (17)$$

Now we introduce the following form of the test stress polarization field

$$\boldsymbol{\theta}(\mathbf{x}; \alpha) = \sum_{r=1}^2 \chi_r(\mathbf{x}; \alpha) \boldsymbol{\theta}_r(\mathbf{x}) \quad (18)$$

where  $\boldsymbol{\theta}_r(\mathbf{x})$  are *realization-dependent* trial fields related to phase  $r$ . We get the probabilistic averaging of the Hashin-Shtrikman functional by plugging Eq.(18) into Eq.(17), solely in terms of field polarization stress  $\boldsymbol{\theta}_r(\mathbf{x})$ . For our last step, we perform maximization with respect to phase polarization field  $\boldsymbol{\theta}_r(\mathbf{x})$ , and the stationary condition of the approximated Hashin-Shtrikman variational principle attains the form:

$$\int_{\Omega} \boldsymbol{\theta}(\mathbf{x}) \cdot \mathbf{c}_r(\mathbf{x}) : [\mathbf{L}_r - \mathbf{L}_0]^{-1} : \boldsymbol{\tau}_r(\mathbf{x}) d\Omega + \sum_{s=1}^2 \int_{\Omega} \mathbf{S}_{rs}(\mathbf{x}, \mathbf{y}) : \boldsymbol{\Gamma}_0(\mathbf{x}, \mathbf{y}) : \boldsymbol{\tau}_s(\mathbf{y}) d\Omega = \int_{\Omega} \boldsymbol{\theta}(\mathbf{x}) \cdot \mathbf{c}_r(\mathbf{x}) : \boldsymbol{\varepsilon}(\mathbf{u}_0(\mathbf{x})) d\Omega. \quad (19)$$

The above equation still presents an infinite system of conditions to be fulfilled. Therefore, to reduce these conditions to a finite-dimensional problem, a proper discretization scheme needs to be set up. This topic is covered in the following section.

#### 4. Boundary element discretization

##### 4.1. Reference problem

According to the standard boundary element method [1], we start with the *fundamental solution*, which are attached to Dirac delta functions. Formulating the ordinary differential equation of the problem according to the boundary conditions, we apply twice *by-parts* integration and replace the test function  $\mathbf{v}(\mathbf{x})$  by Green's function. By applying the Betti theorem and after some manipulations discussed in [6], we arrive to systems of linear equations which by solving them we can formulate the expressions for  $\mathbf{u}_0(\mathbf{x})$  and  $\boldsymbol{\varepsilon}_0(\mathbf{x})$  and solve the first part of the problem.

##### 4.2. Polarization problem

Referring to discretized Hashin-Shtrikman principle [4], we employ the discretization of the polarization stresses as:

$$\boldsymbol{\tau}_r(\mathbf{x}) \approx \mathbf{N}^T(\mathbf{x}) \mathbf{d}_r^T, \quad \boldsymbol{\theta}_r(\mathbf{x}) \approx \mathbf{N}^T(\mathbf{x}) \mathbf{d}_r^{\theta}.$$

After introducing the previous equation into Eq. (13) the stationary condition attains the following form

$$\left( \delta \mathbf{r}_r^i \right)^T \mathbf{K}_r^i \mathbf{r}_r^i + \left( \delta \mathbf{r}_r^i \right)^T \sum_j \mathbf{K}_r^{ij} \mathbf{r}_r^j = \left( \delta \mathbf{r}_r^i \right)^T \mathbf{R}_e^i, \quad (20)$$

Where the individual matrices are defined as

$$\mathbf{K}_r^i = \int_{\Omega} \mathbf{N}_r^T(\mathbf{x}) \mathbf{c}_i(\mathbf{x}) (\mathbf{L}_i - \mathbf{L}_0)^{-1} \mathbf{N}_r(\mathbf{x}) d\Omega,$$

$$\mathbf{K}_r^{ij} = \int_{\Omega} \mathbf{N}_r^T(\mathbf{x}) \boldsymbol{\Gamma}_h(\mathbf{x}, \mathbf{y}) \mathbf{S}_{ij}(\mathbf{x}, \mathbf{y}) \mathbf{N}_r(\mathbf{y}) d\Omega,$$

$$\mathbf{R}_e^i = \int_{\Omega} \mathbf{N}_r^T(\mathbf{x}) \mathbf{c}_i(\mathbf{x}) \boldsymbol{\varepsilon}_0(\mathbf{x}) d\Omega$$

Note that, in view of numerical implementation, we use a standard matrix representation of tensor quantities, as defined in [9], in the presentation.

To complete the solution, we need to specify the boundary element approximation for the function  $\boldsymbol{\Gamma}_h(\mathbf{x}, \mathbf{y})$ :

$$\boldsymbol{\Gamma}_h(\mathbf{x}, \mathbf{y}) = \psi^*(\mathbf{x}, \mathbf{y}) - \int_{\Gamma} \mathbf{H}^*(\mathbf{x}, \mathbf{y}) \mathbf{N}(\mathbf{x}) d\Gamma \mathbf{U}^{-1} \mathbf{E}^*(\mathbf{x}),$$

where  $\mathbf{E}^*(\mathbf{x})$  is a vector [1 x dof] for each state  $\alpha$  and at each point  $\mathbf{x}$ , and dof is the number of degrees of freedom on the boundary,

$\mathbf{U}$  is a square regular matrix [dof x dof] and the sign \* corresponds to a kernel, for more information refer to [4].

#### 5. Numerical example

Consider the one dimensional elastic problem in Figure 2, assigning  $E_r$  to each phase together with specifying boundary condition and loading according to Figure 2 with  $L=1\text{m}$

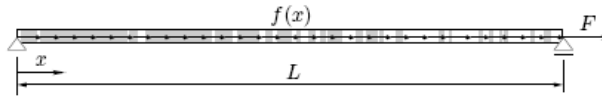


Figure 2 Mechanical problem for realization a

Two different load cases were considered, the structure loaded by distributed load  $f=1 \text{ Nm}^{-1}$  and by concentrated load  $F=1 \text{ N}$ . For each realization it was considered that  $E_r=1 \text{ Pa}$  and by varying  $E_2$ , we examined the influence of the stiffness ratio  $E_2/E_1$ , the discretization parameter  $h$  and microstructural length  $l$  on the quality of the approximate solution. The resulting relations are depicted in Figure 3, 4. In particular, the visualization are used here is based on the relative  $L_2$  norm defined as

$$\eta^n := \frac{\|u_h(\mathbf{x}) - u_{ex}(\mathbf{x})\|_{L_2}}{\|u_{ex}(\mathbf{x})\|_{L_2}} \quad \text{where} \quad \|f(\mathbf{x})\|^2 := \int_{\Omega} f^2(\mathbf{x})d\Omega$$

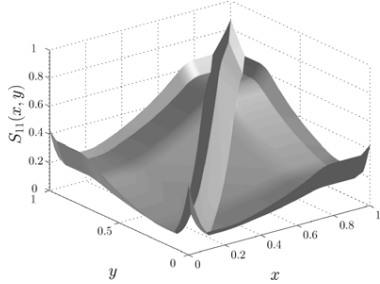


Figure 5. Example of two point probability function

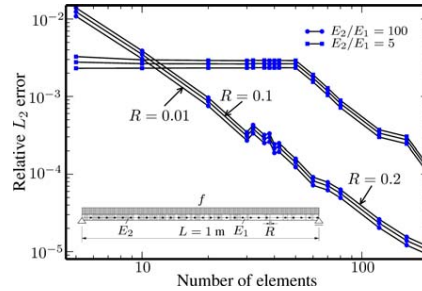


Figure 6. Relative  $L_2$  error

### 6. Conclusion

In this work, an outline microstructure-based model for the elasticity of FGM was set out. Using BEM and discretization of the Hashin-Shtrikman principle, the behavior of the FGM may be described. The dominant factors influencing the convergence are the relative size of microstructure  $\Omega_i / \Omega$ , and the ratio  $E_2 / E_1$  according to Figure 6. From the computational complexity point of view, the BEM-based method is slightly more efficient compared to FEM, mainly in the phase of the reference solution.

The next logical step of the work presented in this contribution is to generalize the implementation to more dimensions and to multi-physics analysis. Once this goal is completed, the resulting formulation is very well suited to optimization studies of statistically inhomogeneous material systems. The specific non-linear behavior of materials can also be considered.

**Acknowledgments.** The financial support of this work provided by grants No.GACR 103/07/0304 and CZE MSM 684 077 0001, 3 of the Grant Agency of the Czech Republic is gratefully acknowledged.

### References

- [1] Bittnar, Z. and Šejnoha, J., "Numerical methods in structural engineering", ASCE Press, 1996
- [2] Luciano, R. and Willis, J.R., "FE analysis of stress and strain fields in finite random composite bodies", Journal of the Mechanics and Physics of Solids, Vol. 53, No. 7, 2005, pp 1505–1522.
- [3] Luciano, R. and Willis, J.R., "Hashin-Shtrikman based FE analysis of the elastic behaviour of finite random composite bodies", International Journal of Fracture, Vol. 137, Nos. 1–4, 2006, pp 261–273.
- [4] Procházka, P. and Šejnoha, J., "A BEM formulation for homogenization of composites with randomly distributed fibers", Engineering Analysis with Boundary Elements, Vol. 27, No 2, 2003, pp 137–144.
- [5] Quintanilla, J. and Torquato, S., "Microstructure functions for a model of statistically inhomogeneous random media", Physical Review E, Vol. 55, No. 2, 1997, pp 1558–1565.
- [6] Sharif-Khodaei, Z., "Preliminaries to modeling and analysis of functionally graded materials". Diploma thesis, Faculty of Civil Engineering, Czech Technical University in Prague, 2006
- [7] Sharif-Khodaei, Z. and Zeman, J., "Elastic modeling of functionally graded materials: One dimensional case", In F. Matejíček, editor, Paper of Proceedings of the 5th International Congress of Croatian Society of Mechanics, Croatian Society of Mechanics, 2006.
- [8] Willis, J. R., "Variational and related methods for the overall properties of composites", In Advances in Applied Mechanics, Vol. 21, 1981, pp 2–74
- [9] Procházka, P. and Šejnoha, "Hashin-Shtrikman variational principles, Applications of mathematics, 2003



## Exact transformation of domain integrals into boundary integrals in BEM formulation of 2D and 3D thermoelasticity

M. R. Hematiyan

Department of Mechanical Engineering, Shiraz University,  
Shiraz, Iran, mhemat@shirazu.ac.ir

**Keywords:** Boundary element method, Thermoelasticity, Domain integral, Boundary integral

**Abstract.** A method for exact transformation of BEM domain integrals of 2D and 3D thermoelasticity is presented. Domain integrals are transformed to boundary by Green's theorem. Temperature rise through the domain can have a cubic variation in one Cartesian direction and arbitrary variations in other directions. Boundary integrals are evaluated by an adaptive method. Two examples are presented to show the validity and accuracy of the method.

### Introduction

For thermoelasticity, the conventional boundary element method (BEM) involves a domain integral. If these domain integral cannot be evaluated by boundary-only discretization, BEM loses its main attractive feature.

When the temperature field satisfies the Laplace equation, the domain integral can be exactly converted into a boundary integral [1, 2]. Some methods for treatment of domain integrals in elasticity and thermoelasticity are reviewed in the paper by Cheng et al [1]. Radial integration method (RIM) [3, 4] is a powerful method for evaluation of domain integrals with boundary-only discretization. In this method the integrand is expressed in a radial form and the domain integral is transformed to a double integral consisting of a boundary integral and a radial integral. Once the radial integral is evaluated analytically, the domain integral can be transformed exactly to boundary.

Recently, Hematiyan [5] presented an adaptive meshless method for evaluation of domain integrals. In this method, the domain integral is not transformed to boundary, but the integral is evaluated with boundary-only discretization. This method can be used for the accurate evaluation of very complicated 2D and 3D domain integrals.

In the present work, the domain integrals appearing in 2D and 3D BEM formulation of thermoelasticity are exactly transformed into boundary integrals by Green's theorems. Domain integrals corresponding to temperature fields with a cubic variation in one Cartesian direction and arbitrary variations in other directions can be exactly transformed to boundary by the method to be presented in this paper.

When the temperature is expressed by discrete values, it must be approximated by interpolation functions. An important feature of the proposed method is that the approximate function can be simply defined in a global Cartesian coordinates system and there is no need for defining interpolating functions in radial form.

### Integral equation of thermoelasticity

Displacement integral equation of thermoelasticity can be expressed as [2]:

$$C_{ij}(\mathbf{x}')u_j(\mathbf{x}') + \int_S T_{ij}(\mathbf{x}', \mathbf{x})u_j(\mathbf{x})dS = \int_S U_{ij}(\mathbf{x}', \mathbf{x})t_j(\mathbf{x})dS + \frac{Eh}{1-2\nu} \int_V U_{ik,k}(\mathbf{x}', \mathbf{x})\theta(\mathbf{x})dV \quad (1)$$

where  $\mathbf{x}'$  and  $\mathbf{x}$  are respectively source point and field point.  $\theta$  is the temperature rise,  $E$  is the Young's modulus,  $\nu$  is the Poisson's ratio and  $h$  is the coefficient of linear thermal expansion.  $U_{ij}$  and  $T_{ij}$  are fundamental solutions in terms of displacement and traction.  $u_j$  and  $t_j$  are respectively displacement and traction components.  $S$  and  $V$  represent boundary and domain of the problem respectively and  $C_{ij}(\mathbf{x}')$  represents coefficient matrix of the free term. The last integral in eq (1) is a domain integral. The fundamental solution of 2D thermoelasticity, in terms of displacement can be expressed as

$$U_{ik}(\mathbf{x}', \mathbf{x}) = A \ln\left(\frac{1}{r}\right) \delta_{ik} + B \frac{\partial r}{\partial x_i} \frac{\partial r}{\partial x_k} = A \ln\left(\frac{1}{r}\right) \delta_{ik} + B \frac{r_i r_k}{r^2} \quad (2)$$

where  $r$  is the Euclidean distance from source point to field point which can be expressed as

$$r = |\mathbf{x} - \mathbf{x}'| = \sqrt{r_i r_i}, \quad r_i = (x_i - x'_i), \quad i = 1, 2.$$

The fundamental solution of 3D thermoelasticity, in terms of displacement can be written as

$$U_{ik}(\mathbf{x}', \mathbf{x}) = D \frac{1}{r} \delta_{ik} + F \frac{1}{r} \frac{\partial r}{\partial x_i} \frac{\partial r}{\partial x_k} = D \frac{1}{r} \delta_{ik} + F \frac{r_i r_k}{r^3} \quad (3)$$

Coefficients  $A$ ,  $B$ ,  $D$  and  $F$  in (2) and (3) are material dependent constants [2].

**Transformation of domain integral to boundary integral in 2D thermoelasticity.** The domain integral of 2D thermoelasticity can be expressed as

$$I = \int_V \theta(\mathbf{x}) \frac{r_i}{r^2} dV \quad (4)$$

The above integral is obtained by substituting the expression in the right side of eq (2) in the last integral of eq (1). The constant coefficient has also been removed.

Assuming that temperature rise  $\theta$  has an arbitrary distribution in direction  $x_2$  and a cubic distribution in direction  $x_1$ , the domain integral (4) can be written as:

$$I = \int_V [f_0(x_2) + f_1(x_2)x_1 + f_2(x_2)x_1^2 + f_3(x_2)x_1^3] \frac{r_i}{r^2} dV. \quad (5)$$

To transform this domain integral into a boundary integral, Green's theorem is employed. Green's theorem is expressed as [6],

$$\int_V \frac{\partial g(\mathbf{x})}{\partial x_1} dV = \int_S g(\mathbf{x}) dx_2 \quad (6)$$

$$\int_V \frac{\partial g(\mathbf{x})}{\partial x_2} dV = - \int_S g(\mathbf{x}) dx_1 \quad (7)$$

By setting  $w(\mathbf{x}) = \frac{\partial g(\mathbf{x})}{\partial x_1}$ , the eq (6) can be rewritten as

$$\int_V w(\mathbf{x}) dV = \int_S \left( \int w(\mathbf{x}) dx_1 \right) dx_2 \quad (8)$$

Similarly, using eq (7), one can show that

$$\int_V w(\mathbf{x}) dV = - \int_S \left( \int w(\mathbf{x}) dx_2 \right) dx_1 \quad (9)$$

By observing equations (8) and (9) one can find that if integrand of a 2D domain integral is integrable with respect to  $x_1$  or  $x_2$ , the domain integral can be transformed to a boundary integral. As it will be seen, the integrand of eq (4) is integrable with respect to  $x_1$  and can be transformed into a boundary integral by eq (8).

The domain integral (5) can be written as

$$I = I_0 + I_1 + I_2 + I_3 \quad (10)$$

where

$$I_\alpha = \int_V [f_\alpha(x_2) x_1^\alpha] \frac{r_i}{r^2} dV \quad \alpha = 0, 1, 2, 3 \quad (11)$$

Using formula (8) one can write

$$I_\alpha = \int_S F_\alpha(x_1, x_2) dx_2 \quad (12)$$

where

$$F_\alpha(x_1, x_2) = \int [f_\alpha(x_2)x_1^\alpha] \frac{r_i}{r^2} dx_1 \tag{13}$$

or

$$F_\alpha(x_1, x_2) = f_\alpha(x_2) \int x_1^\alpha \frac{r_i}{r^2} dx_1 \tag{14}$$

The one-dimensional integral in the right side of eq (14) can be evaluated analytically as follows:

$$\begin{aligned} \int \frac{r_i}{r^2} dx_1 &= \ln r \\ \int x_1 \frac{r_i}{r^2} dx_1 &= \xi_1 \ln r - r_2 \tan^{-1}\left(\frac{r_1}{r_2}\right) + x_1 \\ \int x_1^2 \frac{r_i}{r^2} dx_1 &= (\xi_1^2 - r_2^2) \ln r - 2\xi_1 r_2 \tan^{-1}\left(\frac{r_1}{r_2}\right) + \frac{1}{2}x_1^2 + x_1 \xi_1 \\ \int x_1^3 \frac{r_i}{r^2} dx_1 &= \xi_1 (\xi_1^2 - 3r_2^2) \ln r + r_2 (r_2^2 - 3\xi_1^2) \tan^{-1}\left(\frac{r_1}{r_2}\right) + x_1 \xi_1^2 + \frac{1}{2}x_1^2 \xi_1 + \frac{1}{3}x_1^3 - x_1 r_2^2 \\ \int \frac{r_2}{r^2} dx_1 &= \tan^{-1}\left(\frac{r_1}{r_2}\right) \\ \int x_1 \frac{r_2}{r^2} dx_1 &= r_2 \ln r + \xi_1 \tan^{-1}\left(\frac{r_1}{r_2}\right) \\ \int x_1^2 \frac{r_2}{r^2} dx_1 &= 2r_2 \xi_1 \ln r + (\xi_1^2 - r_2^2) \tan^{-1}\left(\frac{r_1}{r_2}\right) + r_2 x_1 \\ \int x_1^3 \frac{r_2}{r^2} dx_1 &= r_2 (3\xi_1^2 - r_2^2) \ln r + \xi_1 (\xi_1^2 - 3r_2^2) \tan^{-1}\left(\frac{r_1}{r_2}\right) + 2r_2 x_1 \xi_1 + \frac{1}{2}r_2 x_1^2 \end{aligned}$$

Similarly, domain integral (4) associated to a temperature rise with an arbitrary distribution in direction  $x_1$  and a cubic distribution in direction  $x_2$  can be exactly transformed to boundary. Consequently, the domain integral (4) associated to a temperature rise with the form,

$$\begin{aligned} \theta(\mathbf{x}) &= f_0(x_2) + f_1(x_2)x_1 + f_2(x_2)x_1^2 + f_3(x_2)x_1^3 + \\ &h_0(x_1) + h_1(x_1)x_2 + h_2(x_1)x_2^2 + h_3(x_1)x_2^3 \end{aligned}$$

can be exactly transformed to boundary.

**Transformation of domain integral to boundary integral in 3D thermoelasticity.** The domain integral of 3D thermoelasticity can be expressed as

$$I = \int_V \theta(\mathbf{x}) \frac{r_i}{r^3} dV \tag{15}$$

The above integral is obtained by substituting the expression in the right side of eq (3) in the last integral of eq (1).

Assuming that the temperature rise  $\theta$  has arbitrary distributions in directions  $x_2$  and  $x_3$  and a cubic distribution in direction  $x_1$ , the domain integral (15) can be written as:

$$I = \int_V [f_0(x_2, x_3) + f_1(x_2, x_3)x_1 + f_2(x_2, x_3)x_1^2 + f_3(x_2, x_3)x_1^3] \frac{r_i}{r^3} dV. \tag{16}$$

Similar to 2D, Green's theorem is used to transform this domain integral to boundary.

Green's theorem in 3D can be expressed as [6]

$$\int_V \frac{\partial g(\mathbf{x})}{\partial x_i} dV = \int_S g(\mathbf{x}) n_i dS \tag{17}$$

where  $n_i$  is the component of unit vector  $\mathbf{n}$  normal to the boundary.

By setting  $w(\mathbf{x}) = \frac{\partial g(\mathbf{x})}{\partial x_1}$ , the eq (17) can be rewritten as

$$\int_V w(\mathbf{x}) dV = \int_S \left( \int w(\mathbf{x}) dx_1 \right) n_1 dS \quad (18)$$

By observing this equation, one can say that if integrand of a 3D domain integral is integrable with respect to only one of Cartesian coordinates, the domain integral can be transformed into a boundary integral. Similar to 2D, it will be shown that the integrand of eq (16) is integrable with respect to  $x_1$  and can be transformed into a boundary integral.

The domain integral (16) can be written as

$$I = I_0 + I_1 + I_2 + I_3 \quad (19)$$

where

$$I_\alpha = \int_V [f_\alpha(x_2, x_3) x_1^\alpha] \frac{r_i}{r^3} dV \quad \alpha = 0, 1, 2, 3 \quad (20)$$

Using formula (18) one can write

$$I_\alpha = \int_S F_\alpha(x_1, x_2, x_3) n_1 dS \quad (21)$$

where

$$F_\alpha(x_1, x_2, x_3) = \int [f_\alpha(x_2, x_3) x_1^\alpha] \frac{r_i}{r^3} dx_1 \quad (22)$$

or

$$F_\alpha(x_1, x_2, x_3) = f_\alpha(x_2, x_3) \int x_1^\alpha \frac{r_i}{r^3} dx_1 \quad (23)$$

The one-dimensional integral in the right side of eq (23) can be evaluated analytically. For  $i=1$ , it can be expressed as follows:

$$\begin{aligned} \int \frac{r_1}{r^3} dx_1 &= -\frac{1}{r} \\ \int x_1 \frac{r_1}{r^3} dx_1 &= -\frac{x_1}{r} + \ln(r_1 + r) \\ \int x_1^2 \frac{r_1}{r^3} dx_1 &= 2\xi_1 \ln(r_1 + r) + 2r - \frac{x_1^2}{r} \\ \int x_1^3 \frac{r_1}{r^3} dx_1 &= \frac{1}{2r} [x_1^3 + 3\xi_1 x_1^2 + 3x_1(r^2 - r_1^2 - 5\xi_1^2) + 9\xi_1(\xi_1^2 + r^2 - r_1^2)] + \\ &\quad \frac{3}{2} (2\xi_1^2 - r^2 + r_1^2) \ln(r_1 + r) \end{aligned}$$

For  $i \neq 1$  ( $i=2$  or  $3$ ), it can be expressed as follows:

$$\begin{aligned} \int \frac{r_i}{r^3} dx_1 &= \frac{r_1}{r(r^2 - r_1^2)} r_i \\ \int x_1 \frac{r_i}{r^3} dx_1 &= \left[ \frac{r_1 \xi_1}{r(r^2 - r_1^2)} - \frac{1}{r} \right] r_i \\ \int x_1^2 \frac{r_i}{r^3} dx_1 &= \left[ \frac{r_1 \xi_1^2}{r(r^2 - r_1^2)} + \ln(r_1 + r) - \frac{x_1 + \xi_1}{r} \right] r_i \\ \int x_1^3 \frac{r_i}{r^3} dx_1 &= [2r^2 - r_1^2 - 3\xi_1 x_1 + 3\xi_1 r \ln(r_1 + r) + \frac{\xi_1^3 r_1}{(r^2 - r_1^2)}] \frac{r_i}{r} \end{aligned}$$

Similarly, a temperature rise with a cubic distribution in directions  $x_2$  or  $x_3$  and arbitrary distributions in other directions can be exactly transformed to boundary. Consequently, a temperature rise with the form,

$$\theta(\mathbf{x}) = f_0(x_2, x_3) + f_1(x_2, x_3)x_1 + f_2(x_2, x_3)x_1^2 + f_3(x_2, x_3)x_1^3 + h_0(x_1, x_3) + h_1(x_1, x_3)x_2 + h_2(x_1, x_3)x_2^2 + h_3(x_1, x_3)x_2^3 + q_0(x_1, x_2) + q_1(x_1, x_2)x_3 + q_2(x_1, x_2)x_3^2 + q_3(x_1, x_2)x_3^3$$

can be exactly treated in BEM formulation of 3D thermoelasticity.

**Examples**

Two examples are presented to show the validity and accuracy of the present method. In the two examples, all boundary integrals are evaluated by Simpson adaptive integration method with tolerance of  $\epsilon_{\text{int}} = 10^{-6}$ .

**Example1: 2D domain.** In this example, the following integral is to be computed:

$$I = \int_V \theta(\mathbf{x}) \frac{r_i}{r^2} dV$$

where

$$\theta(\mathbf{x}) = (1 + x_2)^4 + [\sin(2\pi x_2)]x_1 + \frac{1}{(2 + x_2)^3}x_1^3.$$

The domain  $V$  is shown in the Fig. 1. Calculated values for the integral by the present method are compared with an accurate solution. The accurate solution has been obtained by an adaptive integration method with internal evaluation of the integrand [5].

The results for some different analyses are given in the Table 1. As seen, the obtained results are satisfactory.

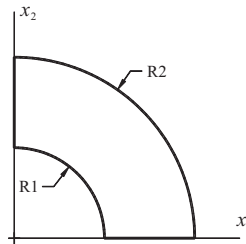


Figure 1: 2D domain

Source point location	Singular kernel	Present Method			Accurate solution with internal evaluation
		6 quadratic boundary elements	12 quadratic boundary elements	24 quadratic boundary elements	
(1,0)	$\frac{r_1}{r^2}$	0.959495	0.961103	0.961128	0.961118
(0.5,1.5)	$\frac{r_2}{r^2}$	1.55236	1.55518	1.55564	1.55584
(1,0)	$\frac{r_1}{r^2}$	6.31231	6.31811	6.31843	6.31855
(0.5,1.5)	$\frac{r_2}{r^2}$	3.00537	3.02209	3.02301	3.02342

Table 1: Computed values for the domain integral of example 1

**Example 2: 3D domain.** In this example, the following integral is to be computed:

$$I = \int_V \theta(\mathbf{x}) \frac{r_1}{r^3} dV$$

where

$$\theta(\mathbf{x}) = \sin(8x_2x_3) + (x_2^2 + x_3^5)x_1 + x_1^2.$$

The domain  $V$  is a  $1 \times 1 \times 1$  cube with two corner points  $P_1 = (0,0,0)$  and  $P_2 = (1,1,1)$ . The boundary of the problem is discretized by only 6 linear 4-node boundary elements. The source point is located at  $(0.2,0.3,0.4)$ . An accurate value for this integral has been obtained by an adaptive method with internal evaluation [5]. The accurate value is 0.630857. The calculated value for the integral, by the present method is 0.630860, which shows an excellent agreement with the accurate solution.

#### Comments and conclusions

A method for exact transformation of thermoelasticity domain integrals to boundary was presented. By the present method, a wide range of domain integrals can be exactly transformed to boundary. By presenting two examples and comparing the obtained results with accurate solutions it was shown that the method is sufficiently efficient.

Although the emphasis was made on BEM formulation of thermoelasticity, the present method can be used for exact transformation of domain integrals to boundary for many other problems. A special characteristic of the present method in comparison to other methods is that it is formulated in a Cartesian coordinate system instead of polar coordinates.

#### References

- [1] A.H.D. Cheng, C.S. Chen, M.A. Golberg and Y.F. Rashed *Engineering Analysis with Boundary Elements*, **25**, 377-387 (2001).
- [2] M.H. Aliabadi *The boundary element method, Vol. 2: Applications in Solids and Structures*, John Wiley & Sons (2002).
- [3] X.W. Gao *Engineering Analysis with Boundary Elements*, **26**, 905-916 (2002).
- [4] X.W. Gao *Journal of Computational and Applied Mathematics*, **175**, 265-290 (2005).
- [5] M.R. Hematiyan *Computational Mechanics*, **39**, 509-520 (2007).
- [6] W.M. Lai, D. Rubin and E. Kremple *Introduction to Continuum Mechanics, Third Edition*, Butterworth-Heinemann (1999).

## Adaptive FEM-BEM Coupling Method for Elasto-Plastic Analysis

W. Elleithy and U. Langer

Institute of Computational Mathematics, Johannes Kepler University Linz, Austria

E-mail: wael.elleithy@numa.uni-linz.ac.at

E-mail: ulanger@numa.uni-linz.ac.at

**Keywords:** FEM; BEM; Adaptive Coupling; Elasto-Plasticity

**Abstract.** In this paper we present an adaptive FEM-BEM coupling method for elasto-plastic analysis in which the nonlinearity, e.g., plastic material behavior, is treated by the FEM while large parts of the finite/infinite linear elastic body are treated using the BEM. A procedure that is easily automated is developed to generate and adapt the FEM zone of discretization (consequently the BEM sub-domain discretization), according to the state of computation. The adaptive FEM-BEM coupling method employs smaller FEM zones of discretization (FEM sub-domain). The adaptive coupling method eliminates the disadvantages of a prior definition and manual localization of the FEM and BEM sub-domains.

### Introduction

The Finite Element Method (FEM) and the Boundary Element Method (BEM) are valuable and frequently used discretization techniques for obtaining approximate solutions to the partial differential equations that arise in scientific and engineering applications. The FEM, e.g., is especially well suited for the analysis of problems involving inhomogeneities or non-linear behavior, while the BEM has some advantages if stress singularities or unbounded sub-regions are present. It is conceptually and computationally very attractive to decompose the domain of the original problem and to use the most appropriate discretization method for the sub-domains under consideration. In this way, we are lead to the coupling of FEM and BEM (FEM-BEM coupling).

The first FEM-BEM coupling investigations date back to 1977 with the pioneering work of Zienkiewicz, Kelly and Bettles [1] based on a standard collocation BEM approach. Since then a large number of papers devoted to the topic have appeared. Due to the unsymmetrical nature of the BEM technique used, the usefulness of the FEM-BEM coupling method has been limited. FEM-BEM coupling approaches based on the Symmetric Galerkin BEM (SGBEM) are quite recent; see, e.g., references [2-9].

The available coupling approaches necessitate a priori defined FEM and BEM zones of discretization (set by the user). Furthermore, the FEM and BEM zones remain unchanged during the computation. Unfortunately, a predefined FEM zone of discretization will probably result in either an under/overestimation of the nonlinear region where the FEM is employed. In the former case, inaccurate solutions is obtained to the problem at hand while for the later the computational cost may be higher than necessary.

This paper presents an adaptive FEM-BEM coupling method that is capable of predicting zones sensible for FEM discretization. An outline of the paper is as follows. Section 2 briefly summarizes the basic SGBEM equations in elasticity, FEM equations in elasto-plasticity and the conventional (direct) and iterative FEM-BEM coupling methods. Then, in Section 3, we present the adaptive FEM-BEM coupling method. A numerical example that illustrates the advantages of the adaptive FEM-BEM coupling method is given in Section 4.

### FEM-BEM Coupling

The system of boundary integral equations for a mixed boundary value problem in linear elasticity, may be written as follows

$$\begin{pmatrix} u \\ t \end{pmatrix} = \begin{pmatrix} \frac{1}{2}I - K & V \\ D & \frac{1}{2}I + K' \end{pmatrix} \begin{pmatrix} u \\ t \end{pmatrix} \quad (1)$$

where  $V$ ,  $K$ , and  $D$  are the single layer potential, double layer potential, hypersingular integral operators, respectively. In order to find the complete Cauchy data  $[u, t]_{\Gamma}$ , the first integral equation for  $x \in \Gamma_D$  and the second one for  $x \in \Gamma_N$  are rewritten as [10,11]

$$(Vt)(x) = \frac{1}{2}g(x) + (Ku)(x) \text{ for } x \in \Gamma_D \quad (2)$$

$$(Du)(x) = \frac{1}{2}h(x) - (K'u)(x) \text{ for } x \in \Gamma_N \quad (3)$$

where  $g(x)$  and  $h(x)$  are the given Dirichlet and Neumann data.

A Galerkin discretization is equivalent to the skew symmetric and positive definite system of linear equations

$$\begin{pmatrix} V_h & -K_h \\ K_h^T & D_h \end{pmatrix} \begin{pmatrix} \underline{t}^h \\ \underline{u}^h \end{pmatrix} = \begin{pmatrix} \underline{f}_1 \\ \underline{f}_2 \end{pmatrix} \quad (4)$$

where the block matrices in eq. (4) are given from discretization of the corresponding parts of the boundary.

In typical applications in linear elastostatics the Dirichlet part  $\Gamma_D$ , is often small compared to the Neumann part  $\Gamma_N$  where the boundary tractions are described. Therefore the inverse of the discrete single layer potential  $V_h$  may be computed using some direct method such as a Cholesky decomposition to obtain

$$\underline{t}^h = V_h^{-1} \left[ \underline{f}_1 + K_h \underline{u}^h \right]. \quad (5)$$

Inserting eq (5) into the second of eq (4) yields the Schur complement system

$$\left[ D_h + K_h^T V_h^{-1} K_h \right] \underline{u}^h = \underline{f}_2 - K_h^T V_h^{-1} \underline{f}_1. \quad (6)$$

The Schur complement system (6) is symmetric and positive definite and is suitable for coupling with FEM.

For a numerical representation of an arbitrary domain,  $\Omega$ , with known boundary conditions specified at the entire boundary,  $\Gamma = \Gamma_N \cup \Gamma_D$ , the FEM and BEM are used. The domain is decomposed into two sub-domains, namely,  ${}_F\Omega$  and  ${}_B\Omega$  with the FEM-BEM coupling interface  $\Gamma_C$ . In all following equations subscripts  $F$  and  $B$  stand for *Finite Element* and *Boundary Element* sub-domains, respectively.

System (6) may be rewritten as

$$\begin{bmatrix} {}_B K_{CC} & {}_B K_{CB} \\ {}_B K_{BC} & {}_B K_{BB} \end{bmatrix} \begin{bmatrix} {}_B u_C \\ {}_B u \end{bmatrix} = \begin{bmatrix} {}_B f_C \\ {}_B f \end{bmatrix}. \quad (7)$$

For the FEM sub-domain, the assembled finite element equations in elasticity in partitioned form are

$$\begin{bmatrix} {}_F K_{FF} & {}_F K_{FC} \\ {}_F K_{CF} & {}_F K_{CC} \end{bmatrix} \begin{bmatrix} {}_F u \\ {}_F u_C \end{bmatrix} = \begin{bmatrix} {}_F f \\ {}_F f_C \end{bmatrix} \quad (8)$$

where  ${}_F K$  is the complete FEM stiffness matrix.

The stiffness matrix  ${}_B K$  can be interpreted as the element stiffness matrix of a finite macro element, computed by the BEM

$$\begin{bmatrix} {}_F K_{FF} & {}_F K_{FC} \\ {}_F K_{CF} & {}_F K_{CC} + {}_B K_{CC} \end{bmatrix} \begin{bmatrix} {}_F u \\ u_C \end{bmatrix} = \begin{bmatrix} {}_F f \\ {}_B f_C + {}_F f_C \end{bmatrix}. \quad (9)$$

For an elasto-plastic analysis, the incremental form of the FEM equations, in a partitioned form are

$$\begin{bmatrix} \Delta {}_F \psi \\ \Delta {}_F \psi_C \end{bmatrix} = \begin{bmatrix} {}_F K_T{}_{FF} & {}_F K_T{}_{FC} \\ {}_F K_T{}_{CF} & {}_F K_T{}_{CC} \end{bmatrix} \begin{bmatrix} \Delta {}_F u \\ \Delta {}_F u_C \end{bmatrix} - \begin{bmatrix} \Delta {}_F f \\ \Delta {}_F f_C \end{bmatrix} \quad (10)$$

where  $K_T$  is the tangent stiffness matrix and  $\Delta \psi$  is the residual (or out-of-balance) force vector. It should be noted that for each load increment, eq (10) are nonlinear and therefore are solved iteratively. Standard solution procedure, at each load increment, contains iterations over computations of tangent stiffness (based on current stress, and plastic strain, if required), applied loads based on current configuration, internal force and force

residual. Then, displacement increment is calculated. With updated displacements the plastic strain increments at element integration points are obtained. Finally, check on convergence is carried out. If the procedure converged, plastic strains are updated and next increment proceeds.

Elasto-plastic problems with limited spread of plastic strains lend themselves to a coupled approach, where the plastic material behavior, is treated by the FEM while large parts of the finite/infinite linear elastic body are treated using the BEM. For each load increment, the following global equation systems are solved at each iteration

$$\begin{bmatrix} \Delta_F \psi \\ \Delta \psi_C \\ \Delta_B \psi \end{bmatrix} = \begin{bmatrix} {}_F K_{TFF} & {}_F K_{TFC} \\ {}_F K_{TCF} & {}_F K_{TCC} + {}_B K_{CC} \\ & {}_B K_{BC} \end{bmatrix} \begin{bmatrix} \Delta_F u \\ \Delta u_C \\ \Delta_B u \end{bmatrix} - \begin{bmatrix} \Delta_F f \\ \Delta_B f_C + \Delta_F f_C \\ \Delta_B f \end{bmatrix}. \quad (11)$$

As an alternative to the conventional (direct) FEM-BEM coupling approach, a partitioned solution scheme can be used, where the systems of equations of the sub-domains are solved independently of each other. The interaction effects are taken into account as boundary conditions, which are imposed on the coupling interfaces. Iterations are performed in order to enforce satisfaction of the coupling conditions. Within the iteration procedure, a relaxation operator is applied to the interface boundary conditions in order to enable and speed up convergence. In this sense, the iterative coupling approaches are called interface relaxation FEM-BEM coupling methods. Interface relaxation FEM-BEM coupling methods in elasto-plasticity are discussed in details in reference [12].

#### Adaptive FEM-BEM Coupling Method

As mentioned earlier, it is not useful to predefine the FEM and BEM zones of discretization in an elasto-plastic FEM-BEM coupling analysis. The predefinition of the zones of discretization, will probably result in either an under/overestimation of the nonlinear region where the FEM is employed. More effective is a mechanism that allows an automated generation and adaption of the FEM zone of discretization. In order to avoid inaccurate or costly computations we propose in this section an adaptive FEM-BEM coupling method that automatically generate and progressively adapt the finite and boundary element zones of discretization. The adaptive FEM-BEM coupling method in elasto-plasticity follows the five basic steps:

1. Load increment and BEM elastic analysis with an initial BEM discretization.  
An hypothetical elastic stress state is determined
2. Detection of zones sensible for FEM discretization  
The hypothetical stress values computed at predefined points inside the BEM domain are checked against yielding (elastic prediction). Violation to the yield condition provides an initial estimate of the zones sensible for discretization by FEM (Fig. 1). For a final estimate of the FEM zones of discretization we propose to use simple fast post-calculations based on energetic methods, e.g., Neuber's and strain energy density methods [13]. This will account for relaxation and redistribution of stresses that occur due to plastic deformation.
3. Automatic generation of FEM zone of discretization (consequently the BEM sub-domain discretization) for the current state of computation  
Particular regions that fulfil the proposed criterion are discretized by the FEM. In order to ensure the compatible coupling between the remaining BEM zone and the FEM zone, the interface is constructed reflecting the current situation. It is useful to reuse the BEM internal points as finite element nodes for the FEM discretization, as they are conveniently distributed in the particular area of interest. This will result in a reduction of the complexity of data management and ease of the automatic generation and adaption of the FEM zone of discretization.
4. Coupled FEM-BEM stress analysis involving elasto-plastic deformations is then conducted
5. Next load increment requires a repetition of steps 1-4.

In our adaptive method, the user needs not to predefine the zones of discretization. In the remainder of this section we will briefly elaborate on the post-calculations for the final estimate of the FEM zone of discretization. Let us consider materials of von-Mises type obeying a multilinear strain hardening rule. Neuber's and strain energy density methods (Fig. 2) are energy equivalence between the hypothetical elastic and the elasto-plastic calculations of the same geometry submitted to the same loading [13]. For uni-dimensional states of stress, the product stress x strain in elasticity is assumed to be locally identical to the same product calculated by means of an elasto-plastic analysis. For tri-dimensional states of stress, the fundamental hypothesis may be written as

$$\sigma_{ij} \varepsilon_{ij} = (\sigma_{ij} \varepsilon_{ij})_{elas} \quad (12)$$

where  $(\cdot)_{elas}$  corresponds to values determined from hypothetical elastic computations. The energy density balance, eq (12), is obtained by using the defined quantities appropriately for the actual elasto-plastic stress-strain state and the hypothetical elastic stress-strain state. However, a local method leads to a violation of equilibrium. Thus a proportionality factor is to be introduced in order to account for the stress relaxation and redistribution due to plastic deformations. From a virtual work principle we may utilize a global formulation

$$\left( \int_{\Omega} \sigma_{ij} \varepsilon_{ij}^* dV \right)_{elastic-plastic \text{ computation}} \approx \left( \int_{\Omega} \sigma_{ij} \varepsilon_{ij}^* dV \right)_{elastic \text{ computation}} \quad (13)$$

Based on the global formulation, eq (13), we propose a simple, yet effective, method for a final estimation of the FEM zones of discretization. The basic steps of post-calculations are summarized as

- 1- For regions that is initially predicted to yield (elastic prediction), compute the net values of the strain energy densities. This is achieved by subtracting the strain energy density that corresponds to the elastic limit from the hypothetical densities based on elastic BEM analysis
- 2- With the net values of strain energy densities of step 1, compute the net value of the strain energy (integrated over the initially estimated FEM discretization regions)
- 3- With the net strain energy that is vulnerable for redistribution computed in step 2 and the total hypothetical elastic strain energy of the whole domain, a pseudo value of the yielding strength is determined while assuming an equivalence of the actual tri-dimensional stress-strain state and a uni-dimensional state (Fig. 2)
- 4- For the whole domain, a final estimate of the FEM zone of discretization is achieved utilizing the strain energy yielding theory with a pseudo value of the material yield strength computed in step 3.

The procedure outlined with its inherent assumptions, provide a simple, fast and effective method for a final estimation of the FEM and BEM zones of discretization. A usual FEM-BEM coupling analysis is then conducted while utilizing the finally estimated zones of discretization.

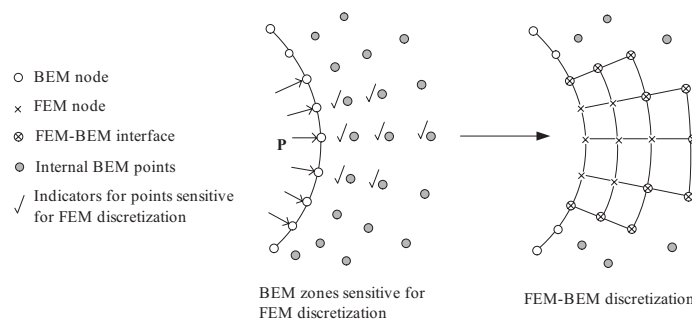


Fig. 1: Generation of FEM and BEM zones

### Numerical Example

In this section we present a numerical example, which serves as a benchmark problem in computational plasticity [14]. The benchmark problem is a stretched plate (width=height=200 mm) with a circular central hole (radius  $r=10$  mm) under plane strain condition. A surface load  $P$  is applied on the plate's upper and lower edges. The applied tractions  $P=100$  N/mm<sup>2</sup> are scaled with the load factor  $\lambda$  which is assumed to be as high as 4.5. Material properties of the plate are described by Young's modulus  $E=206.9$  GPa, Poisson's ratio  $\nu=0.29$ . Material of Von Mises type is considered ( $\sigma_y=450$  MPa), with no hardening effect ( $H=0$ ), as a yield function and plane strain loading conditions. Due to symmetry, only one quarter of the domain is discretized. The problem is solved by means of the adaptive algorithm presented in Section 3. The loads are applied incrementally. Fig. 3 shows the initial (elastic prediction) and final (energetic methods) estimates of the zones sensible for discretization by the FEM ( $\lambda=3.5$ ). Fig. 3 further shows the coupled FEM-BEM computed results (2000

quadrilateral finite elements and 357 boundary elements). The results compare well with those obtained by conventional FEM solutions (10,000 quadrilateral finite elements). The results clearly show the advantages of the adaptive coupled FEM-BEM models in terms of efficiency.

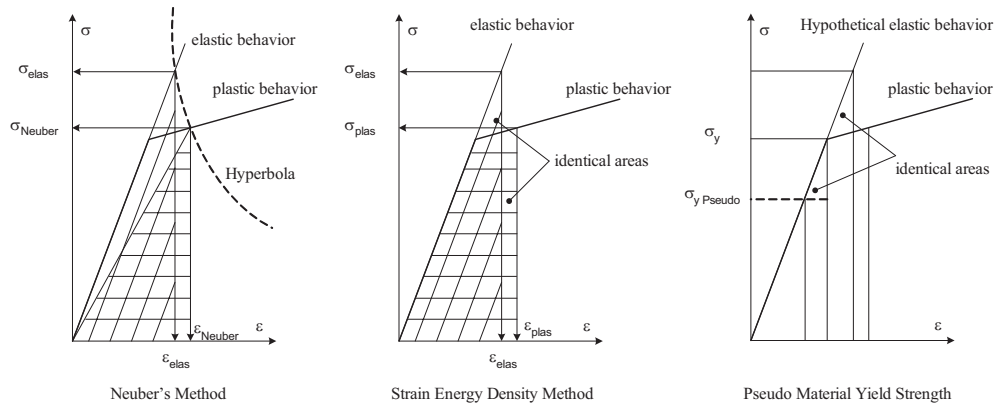


Fig. 3: Neuber's method, strain energy density method and a pseudo value of the yield strength based on hypothetical elastic computations

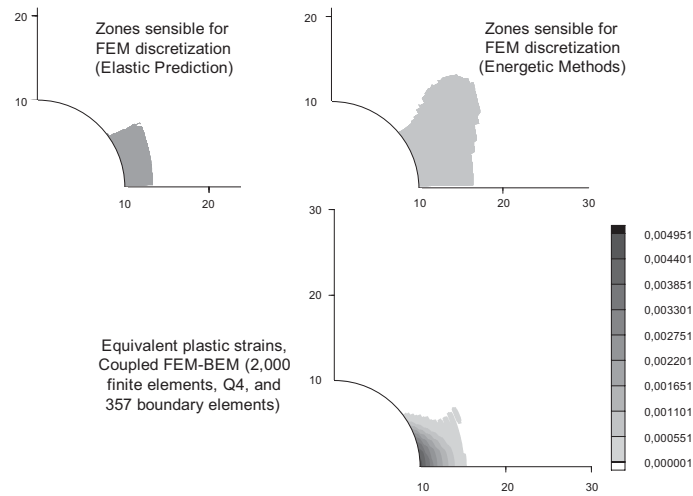


Fig. 4: Intial and final estimation of the FEM discretization zones and computed results via an adaptive FEM-BEM coupling method,  $\lambda = 3.5$

**Conclusions**

This paper deals with FEM-BEM coupling. The paper proposes the use of simple fast post-calculations, based on energetic methods and follows a simple hypothetical elastic boundary element computation, in order to give fast and helpful estimation of the FEM and BEM zones of discretization. The zones of discretization are progressively

adapted according to the state of computation. The present adaptive coupling method eliminates the disadvantages of a prior definition and manual localization of the FEM and BEM sub-domains. It substantially decreases the size of FEM meshes, which plainly leads to reduction of required system resources and gain in efficiency.

#### Acknowledgements

The authors wish to thank Prof. O. Steinbach, Graz University of Technology, for providing the symmetric Galerkin boundary element computer code utilized in some parts of this investigation. The support of the Austrian Science Fund (FWF), Project number: M950, Lise Meitner Program, is gratefully acknowledged.

#### References

- [1] O. C. Zienkiewicz, D. M. Kelly and P. Bettles, "The Coupling of the Finite Element Method and Boundary Solution Procedures," *International Journal for Numerical Methods in Engineering*, **11**, 355-375 (1977).
- [2] M. Costabel, "Symmetric methods for the coupling of finite elements and boundary elements," *Boundary Elements IX*, C. Brebbia, W. Wendland, and G. Kuhn (Eds.), Springer, 411-420 (1987).
- [3] S. Sirtori, G. Maier, G. Novati and S. Miccoli, "A Galerkin Symmetric Boundary Element Method in Elasticity: Formulation and Implementation," *International Journal for Numerical Methods in Engineering*, **35**, 255-282 (1992).
- [4] U. Langer, "Parallel Iterative Solution of Symmetric Coupled FE/BE-Equation via Domain Decomposition," *Contemporary Mathematics*, **157**, 335-344 (1994).
- [5] M. Bonnet, "Regularized Direct and Indirect Symmetric Variational BIE Formulations for Three-Dimensional Elasticity," *Engineering Analysis with Boundary Elements*, **15**, 93-102 (1995).
- [6] S. Ganguly, J. B. Layton and C. Balakrishna, "Symmetric coupling of multi-zone curved Galerkin boundary elements with finite elements in elasticity," *International Journal of Numerical Methods in Engineering*, **48**, 633-654 (2000).
- [7] U. Langer, O. Steinbach, "Coupled Boundary and Finite Element Tearing and Interconnecting Methods," *Proceedings of the Fifteenth International Conference on Domain Decomposition*, Berlin, 83-98 (2003).
- [8] M. Haas, B. Helldörfer and G. Kuhn, "Improved Coupling of Finite Shell Elements and 3D Boundary Elements," *Archive of Applied Mechanics*, **75**, 649-663 (2006).
- [9] R. Springhetti, G. Novati, M. Margonari, "Weak Coupling of the Symmetric Galerkin BEM with FEM for Potential and Elastostatic Problems", *Computer Modeling in Engineering & Sciences*, **13**, 67-80 (2006).
- [10] S. Sirtori, "General Stress Analysis Method by means of Integral Equations and Boundary Elements," *Meccanica*, **14**, 210-218 (1979).
- [11] M. Costabel and E. P. Stephan, "Integral Equations for Transmission Problems in Linear Elasticity," *Journal of Integral Equations*, **2**, 211-223 (1990).
- [12] W. Elleithy, M. Tanaka and A. Guzik, "Interface Relaxation FEM-BEM Coupling Method for Elasto-Plastic Analysis," *Engineering Analysis with Boundary Elements*, **28**, 849-857 (2004)
- [13] R. Desmorat, "Fast Estimation of Localized Plasticity and Damage by Energetic Methods," *International Journal of Solids and Structures*, **39**, 3289-3310 (2002).
- [14] E. Stein, P. Wriggers, A. Rieger and M. Schmidt, "Benchmarks," *Error-Controlled Adaptive Finite Elements in Solid Mechanics*, John Wiley & Sons, 385-404 (2002)

## Quantum Dots in Infinite and Semi-infinite Piezoelectric Semiconductors of General Anisotropy

M. Denda<sup>1</sup>, E. Pan<sup>2</sup> and C.-Y. Wang<sup>3</sup>

<sup>1</sup> Mechanical and Aerospace Engineering Department, Rutgers University  
98 Brett Road, Piscataway, NJ 08854-8058, USA, denda@jove.rutgers.edu

<sup>2</sup> Advanced Material and Structure Center, College of Engineering,  
University of Akron, Akron, OH 44325-3905, USA, pan2@uakron.edu

<sup>3</sup> Mathematics and Modelling Department, Schlumberger-Doll Research,  
Old Quarry RD, Ridgefield, CT 06877-4108, USA, wang20@slb.com

**Keywords:** strained nanoscale quantum dot, anisotropic piezoelectric semiconductor, Green's functions, Eshelby problem, polyhedral inclusion

**Abstract.** Characteristics of the self-organized quantum dots (QDs) such as electron and hole energy levels and wave functions depend on the strain and electric field produced during the growing process of QDs in a semiconductor substrate. The calculation of the strain and electric field must consider material anisotropy induced coupling between the elastic and electric fields and it must include the full three-dimensional and usually intricate shapes of the QDs. In addition, the QDs are formed near the free surface of the semiconductor substrate. In this paper, we present a new Green's function approach which takes into account QDs of arbitrary shape in the infinite and semi-infinite semiconductor substrates with the most general class of anisotropy and piezoelectricity.

### Introduction

In the growth of QDs the self organized QD structures can be produced with high quality in a wide range of semiconductor compounds. The quantum effects due to confinement on electronic motion in the QDs will render novel devices with fascinating functionalities and applications such as semiconductor light-emitting and laser diodes. The growth of semiconductor QDs is achieved by the controlled self-assembled coarsening of a thin film that is strained with respect to the substrate as a result of misfit-lattice-induced strains. The dots are often capped by the substrate material, thus extending the strain around the dot to all angular directions. In the analysis of the electronic structure of QDs, the electron and hole energy levels and wave functions in arbitrary-shaped QD structures are calculated by taking into account effects of the strain and electric fields induced during the QD growth process. Indeed one could control/optimize the electronic and optical properties of QDs by altering the elastic strain and electric field.

The calculation of the strain tensor and electric field involves material anisotropy induced coupling between the elastic and electric fields and it must include the full three-dimensional and usually intricate shapes of the QDs embedded either in the infinite or the semi-infinite substrate. In this paper, we present a new Green's function approach which takes into account QDs of arbitrary shape and semiconductor substrates of infinite and semi-infinite extent with the most general class of anisotropy and piezoelectricity. Following Pan [1], the problem is formulated as an Eshelby inclusion problem of which the solution can be expressed by a volume-integral equation that involves the Green's functions and the equivalent body-force of eigenstrain. The volume integral is subsequently reduced to a line integral exploiting a unique structure of the Green's functions.

### Integral Representation for Equivalent Body Force of Eigenstrain

The elastic field is described by its displacement vector  $u_j$ , body force vector  $f_j$ , stress tensor  $\sigma_{ij}$ , strain tensor  $\gamma_{ij}$  and eigenstrain tensor  $\gamma_{ij}^*$  and the electric field quantities by the electric potential  $\phi$ , charge  $q$ , displacement vector  $D_j$ , field vector  $E_j$ , and eigenfield vector  $E_j^*$ . We adopt the compact notation, using capital-letter subscripts ranging from 1 to 4, for the 'extended' displacement  $u_J$ , body force  $f_J$ , stress

$\sigma_{iJ}$ , strain  $\gamma_{Ji}$  and egenstrain  $\gamma_{Ji}^*$  defined as follows,

$$u_J = \begin{cases} u_j \\ \phi \end{cases}, \quad f_J = \begin{cases} f_j \\ -q \end{cases}, \quad \begin{matrix} J = j = 1, 2, 3 \\ J = 4 \end{matrix}, \quad (1)$$

and

$$\sigma_{iJ} = \begin{cases} \sigma_{ij} \\ D_i \end{cases}, \quad \gamma_{Ji} = \begin{cases} \gamma_{ji} \\ E_i \end{cases}, \quad \gamma_{Ji}^* = \begin{cases} \gamma_{ji}^* \\ E_i^* \end{cases}, \quad \begin{matrix} J = j = 1, 2, 3 \\ J = 4, \end{matrix} \quad (2)$$

Let  $\gamma_{KL}^*$  be the extended eigenstrain of the QD defined over a domain  $V$  bounded by its boundary  $\partial V$ . The extended stress is determined by the constitutive equations

$$\sigma_{iJ} = c_{iJKl}(u_{K,l} - \gamma_{KL}^*). \quad (3)$$

where the relations

$$\gamma_{kl} = (u_{k,l} + u_{l,k})/2, \quad E_l = \phi_{,l}, \quad (4)$$

are used and the material constants  $c_{iJKl}$  are given by

$$c_{iJKl} = \begin{cases} c_{ijkl}, & J = j = 1, 2, 3, & K = k = 1, 2, 3 \\ e_{kli}, & J = 4, & K = k = 1, 2, 3 \\ e_{jil}, & K = 4, & J = j = 1, 2, 3 \\ -\kappa_{il}, & J = K = 4 \end{cases} \quad (5)$$

in which  $c_{ijkl}$ ,  $e_{ijk}$  and  $\kappa_{ik}$  are the elasticity tensor, the piezoelectric tensor and the dielectric permittivity tensor, respectively. Substitution of (3) into the equilibrium equations leads to

$$c_{iJKl}\partial_l\partial_i u_K = c_{iJKl}\gamma_{KL,i}^*. \quad (6)$$

The term in the right hand side

$$f_J(\mathbf{x}) = -c_{iJKl}\gamma_{KL,i}^*(\mathbf{x}) \quad (7)$$

is the equivalent body force of the eigenstrain  $\gamma_{KL}^*$  defined in the QD domain  $V$ , which gives the volume integral representation

$$u_I(\mathbf{x}) = -\int_V g_{IJ}^T(\mathbf{x}, \mathbf{y}) [c_{mJLn}\gamma_{Ln}^*]_{,m} dV(\mathbf{y}), \quad (8)$$

where  $g_{IJ}^T(\mathbf{x}, \mathbf{y})$  is the Green's function, in the semi-infinite body, which is the  $I$ -th component of the extended displacement at location  $\mathbf{x} = (x_1, x_2, x_3)$  produced by the  $J$ -th component of an extended point force applied at  $\mathbf{y} = (y_1, y_2, y_3)$ . It consists of the singular term  $g_{IJ}^\infty(\mathbf{x}, \mathbf{y})$  and the image term  $g_{IJ}(\mathbf{x}, \mathbf{y})$ . For the uniform eigenstrain within the QD domain  $V$ , the volume integral (8) can be transformed into a surface integral on the boundary  $\partial V$  with the result

$$u_I(\mathbf{x}) = c_{mJLn}\gamma_{Ln}^* \int_{\partial V} g_{IJ}^T(\mathbf{x}, \mathbf{y}) \nu_m(\mathbf{y}) ds(\mathbf{y}), \quad (9)$$

where  $\nu_m(\mathbf{y})$  is the outward normal to the boundary  $\partial V$ .

### Green's Functions

The Green's function  $g_{IJ}^\infty(\mathbf{x}, \mathbf{y})$  is the solution of the singular partial differential equation

$$\Gamma_{JP}(\partial_{\mathbf{x}})g_{PM}(\mathbf{x} - \mathbf{y}) = -\delta_{JM}\delta(\mathbf{x} - \mathbf{y}), \quad (10)$$

which is satisfied by [2]

$$g_{IJ}^\infty(\mathbf{x}, \mathbf{y}) = \frac{1}{8\pi^2} \int_{|\mathbf{d}|=1} \frac{A_{IJ}(\mathbf{d})}{D(\mathbf{d})} \delta[\mathbf{d} \cdot (\mathbf{x} - \mathbf{y})] d\Omega(\mathbf{d}), \quad (11)$$

where

$$A_{IJ}(\mathbf{d}) = \text{adj } \Gamma_{IJ}(\mathbf{d}) \quad , \quad D(\mathbf{d}) = \det \Gamma_{IJ}(\mathbf{d}) \quad , \quad (12)$$

and  $\Gamma_{IJ}$  is the differential operator  $\Gamma_{IJ}(\partial_{\mathbf{x}}) = c_{pIJq} \partial_p \partial_q$ , and  $\delta_{JM}$  is the Kronecker delta.

Let  $(\mathbf{q}_1, \mathbf{q}_2, \mathbf{n})$  be a set of unit local orthogonal base vectors (for now, we consider  $\mathbf{n}$  as a constant unit vector, it will be used later as the outward normal to the boundary  $\partial V$ ). We express the unit sphere  $|\mathbf{d}| = 1$  in the integral (11) by

$$\mathbf{d} = \sin \phi \cos \theta \mathbf{q}_1 + \sin \phi \sin \theta \mathbf{q}_2 + \cos \phi \mathbf{n} \quad , \quad (13)$$

from which a new local vector is defined by

$$\mathbf{s} = \cos \theta \mathbf{q}_1 + \sin \theta \mathbf{q}_2 + \eta \mathbf{n} \quad , \quad (14)$$

where  $\eta = \cot \phi$ . The representation (11) can be reduced to a line integral form [2]

$$g_{IJ}^\infty(\mathbf{x}, \mathbf{y}) = -\Re \int_0^\pi \sum_{N=1}^4 \bar{g}_{IJ}^N(\theta) \frac{\text{sign}[\mathbf{n} \cdot (\mathbf{x} - \mathbf{y})]}{\mathbf{s}^N \cdot (\mathbf{x} - \mathbf{y})} d\theta \quad , \quad (15)$$

where

$$\bar{g}_{IJ}^N(\theta) = \frac{1}{2\pi^2} \frac{A_{IJ}(\mathbf{s}^N)}{D_{,\eta}(\mathbf{s}^N)} \quad . \quad (16)$$

The symbol  $\Re$  indicates the real part of the complex number and  $\mathbf{s}^N$  is the value of  $\mathbf{s}$  for the eigenvalue  $\eta^N$  [2] determined by  $D(\mathbf{s}) = 0$ . The integrand of this line integral is given by the product of two terms,  $\bar{g}_{IJ}^N(\theta)$  and  $\text{sign}[\mathbf{n} \cdot (\mathbf{x} - \mathbf{y})]/\mathbf{s}^N \cdot (\mathbf{x} - \mathbf{y})$ . The first term is a function of the material properties only, i.e., independent on the location vectors  $\mathbf{x}$  and  $\mathbf{y}$ . The second term is a simple algebraic function. It is in fact a 'plane wave function' which is in essence a one-dimensional function. Similarly, the derivative of the Green's function is given by

$$g_{IJ,q}^\infty(\mathbf{x}, \mathbf{y}) = \Re \int_0^\pi \sum_{N=1}^4 s_q^N \bar{g}_{IJ}^N(\theta) \frac{\text{sign}[\mathbf{n} \cdot (\mathbf{x} - \mathbf{y})]}{[\mathbf{s}^N \cdot (\mathbf{x} - \mathbf{y})]^2} d\theta \quad . \quad (17)$$

For the semi-infinite body with  $x_3 > 0, y_3 > 0$ , the general boundary condition on the surface  $x_3 = 0$  can be one of the 16 different sets including the traction ( $= 0$ ), displacement ( $= 0$ ), and mixed types [3]. The image term of the Green's function, needed to satisfy the general boundary condition, was obtained by Pan [3] using the Stroh formalism in the double Fourier transformed domain to get the line integral

$$g_{IJ}(\mathbf{x}, \mathbf{y}) = -\frac{1}{2\pi^2} \Re \int_0^\pi \frac{\sum_M^4 \sum_N^4 (\bar{\mathbf{A}})_{IM} (\bar{\mathbf{K}}^{-1} \mathbf{K})_{MN} (\mathbf{A}^T)_{NJ}}{\mathbf{t}^N \cdot (\mathbf{x} - \mathbf{y}) + (\bar{p}^M - p^N)x_3} d\theta \quad , \quad (18)$$

where  $p^N$  ( $N = 1, 2, 3, 4$ ) and  $\mathbf{A}$  are the eigenvalues and eigenmatrix for the Stroh formalism and  $\mathbf{t}^N = (\cos \theta, \sin \theta, p^N)$  is a global vector. Matrix  $\mathbf{K}$ , function of  $\theta$ , depends on the general boundary condition on the surface  $x_3 = 0$  and can take up to 16 different values. Notice that the integrand is a product of two terms  $(\bar{\mathbf{A}} \bar{\mathbf{K}}^{-1} \mathbf{K} \mathbf{A}^T)_{IJ}$  and  $1/[\mathbf{t}^N \cdot (\mathbf{x} - \mathbf{y}) + (\bar{p}^M - p^N)x_3]$ . The former is the function of  $\theta$  and does not depend on the location vectors  $\mathbf{x}$  and  $\mathbf{y}$ . The derivative of the Green's function is given by

$$g_{IJ,q}(\mathbf{x}, \mathbf{y}) = \frac{1}{2\pi^2} \Re \int_0^\pi \frac{\sum_M^4 \sum_N^4 (\bar{\mathbf{A}})_{IM} \bar{t}_q^M (\bar{\mathbf{K}}^{-1} \mathbf{K})_{MN} (\mathbf{A}^T)_{NJ}}{[\mathbf{t}^N \cdot (\mathbf{x} - \mathbf{y}) + (\bar{p}^M - p^N)x_3]^2} d\theta \quad . \quad (19)$$

We exploit the simple structure of the integrands in (15), (17), (18) and (19) in our evaluation of these integrals.

### Evaluation of Integrals

We evaluate the boundary integral (9) using the line integral expressions for the Green's functions (15), (18) and (17) and (19). We consider the QD with arbitrary shape that can be represented by a collection

of triangular surfaces. Substituting solutions (15), (18) and (17), (19) into (9) and (4) and exchanging integration orders we obtain

$$u_I^T(\mathbf{x}) = u_I^\infty(\mathbf{x}) + u_I(\mathbf{x}), \quad \gamma_{pq}^T(\mathbf{x}) = \gamma_{pq}^\infty(\mathbf{x}) + \gamma_{pq}(\mathbf{x}), \quad E_p^T(\mathbf{x}) = E_p^\infty(\mathbf{x}) + E_p(\mathbf{x}), \quad (20)$$

with

$$u_I^\infty(\mathbf{x}) = c_m J L n \gamma_{Ln}^* \nu_m \int_0^\pi \Re \sum_{N=1}^4 \bar{g}_{IJ}^N(\theta) \phi_N(\mathbf{x}, \theta) d\theta, \quad (21)$$

$$u_I(\mathbf{x}) = c_m J L n \gamma_{Ln}^* \nu_m \int_0^\pi \Re \sum_M^4 \sum_N^4 [(\bar{\mathbf{A}})_{IM} (\bar{\mathbf{K}}^{-1} \mathbf{K})_{MN} (\mathbf{A}^T)_{NJ}] \Phi_{MN}(\mathbf{x}, \theta) d\theta, \quad (22)$$

$$\gamma_{pq}^\infty(\mathbf{x}) = \frac{1}{2} c_m J L n \gamma_{Ln}^* \nu_m \int_0^\pi \Re \sum_{N=1}^4 [s_q^N \bar{g}_{pJ}^N(\theta) + s_p^N \bar{g}_{qJ}^N(\theta)] \psi_N(\mathbf{x}, \theta) d\theta, \quad (23)$$

$$\begin{aligned} \gamma_{pq}(\mathbf{x}) &= \frac{1}{2} c_m J L n \gamma_{Ln}^* \nu_m \int_0^\pi \Re \sum_M^4 \sum_N^4 \\ &[(\bar{\mathbf{A}})_{pM} \bar{t}_q^M (\bar{\mathbf{K}}^{-1} \mathbf{K})_{MN} (\mathbf{A}^T)_{NJ} + (\bar{\mathbf{A}})_{qM} \bar{t}_p^M (\bar{\mathbf{K}}^{-1} \mathbf{K})_{MN} (\mathbf{A}^T)_{NJ}] \Psi_{MN}(\mathbf{x}, \theta) d\theta, \end{aligned} \quad (24)$$

and

$$E_p^\infty(\mathbf{x}) = c_m J L n \gamma_{Ln}^* \nu_m \int_0^\pi \Re \sum_{N=1}^4 s_p^N \bar{g}_{4J}^N(\theta) \psi_N(\mathbf{x}, \theta) d\theta, \quad (25)$$

$$E_p(\mathbf{x}) = c_m J L n \gamma_{Ln}^* \nu_m \int_0^\pi \Re \sum_M^4 \sum_N^4 (\bar{\mathbf{A}})_{4M} [\bar{t}_p^M (\bar{\mathbf{K}}^{-1} \mathbf{K})_{MN} (\mathbf{A}^T)_{NJ}] \Psi_{MN}(\mathbf{x}, \theta) d\theta, \quad (26)$$

where

$$\phi_N(\mathbf{x}, \theta) = - \int_A \frac{\text{sign}[\mathbf{n} \cdot (\mathbf{x} - \mathbf{y})] ds(\mathbf{y})}{\mathbf{s}^N \cdot [\mathbf{x} - \mathbf{y}]}, \quad \psi_N(\mathbf{x}, \theta) = \int_A \frac{\text{sign}[\mathbf{n} \cdot (\mathbf{x} - \mathbf{y})] ds(\mathbf{y})}{\{\mathbf{s}^N \cdot [\mathbf{x} - \mathbf{y}]\}^2}, \quad (27)$$

and

$$\begin{aligned} \Phi_{MN}(\mathbf{x}, \theta) &= - \frac{1}{2\pi^2} \int_A \frac{ds(\mathbf{y})}{\mathbf{t}^N \cdot (\mathbf{x} - \mathbf{y}) + (\bar{p}_M - p_N) x_3}, \\ \Psi_{MN}(\mathbf{x}, \theta) &= \frac{1}{2\pi^2} \int_A \frac{ds(\mathbf{y})}{[\mathbf{t}^N \cdot (\mathbf{x} - \mathbf{y}) + (\bar{p}_M - p_N) x_3]^2}, \end{aligned} \quad (28)$$

are integrals over a triangle  $A$  which can be integrated analytically. As a result, only the line integrals over  $(0, \pi)$  in equations (21)-(26) need to be computed numerically.

The integrations in (27) can be performed in the local coordinates for the triangular element  $A$  as shown in Fig.1 with the result

$$\phi_N(\mathbf{x}, \theta) = \frac{\text{sign}(\tilde{x}_3) h}{\cos \theta} \left[ \frac{z_1 \log z_1 - z_2 \log z_2}{z_1 - z_2} - \frac{z_1 \log z_1 - z_3 \log z_3}{z_1 - z_3} \right], \quad (29)$$

$$\psi_N(\mathbf{x}, \theta) = \frac{\text{sign}(\tilde{x}_3) h}{\cos \theta} \left[ \frac{\log z_1 - \log z_2}{z_1 - z_2} - \frac{\log z_1 - \log z_3}{z_1 - z_3} \right], \quad (30)$$

where

$$z_1 = h \sin \theta - \varsigma_N, \quad z_2 = l_2 \cos \theta - \varsigma_N, \quad z_3 = -l_1 \cos \theta - \varsigma_N. \quad (31)$$

and

$$\varsigma_N = (\mathbf{x} - \mathbf{y}_0) \cdot \mathbf{s}^N = \tilde{x}_1 \cos \theta + \tilde{x}_2 \sin \theta + \tilde{x}_3 \eta^N. \quad (32)$$

As shown in Fig.1,  $\mathbf{y}_0 = (y_{01}, y_{02}, y_{03})$  is the origin of the local coordinate system and

$$\tilde{x}_1 = (\mathbf{x} - \mathbf{y}_0) \cdot \mathbf{q}_1, \quad \tilde{x}_2 = (\mathbf{x} - \mathbf{y}_0) \cdot \mathbf{q}_2, \quad \tilde{x}_3 = (\mathbf{x} - \mathbf{y}_0) \cdot \mathbf{n}. \quad (33)$$

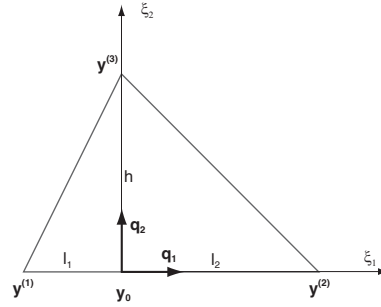


Figure 1: Local coordinate system  $(\xi_1, \xi_2, \xi_3)$  with the origin  $\mathbf{y}_0$  and the unit vectors  $\mathbf{q}_1$  and  $\mathbf{q}_2$  and  $\mathbf{n}$ . The axis  $\xi_3$  and the unit normal  $\mathbf{n}$ , perpendicular to the element, are not shown.

Similarly, the integrations in (28) is given by

$$\Phi_{MN}(\mathbf{x}, \theta) = \frac{h}{\tau_1^N} \left[ \frac{Z_1 \log Z_1 - Z_2 \log Z_2}{Z_1 - Z_2} - \frac{Z_1 \log Z_1 - Z_3 \log Z_3}{Z_1 - Z_3} \right], \quad (34)$$

$$\Psi_{MN}(\mathbf{x}, \theta) = -\frac{h}{\tau_1^N} \left[ \frac{\log Z_1 - \log Z_2}{Z_1 - Z_2} - \frac{\log Z_1 - \log Z_3}{Z_1 - Z_3} \right], \quad (35)$$

where  $(\tau_1^N, \tau_2^N)$  are the local  $\xi_1$  and  $\xi_2$  components, of the global vector  $\mathbf{t}^N$ . In addition,

$$Z_1 = h\tau_2^N - \varepsilon_N, \quad Z_2 = l_2\tau_1^N - \varepsilon_N, \quad Z_3 = -l_1\tau_1^N - \varepsilon_N, \quad (36)$$

and

$$\varepsilon_N = (\mathbf{x} - \mathbf{y}_0) \cdot \mathbf{t}^N + (\bar{p}^M - p^N)x_3. \quad (37)$$

Now, with the analytical solutions given by (29), (34) and (30), (35) the only concerns remained are the computation of the line integrals (15), (17)-(19), which can be achieved by numerical integration. The integrands in the line integrals (21)-(26) are given by the products of (a) functions of the material properties only, which are location independent, and (b) functions of location and geometry.

**Summary**

In this paper, we have presented a new Green’s function approach for the calculation of the strain and electric field in and out of QDs embedded in the semiconductor substrate of infinite and semi-infinite extents. QDs of arbitrary shape and semiconductor substrates with the most general class of anisotropy and piezoelectricity are considered. The problem is formulated as an Eshelby inclusion problem of which the solution can be expressed by a volume-integral equation, which is subsequently reduced to a line integral. The unique structure of the integrand of the line integral facilitates the coding procedure and the computation for very large systems. Numerical results for the QDs in the infinite substrate are given in [2] and those for the semi-infinite substrate will be shown during the conference.

**References**

[1] E. Pan *J. Appl. Phys.*, **91**, 3785–3796 (2002).  
 [2] C.-Y. Wang, E. Pan and M. Denda *Int. J. Solids Struct.*, **43**, 7593–7608 (2006).  
 [3] E. Pan *Proc. R. Soc. Lond. A*, **458**, 181–208 (2002).



# A time-domain decomposition method for the parallel boundary element solution of diffusion problems

D. Crann<sup>1</sup>, S. J. Kane<sup>1</sup>, A. J. Davies<sup>1</sup> and C-H. Lai<sup>2</sup>

<sup>1</sup>*School of Physics, Astronomy and Mathematics,  
University of Hertfordshire, Hatfield, Herts. AL10 9AB, U.K.*

<sup>2</sup>*School of Computing and Mathematical Sciences,  
University of Greenwich, London SE10 9LS, U.K.*

## Abstract

In an earlier paper the authors considered a hybrid Laplace transform/finite difference method for dealing with the time variable in the solution of diffusion problems. An important property of the Stehfest method for the numerical inversion of the Laplace transform is that it develops the solution at any specific time without the necessity of solutions at earlier times. The hybrid procedure involves a time-domain decomposition into a set of time slabs in each of which the initial condition is obtained using the Laplace transform, the solution within the time slab is then determined by a finite difference approach. The method has been shown to be very successful in a sequential sense. In this paper we discuss the implementation in a parallel environment. The time-domain decomposition is ideally-suited to a parallel implementation with each time slab associated with its own processor and the solution in each time slab is obtained independently of the others. Since the only inter-processor communication occurs during broadcast and gather of data the parallel implementation exhibits very nearly linear speed-up

*Keywords: Boundary element method, domain decomposition, diffusion problem*

## 1 INTRODUCTION

We follow the approach to the numerical solution of the diffusion problem recently developed by the authors [1]. The ‘space variation’ is developed using a boundary element approach and the ‘time development’ is obtained in a hybrid Laplace transform/finite difference manner. In their paper Davies et al. [1] solve the problem in a sequential manner. However the major

attraction of the hybrid approach is that it has the potential for exploitation in a parallel environment. Such procedures have been considered before in a purely finite difference context [2, 3] in terms of the so-called *parareal algorithm*. The difference in the authors' approach is the use of the Laplace transform.

A numerical Laplace transform approach using Stehfest's [4, 5] numerical inversion method is used because the solution at any specific time can be obtained independently of those at any other times. The space solution at each time value could be obtained by any suitable solver and the most commonly used approach is that using finite differences [2, 3]. In our approach we shall use a boundary element technique in space incorporating the dual reciprocity method. This has been used extensively by the authors in both Laplace transform and finite difference time-decompositions [1, 6, 7, 8, 9].

We consider the following reaction-diffusion model problem:

$$\nabla^2 u = \frac{1}{\alpha} \frac{\partial u}{\partial t} + h(u, x, y, t) \quad \text{in } \Omega \quad (1)$$

subject to the boundary conditions

$$\begin{aligned} u(s, t) &= u_1(s, t) \quad \text{on } \Gamma_1 \\ q(s, t) &= \frac{\partial u}{\partial n}(s, t) = q_2(s, t) \quad \text{on } \Gamma_2 \end{aligned} \quad (2)$$

$$\text{with} \quad u(x, y, 0) = u_0(x, y) \quad \text{in } \Omega \quad (3)$$

where  $\Omega$  is a closed two-dimensional region bounded by the curve  $\Gamma = \Gamma_1 + \Gamma_2$ . We seek the solution  $u(x, y, t)$  for  $(x, y) \in \Omega$  and  $0 < t \leq T$ .

## 2 THE HYBRID ALGORITHM

### 2.1 The Laplace transform

We define the Laplace transform,  $\bar{u}(x, y; \lambda)$ , of  $u(x, y, t)$ , as

$$\bar{u}(x, y; \lambda) = \int_0^\infty u(x, y, t) e^{-\lambda t} dt$$

Taking the Laplace transform of the initial boundary-value problem (1), (2), (3) we obtain

$$\nabla^2 \bar{u} = \frac{1}{\alpha} (\lambda \bar{u} - u_0) + \bar{h} \quad \text{in } \Omega \quad (4)$$

$$\begin{aligned} \bar{u}(s; \lambda) &= \bar{u}_1(s; \lambda) \quad \text{on } \Gamma_1 \\ \bar{q}(s; \lambda) &= \bar{q}_2(s; \lambda) \quad \text{on } \Gamma_2 \end{aligned} \quad (5)$$

The elliptic boundary-value problem, in Laplace transform space, given by equations (4) and (5) is solved using the dual reciprocity method [6, 10] as follows:

We write equation (4) in the form

$$\nabla^2 \bar{u} = b(x, y, \bar{u}; \lambda) \quad \text{in } \Omega \quad (6)$$

subject to the same boundary equations (5).

In this form we can apply the dual reciprocity approach using the fundamental solution,  $u^*$ , of the Laplacian operator to write equation (6) in the integral form

$$c_i \bar{u}_i + \int_{\Gamma} q^* \bar{u}_i d\Gamma - \int_{\Gamma} u^* \bar{q}_i d\Gamma + \int_{\Omega} b_i u^* d\Omega = 0 \quad (7)$$

Using the usual DRM approach we approximate the source term,  $b$ , in equation (6) in terms of a linear combination of radial basis functions,  $f_j(R)$ , and apply collocation at  $M = N + L$  nodes where  $N$  and  $L$  are the numbers of boundary and internal nodes respectively.

Hence using Green's theorem in equation (7) we obtain the boundary integral equation

$$c_i \bar{u}_i + \int_{\Gamma} q^* \bar{u}_i d\Gamma - \int_{\Gamma} u^* \bar{q}_i d\Gamma = \sum_{j=1}^N \alpha_j \left( c_i \hat{u}_{ij} + \int_{\Gamma} q^* \hat{u}_j d\Gamma - \int_{\Gamma} u^* \hat{q}_j d\Gamma \right) \quad (8)$$

Internal values are given similarly and equation (8) can be combined with the equivalent internal equation. Collocation at the  $M$  nodes gives the overall set of equations

$$\mathbf{H}\bar{\mathbf{U}} - \mathbf{G}\bar{\mathbf{Q}} = [\mathbf{H}\hat{\mathbf{U}} - \mathbf{G}\hat{\mathbf{Q}}] \mathbf{F}^{-1} \mathbf{b}(\bar{\mathbf{U}}) \quad (9)$$

where  $\mathbf{F}$  is the usual DRM collocation matrix written in the form  $\mathbf{b} = \mathbf{F}\boldsymbol{\alpha}$ . Here matrices  $\mathbf{H}$  and  $\mathbf{G}$  are the usual boundary element matrices and  $\hat{\mathbf{U}}$  and  $\hat{\mathbf{Q}}$  are the matrices of collocated values of the functions  $\hat{\mathbf{u}}$  and  $\hat{\mathbf{q}}$  [11].

Equation (9) can be written in the form

$$\mathbf{H}\bar{\mathbf{U}} - \mathbf{G}\bar{\mathbf{Q}} = \mathbf{S}\mathbf{b}(\bar{\mathbf{U}}) \quad (10)$$

where  $\mathbf{S}$  is a matrix which depends only on the geometry.

By virtue of the form of equation (4) we see that  $\mathbf{b}$  is a linear function of  $\bar{\mathbf{U}}$  so that equation (10) is a linear system of equations. The solution of equation (10) yields the approximate transforms  $\bar{\mathbf{U}}$  and  $\bar{\mathbf{Q}}$  which may then be inverted to obtain the approximate solutions  $\mathbf{U}$  and  $\mathbf{Q}$ .

To implement the Stehfest method we proceed as follows:

Choose a specific time value,  $\tau$ , at which we seek the solution and define a discrete set of transform parameters given by

$$\left\{ \lambda_j = j \frac{\ln 2}{\tau} : j = 1, 2, \dots, m; m \text{ even} \right\} \quad (11)$$

The dual reciprocity boundary element method is applied to equation (6) for each  $\lambda_j$  to obtain a set of approximate boundary and internal values

$$\bar{U}_{ij}, \bar{U}_{kj}; \quad i = 1, \dots, N; \quad k = N + 1, \dots, M; \quad j = 1, \dots, m$$

The inverse transforms are then given as follows:

$$U_r = \frac{\ln 2}{\tau} \sum_{j=1}^m w_j \bar{U}_{rj} \quad (12)$$

where  $r = 1, \dots, N$  for boundary points and  $r = N + 1, \dots, M$  for internal points and the weights,  $w_j$ , are given by Stehfest [4, 5]

## 2.2 Finite difference method

We define the time slabs as

$$0 = \tau_0 \leq t < \tau_1, \tau_1 \leq t < \tau_2, \dots, \tau_{p-1} \leq t < \tau_p = T$$

and apply the fine-grained approach in each time slab  $\tau_i \leq t < \tau_{i+1}$  ( $i = 0, 1, \dots, p - 1$ ) in which we use an Euler solver.

We use  $n - 1$  time steps with time step

$$\Delta t = (\tau_{i+1} - \tau_i)/n$$

The Euler algorithm to solve equation (1) is given by the explicit scheme

$$\nabla^2 u_i^{(k+1)} = \frac{1}{\alpha \Delta t} u_i^{(k+1)} - \frac{1}{\alpha \Delta t} u_i^{(k)} + h(x, y, t_k) \quad k = 0, 1, \dots, n - 1 \quad (13)$$

with

$$t_{k+1} = t_k + \Delta t, \quad t_0 = \tau_i$$

The solution at times  $t_k$  may be obtained from the system of linear equations, developed in a similar manner to that for equation (10) in section 2.1:

$$\mathbf{H}\mathbf{U}^{(k+1)} - \mathbf{G}\mathbf{Q}^{(k+1)} = \mathbf{Sb}(\mathbf{U}^k) \quad (14)$$

## 3 EXAMPLE

We consider the non-linear problem

$$\nabla^2 u = \frac{\partial u}{\partial t} + u^2 + h(x, y, t)$$

defined in the unit square, using boundary conditions compatible with the analytic solution  $u = x^2 t^2$

In this case we cannot apply the Laplace transform directly due to the non-linear term  $u^2$  and we use a direct iteration approach as described by Crann [6].

We use 36 linear boundary elements with 9 internal nodes for the dual reciprocity method, the Laplace transform solution is developed at times  $0.5p$  ( $p = 1, 2, \dots, 8$ ) and the Euler time step is  $\Delta t = 0.1$  in each time slab.

The problem was solved on the parallel system at the University of Greenwich which comprises three DEC4100 servers and eighteen single alpha processors. The problem was solved using 1, 2, 4, 8 and 16 processors. We define the speed-up,  $S_p$ , as

$$S_p = \frac{T_p}{T_1}$$

where  $T_j$  is the processor time on  $j$  processors. The speed-up is shown in figure 1 and we see that the process exhibits almost linear speed-up, the small deviation from linearity being due to the initial broadcast and the final gather of data.

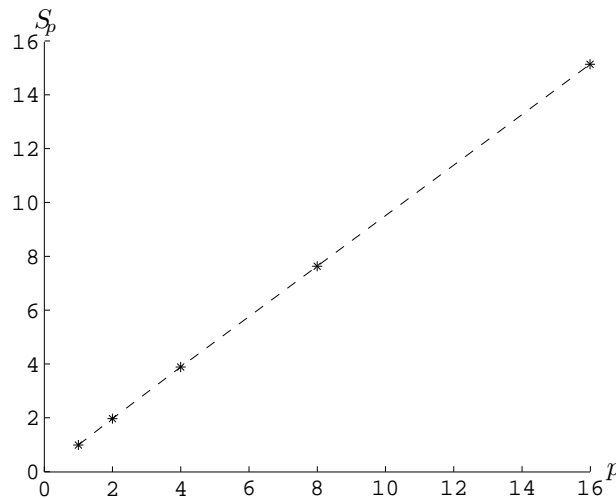


Figure 1: Speed-up,  $S_p$ , as a function of the number of processors,  $p$ .

## 4 CONCLUSIONS

The hybrid Laplace transform/finite difference method provides a suitable approach to the solution of diffusion problems. In this investigation we have considered the approach in a parallel environment. The domain decomposition has an inherent parallelism and there is no inter-processor communication during the computational process. This would guarantee linear speed-up. There is, however, inter-processor communication during the broadcast

and gather of data and this does degrade the linearity by a very small amount. For larger problems this degradation would become vanishingly small.

## References

- [1] Davies AJ, Crann D, Kane SJ and Lai C-H. A hybrid Laplace transform/finite difference boundary element method for diffusion problems. *Comp. Mod. Engng Sci.* accepted for publication, 2007.
- [2] Lions J-L, Maday Y, Turinici G. Résolution d'EDP par un schéma en temps "pararéel". *C.R.Acad. Sci. Paris Ser. I Math* 2001; **332**: 661–668.
- [3] Bal G, Maday Y. A "parareal" time discretisation for non-linear PDE's with application to the pricing of an American put. *Recent developments in domain decomposition methods* 2002; **23**:190–202.
- [4] Stehfest H. Numerical inversion of Laplace transforms, *Comm. ACM.* 1970; **13**:47–49.
- [5] Stehfest H. Remarks on Algorithm 368 [D5] Numerical inversion of Laplace transforms. *Comm. ACM.* 1970; **13**:624.
- [6] Crann D. *The Laplace transform boundary element method for diffusion-type problems.* PhD Thesis, University of Hertfordshire; 2005.
- [7] Crann D, Davies AJ, Lai C-H, Leong SH. Time domain decomposition for European options in financial modelling. *Domain Decomposition Methods 10* 1998; 486–491.
- [8] Davies AJ, Crann D. Parallel Laplace transform methods for boundary element solution of diffusion-type problems. *Advances in Boundary Element Techniques II* 2001; 183–190.
- [9] Davies AJ, Toutip W, Bartholomew-Biggs MC. The dual reciprocity method for coupled thermal/electromagnetic problems. *Boundary element Technology XIV* 2001; 371–380.
- [10] Zhu SP. Time-dependent reaction-diffusion problems and the LT-DRM approach. *Boundary Integral Methods, Numerical and Mathematical Aspects* 1997; 1–35.
- [11] Wrobel LC *The boundary element method.* vol.1. Wiley, 2002.